Department of Chemical Engineering

Modelling of Solid Oxide Fuel Cell - Multi Scaling Modelling of the Planar SOFC

Shahin Hosseini

This Thesis is presented for the Degree of
Doctor of Philosophy
of
Curtin University

November 2011

Declaration

To the best of my knowledge and belief this thesis contains no material previously published by any other person except where due acknowledgment has been made. This thesis contains no material which has been accepted for the award of any other degree or diploma in any university.

Date:

Signature:

Abstract

As a subset of the big project in fuel cell research group at Curtin University, this thesis mainly focused on presenting different perspectives on multi scale modelling of the planar solid oxide fuel cell (SOFC).

First of all, a dynamic plug flow reactor (PFR) model of a planar SOFC was developed. The novelty of this model is based on using the modified expressions for the charge balance between the electrodes-electrolyte interfaces, which enabled us to include double layer capacitance effect of the charge transfer processes for physically characterizing the Faradic and electrolyte current densities. It was shown that under steady state operating condition, no charging or discharging process occurred and in response to a voltage step change double layer capacitance has insignificant effect on transient behaviour of the cell. On the contrary, when SOFC is subjected to a time varying sinusoidal voltage, temperature and reactants' concentration are not sensitive to the high frequent voltage change, while dynamic response of the cell is mainly controlled by the electrochemical reactions and double layer charging or discharging processes.

A new dynamic tank in series reactor (TSR) model of the planar SOFC operating in co-, counter- and cross flow directions was also developed for the first time. One of the novelties of this model (TSR) is the reduction in model complexity, which has been achieved by replacing a planar SOFC with a network of several continuous stirred tank reactors (CSTRs). In addition, this model accelerated 2D simulation to obtain the trend in the distribution of important variables under steady state and dynamic operating conditions. It is worth mentioning that spatial consideration in SOFC dynamic analysis has been given very little attention from the research community. The predicted results from TSR model demonstrate strong coupling between key parameters. Furthermore, examination of the simulation results highlights the influence of different fuel and air flow configurations on the steady state and dynamic performance of the cell.

Finally, a 3D CFD model was developed for the planar methane fuelled SOFC previously designed by Ceramic Fuel Cells Ltd. (CFCL), Melbourne. CFCL has supported this project from its inception. Using this model, the effects of different anode flow field designs on pressure and velocity profiles were investigated. Another important feature of this work is the use of the 3D CFD model to study the combined effects of the geometrical factors and different microstructural parameters of the anode diffusion layer (ADL) on distribution of the key parameters along different spatial domains. From the simulation results, it was shown that an optimal set of the ADL micro structural parameters, which can effectively promote the reforming reaction rate, will not automatically result in the best SOFC performance. In addition, these parameters were found to have conflicting effects on multi component gas transport and the reactions taking place in the SOFC system.

Acknowledgements

This thesis would not have been finished without the support, help, and love from many people who have enriched my life and added so much joy to it. First and foremost, I would like to express my respect and sincere gratitude to my supervisor, Professor Moses O. Tadé from the Department of Chemical Engineering. His knowledge and wisdom were my resources, his hard work my inspiration and his persistence my motivation during these years. I would also like to thanks Dr. Valery A. Danilov, my co-supervisor, Professor Ming Ang, the chairman of my research committee', Dr. Ranjeet Utikar, and Dr. Khaliq Ahmed for their valuable guidance.

This work was supported by several parties to whom I would like to acknowledge my highest gratitude. First, I would like to make particular thanks to the Department of Chemical Engineering, Curtin University who supported the first semester of my study through Departmental Scholarship. I also thank Curtin University who supported me with a full scholarship from 2009-2011 with the Curtin Strategic International Research Scholarships (CSIRS). I am grateful Ceramic Fuel Cells Ltd. Melbourne, Australia for their helpful suggestions, interesting discussions and for providing me with valuable data through the joint research collaboration on modelling of the planar solid oxide fuel cells. I am also thankful the Australian Research Council (ARC) for granting this project. Finally I would also like to acknowledge Jam Petrochemical Complex and National Petrochemical Company, Tehran, Iran for their assistance allows me doing my Ph.D. project in Australia.

It has been a tough time thousands of miles away from home but the groups of friends I found at Curtin University especially in fuel cell research group and centre for process systems computations have made me forget all about it and for that I would like to thank them all. Thanks also due to my officemates with whom I have shared treasured moments.

I would like to thank my wife Maral for her constant love, patience and understanding. She always behind me and helped me to keep my head up through the period of my study.

I am also indebted to my family, especially my parents, my mother in law and my sisters for their love, affection and continuous supports. The final heartfelt words come to my niece Kimia who is such a wonderful blessing and I had just to tell her so.

Brief Biography

Shaihn Hosseini was born in 1976, Tehran-Iran. He received his Master degree by honour in Chemical Engineering from science and research campus of Azad University, Iran 2001. He also holds Batcher degree in Chemical Engineering and graduate diploma in Polymer Process Engineering from Polytechnic University in Iran. He has almost 9 years industrial experience in process design, control and operation. Meanwhile, he was nominated for different awards for his extraordinary contributions in project leadership and achievements from well-recognized companies such as Fuji electric Instruments; Basell Polyolefines, Italian Technimont and Jam Petrochemical Complex that is known as the largest olefine plant in the world. He commenced his Ph.D. studies in July 2008 with scholarship from Chemical Engineering Department, Curtin University and then continued under a Curtin Strategic International Research Scholarship (CSIRS) from 2009-2011. He was also teaching assistant for the units of Advanced Process Control, in addition to Process Control & Instrumentations from February 2009 to November 2011. Furthermore, he is qualified as professional engineer by the Engineers Australia.

Table of Contents

List of Figures

List of Tables

List of Symbols

A_s	Reactive surface area per unit volume, (m^{-1})
C	Molar density, ($mol.m^{-3}$)
C_{dL}	Double layer capacitance, ($A.s.V^{-1}.m^{-2}$)
c_P	Specific heat capacity, ($J.mol^{-1}.K^{-1}$)
d_P	Particle diameter, (m)
D_{ij}	Binary diffusion coefficients, ($m^2.s^{-1}$)
$D_{i,GM}$	Diffusion coefficients of the species in a multi-component gas mixture, ($m^2.s^{-1}$)
$D_{i,k}$	Knudsen diffusion coefficients of the species, ($m^2.s^{-1}$)
D_i^{eff}	Effective diffusion coefficients of the species, ($m^2.s^{-1}$)
$e(i)$	Normalized error
E	Specific energy, ($J.kg^{-1}$)
E_{act}	Activation energy, ($J.mol^{-1}$)
E_{ref}	Reference voltage, (V)
E_{cell}	Cell Voltage, (V)
E_{bias}	Bias voltage, (V)
E_{amp}	Amplitude voltage, (V)
f	Frequency, (Hz)
F	Faraday's constant, (96485 $C.mol^{-1}$)
F^f	Fuel mass flow rate, ($mol.s^{-1}$)
F^a	Air mass flow rate, ($mol.s^{-1}$)
g	Acceleration due to gravity, ($m.s^{-2}$)
ΔG^0	Standard Gibbs free energy change, ($J.mol^{-1}$)
ΔH	Enthalpy change of reaction, ($J.mol^{-1}$)
H	Height of gas channels, (m)
h	Enthalpy, ($J.mol^{-1}$)
$\hbar$	Convective heat transfer coefficient, ($W.m^{-2}.K^{-1}$)
i	Current density, ($A.m^{-2}$)
i_L	Linear current density, ($A.m^{-1}$)

i_0	Exchange current density, ($A.m^{-2}$)
J	Diffusion flux, ($mol.m^{-2}.s^{-1}$)
k	Solid thermal conductivity, ($J.m^{-1}.s^{-1}.K^{-1}$)
L	Channel length, (m)
M	Momentum flux tensor, (Pa)
M_w	Molecular weight, ($g.mol^{-1}$)
n	Mass flux, ($Kg.m^{-2}.s^{-1}$), Number of CSTR compartment in TSR model
n_e	Number of electrons participating in electrochemical reaction
n_t	Total number of particles per reaction volume, (m^{-3})
n_{elde}	Number fraction of electrode particles in the anode functional layers, (%)
n_{elyt}	Number fraction of electrolyte particles in the anode functional layers, (%)
P	Pressure, (Pa)
P_i	Partial pressure, (Pa)
P_{elde}	Probability of the electrode particles
P_{elyt}	Probability of the electrolyte particles
q	Heat flux, ($J.m^{-2}.s^{-1}$)
Q	Surface charge density, ($C.m^{-2}$)
r	Resistance, (Ω)
r_{elde}	Radius of electrode particles
r_{elyt}	Radius of electrolyte particles
r_P	Pore radius
R	Ideal gas constant, ($J.mol^{-1}.K^{-1}$)
R_h	Heat flux, ($J.m^{-2}.s^{-1}$)
R_r	Mass flux, ($mol.m^{-2}.s^{-1}$)
S	Electrode surface area, (m^2)
S_h	Volumetric heat source term, ($J.m^{-3}.s^{-1}$)
S^r	Volumetric mass source term, ($mol.\ m^{-3}.s^{-1}$)
S_M	Momentum source term, ($N.m^{-3}$)
T	Temperature, (K)
t	Time, (s)

$\vec{u}$	Tensor of velocity, ($m.s^{-1}$)
υ	Velocity in the x direction, ($m.s^{-1}$)
V	Volume, (m^3)
v	Velocity in the y direction, ($m.s^{-1}$)
x	Rectangular coordinate in x direction, (m)
y	Rectangular coordinate in y direction, (m)
y_i	Species mole fraction, (%)
w	Velocity in the z direction, ($m.s^{-1}$)
z	Rectangular coordinate in z direction, (m)
Z	Average coordinate number
Z_{elde}	Coordinate number of the electrode particles
Z_{elyt}	Coordinate number of the electrolyte particles

Greek Letters

α_A^A	Anodic charge transfer coefficient for anode
α_C^A	Cathodic charge transfer coefficient for anode
α_A^C	Anodic charge transfer coefficient for cathode
α_C^C	Cathodic charge transfer coefficient for cathode
α_P	Permeability, (m^2)
β	Species reaction order
γ	Pre-exponential kinetic factor of electrochemical reactions, ($A.m^{-2}$)
δ	Thickness, (μm)
ε	Porosity, (%)
η	Electric potential steps at the electrodes, (V)
η_{eq}	Equilibrium electric potential steps of the electrodes, (V)
η_{act}	Activation overpotential of the electrodes, (V)
θ	Contact angle, (^{o})
ι	Tortuosity
κ	Reaction rate constant
λ_s	Effective factor of the reactive volume

μ	Dynamic viscosity, (Pa.s)
μ_i^0	Standard state chemical potential of different species i, ($J.mol^{-1}$)
ν_i	Species stoichiometric coefficient
ξ	Emissivity
ρ	Density, ($kg.m^{-3}$)
σ_{EB}	Stefan-Boltzmann constant, ($W.m^{-2}.K^{-4}$)
σ	Conductivity, ($\Omega^{-1}.m^{-1}$)
τ	Viscous stress, (Pa)
Φ_{elde}	Electrode potential, (V)
Φ_{elyt}	Electrolyte potential beyond the electrode, (V)
Ψ_{elde}	Volume fraction of the electrode particles, (%)
Ψ_{elyt}	Volume fraction of the electrolyte particles, (%)
ω	Angular frequency, (rad)

Subscripts

avg	Average
cell	Cell
eq	Equilibrium
elde	Electrode
elyt	Electrolyte
exp	Experimental
F	Faradic
f	Forward reaction
gas	Gas
i	Species i
in	Inlet
i, j	i, j Cell
j	Species j
out	Outlet

n	Normal
Sim	Simulation

Superscripts

A	Anode electrode
a	Airgas channel
C	Cathode electrode
chem	Chemical reaction
cat	Catalyst layer
eff	Effective
elec	Electrochemical reaction
f	Fuel gas channel
I	Interconnect
PEN	PEN structure
rad	Radiation
S	Solid phase
SMR	Steam Methane Reforming
WGS	Water Gas Shift

Acronyms

ACL	Anode Catalyst Layer
ADL	Anode Diffusion Layer
AU	Air Utilization
BC	Boundary condition
CCL	Cathode Catalyst Layer
CDL	Cathode Diffusion Layer
CHP	Combined Heat and Power System
CSTR	Continuous Stirred Tank Reactor
FU	Fuel Utilization
LSE	List Square Error
PEN	Positive electrode – Electrolyte – Negative electrode

PFR Plug Flow Reactor

SFOC Solid Oxide Fuel Cell

TSR Tank in Series Reactors

TPB Triple Phase Boundary

Chapter 1

Introduction

1.1. Background and Motivation

Starting with the industrial revolution in the late eighteenth century, human life style has been changed dramatically and the use of machines has infiltrated into almost all aspects of our daily life. For several decades, in the absence of technological advances, conventional power devices have been used to convert energy from conventional fuels. However, conversion of energy by the conventional methods is highly polluting to our environment and affects the greenhouse gas emissions. Additionally, the efficiency of the conventional methods is limited by the Carnot efficiency [1, 2], which in turn accelerates the continual increase of the worldwide energy demands by the industrial sector, which consumes about one-half of the world's total delivered energy followed by transportation sector that is second only to the industrial one[3]. All these, combined with concerns about the limitation of the conventional fuels had led to the new alternatives particularly, the renewable resources[3, 4].

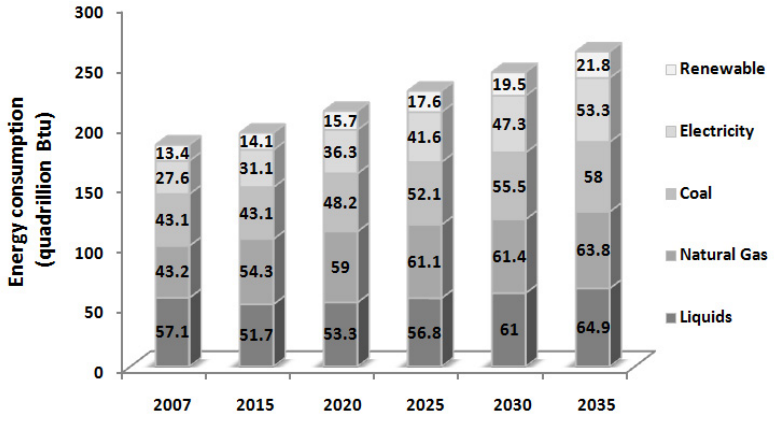

Figure 1.1 - World industrial delivered energy consumption by energy source[5]

Figure 1.1 presents projection for the worldwide energy demands through 2035 in which, the electricity followed by the renewable resource has the most rapid growth from 27.6 and 13.4 quadrillion Btu in 2007 to 53.3 and 21.8 quadrillion Btu in 2035 respectively. However, as Figure 1.1 shows, renewable resource is expected to have the small share in the world industrial energy demands.

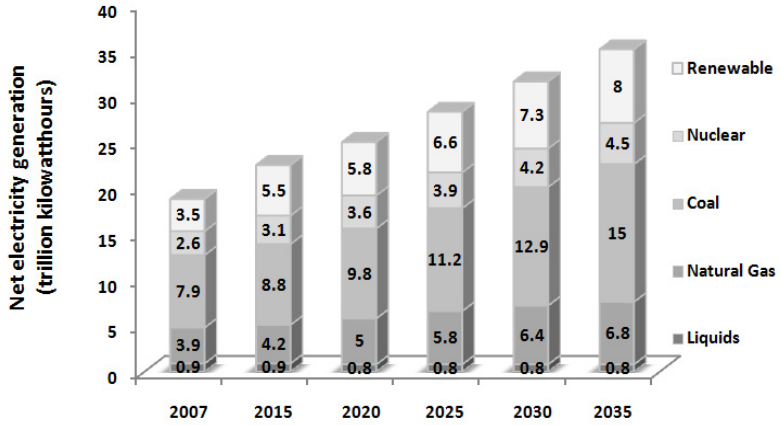

Figure 1.2 - World net electricity generation by energy source [5]

Additionally, from Figure 1.2 it is evident that long term prospects continue to improve the world net electricity generation from both renewable and nuclear fuels; however, combined with the statistical data from Figure 1.1, coal, natural gas and liquid fuels are expected to remain as the most important energy resources over the same projected period. All these bring us to the point that although using of the renewable energy resource is a good alternative to meet the future energy demands, development of the more efficient and less polluting energy conversion devices capable to use both conventional fuels and renewable energy sources can be helpful in the meantime. In this regard, fuel cell has been considered as a promising energy conversion device predominantly for electricity generation [2, 6]. Fuel cell's operational principle bypasses the limitations of the Carnot cycle, which results in higher theoretical efficiency than internal combustion engines [1]; therefore, fuel cells are consuming fewer amounts of fuel and they are less polluting to our environment. However, among different types of fuel cells, the planar-type solid oxide fuel cell (SOFC) is potentially attractive due to its fuel flexibility and compactness.[7, 8] On the other hand, the high operating temperature and capabilities

of the fuel flexibility can make SOFCs suffer from low reliability[9]. Therefore, numerous technical challenges exist to achieve the goal of a highly efficient and environmentally friendly system with comparable reliability, cost and lifetime of the conventional power devices [6]. Current research is mainly aimed at solving hurdles to the components' material, flow field design, thermal and structural stability of the cell and stack and fuel cell control system design. To address these research challenges in the path toward the fuel cell commercialization, numerical modelling is critical because of a number of reasons[6, 9]. First, fuel cell modelling is a valuable tool to gain better insight into the physics and chemistry of the inner processes occurring within the cell. Second, modelling is a valid tool to modify the process parameters in a given direction more cost effectively and more quickly than experimental procedure. Lastly, a physically based model is capable of predicting the fuel cell performance in line with the real physics and under the steady state and dynamic operating conditions. In view of this, modelling can play a role as a diagnostic tool for assessing the state of the fuel cell stack and/or system.

In the past decades, there has been enormous progress in fuel cell modelling. However, with respect to the complexity of the processes happening in a fuel cell, hardware limitation, memory requirements and computational time we still need to improve the modelling strategies. Therefore, the motivation behind this study is to improve physically based multi scale modelling of the planar solid oxide fuel cells to address the following objectives.

1.2. Objective

From the literature review that will be explained in the next chapter, it is evident that in most of the SOFC dynamic models, the effect of the charge double layer capacitance on transient characteristics of the SOFCs has been neglected and with a few exceptions it is lumped together with the electrochemical reaction potential steps. Therefore, there is a limitation to physically characterize of the current densities at the electron and ion conducting media upon transient conditions. Additionally, with respect to the effects of different fuel and air flow configurations on the steady state and dynamic performances, there is a need for a new SOFC dynamic model with less complexity and computational dexterity that falls between

the most simplified lumped and multi-dimensional models found in the literature. Finally, there is a need for a complete 3D CFD model to investigate the combined effects of the flow field design and micro-structural factors on distribution of the key parameter and overall performance of an industrial methane fuelled SOFC. Hence, from the motivation behind this study and the controversial research areas in SOFC modelling that comes from the literature review of the next chapter, the objectives of this thesis are:

- To develop dynamic plug flow reactor (PFR) model of a planar SOFC with distributed charge balance equation between the electron and ion conducting phases.
- To develop new dynamic tanks in series (TSR) model of a planar SOFC as a network of several CSTR compartments.
- To develop 3D CFD model of an industrial planar SOFC stack previously designed by the Ceramic Fuel Cells Ltd.

1.3. Contributions

Building on the existing SOFC models, which have been developed by the other researchers, the main contributions of this thesis are summarized as follows:

Dynamic plug flow reactor model accounting for the mass, heat and charge balances has been developed to analyse the steady state and dynamic performances of a planar SOFC. In this model modified expression for the charge balance between the electron and ion conducting phases facilitates physically based characterisation of the electronic and ionic current densities upon transient condition and under the effects of double layer capacitances at the electrode-electrolyte interfaces.

A new tank in series model of a planar SOFC has been developed for the first time. This model takes into account the charge balances at the electrodes and electrolyte interfaces, species mass balances to the gas channels and diffusion layers, and energy balances for the fuel and air channels and also for the PEN structures. This

model provides 2D visualization map of the SOFC performance with co-, counter- and cross-flow directions of fuel and air under the steady state and dynamic operating conditions. The model solves most of the important details that are resolved by a 2D CFD model but it is much less intensive in computational time. Additionally, the reduction in model complexity has been achieved by replacing a planar SOFC with a network of several continues stirred tank reactors. Using this model, it is also possible to take into account the hydrodynamic effects of different flow field designs.

Further contribution of this research was accomplished in collaboration with Ceramic Fuel Cell Ltd. (CFCL). The originality of this work lies in the fact that a three dimensional CFD model was developed to examine the combined effects of the anode flow field design and micro-structural parameters of the anode diffusion layer on distribution of the key parameters along different spatial domains and the overall performance of the industrial planar SOFC stack, previously designed by CFCL. Another specific impact of this work is the presentation of a 3D CFD model for a complete SOFC, which is evaluated by the experimental data that has been reported from a cell, the same as the modelled one.

1.4. Organization of the Thesis

As Figure 1.3 shows, this thesis is organized into 6 chapters including the present introduction. Chapter 2 is on comprehensive literature survey, which provides a brief introduction to the fuel cell technology followed by an assessment of the SOFC models published in the open literature. To address the ideas that come from the literature review, Chapter 3 presents development of the 1D dynamic plug flow reactor (PFR) model of a planar SOFC with modified charge balance equation, which is capable of dynamically characterizing the electronic and ionic current densities in line with the real physics of the charge transfer process. Chapter 4 details the development of a network of several continuous stirred tank reactors (CSTR) as the new dynamic tank in series (TSR) model of a planar SOFC. The main idea involved is accelerating 2D performance analysis of a planar solid oxide fuel cell with different fuel and air flow directions under the steady state and dynamic operating conditions. Chapter 5 presents our collaboration with the

Ceramic Fuel Cell Ltd. (CFCL) for developing of a 3D CFD model of an industrial planar methane fuelled SOFC. This model is validated by a set of experimental data, which are produced from a cell similar to the modelled one. Furthermore, the influence of different anode flow field designs on pressure and velocity profiles are analysed therein. Also the effects of the anode micro-structural parameters on spatial distribution of temperature, reaction rates and species concentration profiles are presented in Chapter 5. Lastly, some key conclusions and the scope for future research work are outlined in Chapter 6.

1.5. Publications in Support of This Thesis

Several following publications were extracted from this work, which are totally or partly included in this thesis.

Publications which are included totally:

Hosseini, S.; Danilov, V. A.; Tade, M. O.; Datta, R.1D physically based dynamic model for the planar SOFC. (It has been submitted to the *Electrochim.Acta* - Under review).

Hosseini, S.; Tade, M. O.; Ahmed, K. The combined effects of macro and micro-structural parameters on predicted results from 3D model of a planar SOFC; Technical Report for Ceramic Fuel Cells Ltd.: Melbourne, VIC, October 2011.

Hosseini, S.; Tade, M. O.; Ahmed, K. On the effects of geometry and methane reforming kinetics in predicted results from the mechanistic model of a planar SOFC. Presented in Chemeca International Conference 2011, Sydney, Australia.

Hosseini, S.; Danilov, V. A.; Vijay, P.; Tade, M. O. 2D performance analysis with a new tank in series model of the planar SOFC operating with different flow directions. Presented in Chemeca International Conference 2011, Sydney, Australia.

Hosseini, S.; Danilov, V. A.; Vijay, P.; Tade, M. O. Improved tank in series model for the planar solid oxide fuel cell. *Ind. Eng. Chem. Res.***2011**, 50, 1056 – 1069.

Hosseini, S.; Tade, M. O.; Ahmed, K. On the effects of the methane steam reforming in a planar anode supported solid oxide fuel cell; Technical Report for Ceramic Fuel Cells Ltd.: Melbourne, VIC, July 2010.

Hosseini, S.; Tade, M. O.; Ahmed, K. Effects of geometry on pressure and velocity profiles: Comparison among three different flow field designs; Technical Report for Ceramic Fuel Cells Ltd.: Melbourne, VIC, February 2010.

Publications which are included partly:

Hosseini, S.; Danilov, V. A.; Tade, M. O.A dynamic CSTR model for SOFC. Chemeca International Conference 2009; 407-415.

Hosseini, S.; Danilov, V. A.; Tade, M. O.A dynamic plug flow model for planar SOFC. Chemeca International Conference 2009; 2636-2646.

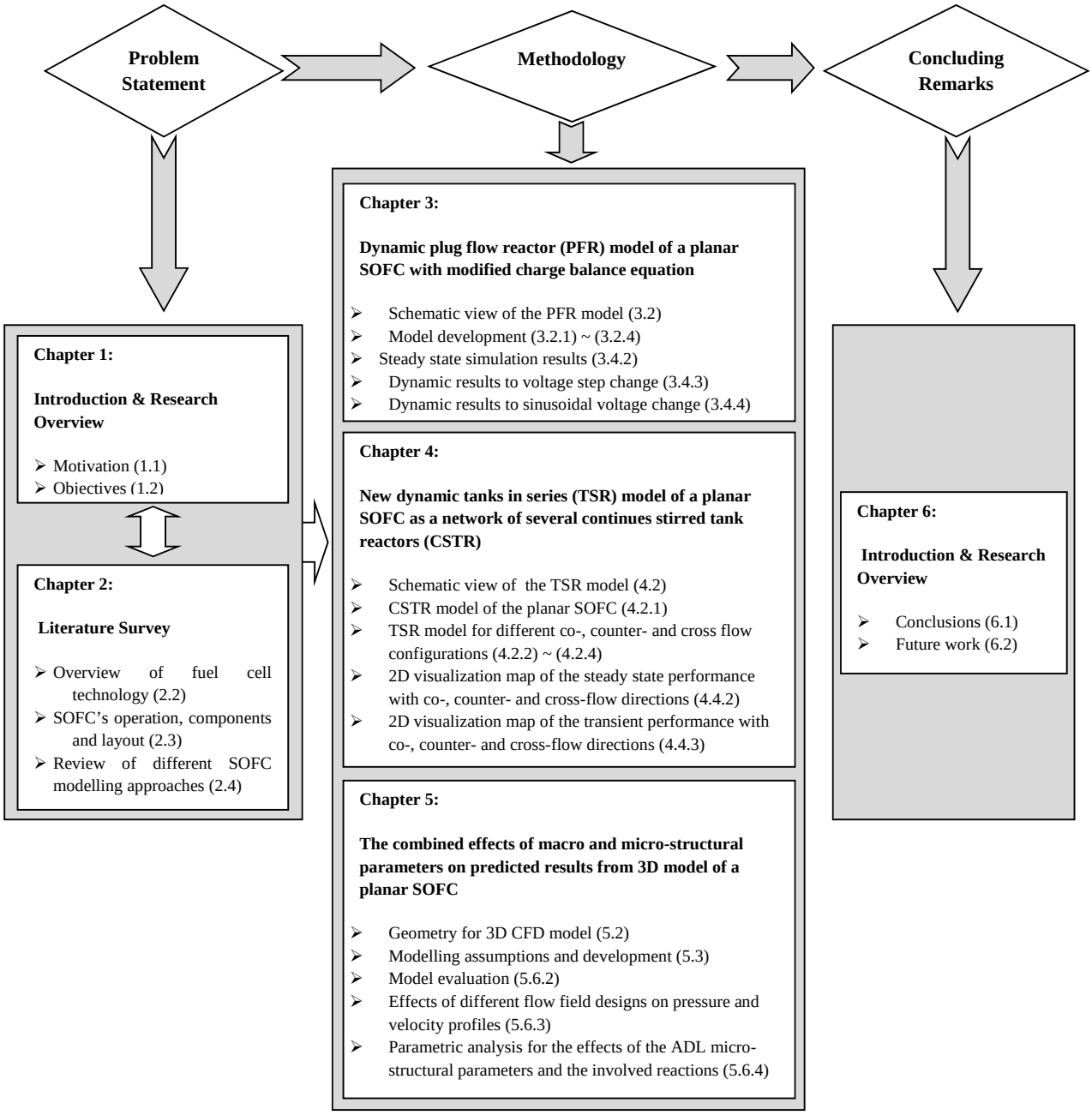

Figure 1.3 - Thesis organization

Chapter 2

Literature Survey and Problem Statement

2.1. Introduction

With respect to the important role of the physically based models in the path toward the fuel cell commercialization, this chapter aims at establishing a basis for the development of the models presented in Chapters 3 to 5. Therefore, it starts with a brief introduction to the fuel cell technology with emphasize on the solid oxide fuel cells followed by an explanation of the SOFCs' operation, components and layouts. After creating a basis for understanding the SOFC technology, a comprehensive review on different levels of the physically based SOFC models published in the open literature is performed. Finally, the controversial research areas in SOFC modelling will be highlighted.

2.2. Overview of the Fuel Cell Technology

A fuel cell is an electrochemical device that continuously converts chemical energy into electricity and some amount of heat for as long as fuel and oxidant are supplied. Therefore, fuel cells bear similarities both to batteries, which share the electrochemical nature of the power generation process, and to engines which unlike batteries will work continuously consuming a fuel of some sort [10, 11]. In view of this, researchers and engineers thought about commercializing the use of fuel cells for many practical issues in transportation, stationary power generation and portable applications [12]. To address these issues and the fundamental problems such as the manufacturing and material cost, reaction rate and fuel flexibility, a whole family of fuel cells are developed in different types, which are commonly characterized by the kind of the electrolyte being used and, simultaneously increasing operating temperature [13]. Table 2.1 presents a summary of kind of fuel cells in which the fuel types were listed as the crudest possible.

Table 2.1 - Different kinds of fuel cells and their characteristics[13]

Fuel cell type	Electrolyte	Charge carrier	Operating temperature	Fuel	Electric efficiency	Power range/ application
Proton exchange membrane fuel cell (PEMFC)	Solid polymer (Nafion)	H^+	50 - 100°c	Pure H_2 (tolerates CO_2)	35-45%	Automotive, CHP (5-250 kW), Portable
Alkaline fuel cell (AFC)	KOH	OH^-	60 - 120°c	Pure H_2	35-55%	<5 kW, niche markets (military, space)
Phosphoric acid fuel cell (PAFC)	Phosphoric acid	H^+	220°c	Pure H_2 (tolerates CO_2, approx. 1% CO)	40%	CHP (200 kW)
Molten carbonated fuel cell (MCFC)	Lithium & potassium carbonate	CO_3^{2-}	650°c	H_2, CO_2, CH_4, other hydrocarbons (tolerates CO_2)	>50%	200 kW-MW range, CHP & stand alone
Solid oxide fuel cell (SOFC)	Solid oxide electrolyte	O^{2-}	1000°c	H_2, CO_2, CH_4, other hydrocarbons (tolerates CO_2)	>50%	2 kW-MW range, CHP & stand alone

As it is shown in the table, among low temperature fuel cells, AFCs require pure hydrogen while PEMFCs and PAFCs can tolerate the impurities of reformate to some limited extends in the hydrogen rich fuels. Therefore, the application of AFCs has been only limited to the rich markets. PAFCs have been considered mainly for the medium scale power generating systems; however, in comparison with AFCs and PEMFCs, they achieve only moderate current densities [13]. PEMFCs capitalize on the essential simplicity of the fuel cells in which the electrolyte is a solid polymer with proton conductivity. The low operating temperature combined with the high electric efficiency enables PEMFCs for fast start up operation and makes them attractive for transportation applications and also for the small or midsize distributed electric power generation [14]. Despite to the low temperature fuel cells, SOFCs operate in the range of 600-1000°C[15]. The high operating temperature provides the high quality waste heat and activates the reaction rates in the presence of the low-cost catalysts [16], while it offers the opportunity for the internally reforming of the most hydrocarbon fuels without the need for the external reformer. Furthermore, the insensitivity of the high temperature fuel cells to the fuel contaminants enables them to utilize unconventional fuels such as biomass or coal gas [9]. This is in contrast to the low temperature fuel cells, which cannot accept the

hydrocarbon fuels and the risk of their poisoning by the fuel contaminants is very high. Co-production of heat and power, often known as combined heat and power system (CHP), is the other advantage of the high temperature fuel cells [6]. The recovery of the waste heat along with the production of electricity enables the total energy efficiency of such a system to be in the range of 85-90% [17]. Despite operating at high temperature, the SOFCs always stay in the solid state. This is not true for the MCFCs in which the benefit of the high operating temperature is offset by the corrosive nature of the liquid electrolyte. All these make SOFCs suitable as a prime power source for electricity generation in both central station power plants and decentralized generation units [9]. However, SOFC technology is still in embryonic infancy and as one can expect, some technical challenges such as the heat management and material design are associated with the high operating temperature[6].

2.3. SOFC's Operation, Components and Layout

Figure 2.1 illustrates the working principle of a typical hydrogen-oxygen fuelled SOFC in a planar geometry. Fuel is fed to the fuel gas channels and diffuses through the porous media of the anode electrode until it comes into contact with the electrode-electrolyte interfaces. Here, the anode accepts oxygen ions and converts them into H2O and electrons by reacting with hydrogen fuels. Electrons are introduced into the cathode via an external circuit. Similarly, at the cathode side, oxygen is fed to the gas channels and the electrochemical reduction of oxygen at the cathode-electrolyte interfaces leads to the production of the oxygen ions. The resulting ions migrate through the electrolyte to complete the circuit and sustain the half layers electrochemical reactions.

Based on the working principle, a typical SOFC consists of four basic components: dense electrolyte, anode and cathode electrodes and interconnects. Electrolyte is the central element of the fuel cell by which the operating temperature and other components' materials can be identified [4]. Due to its dense solid nature, it prevents penetrating of the gas species into it and then behaves like a gas separator. Moreover, the electrolyte functions as an ionic conductor enabling oxygen ions to flow from cathode to the anode sides. Therefore, an SOFC electrolyte material

should come across various requirements in order for the fuel cell to have a good performance and be stable over long time operation. Yttria Stabilized Zirconia (YSZ) is the most popular choice for the electrolyte material with the ionic conductivity of 0.02 $s.cm^{-1}$ at around 1000 K[16]. However, the research trend is toward reducing the operating temperature of SOFCs by using novel electrolyte material, such as LaSrGaMgO (LSGM), and by reducing the electrolyte thickness[18, 19].

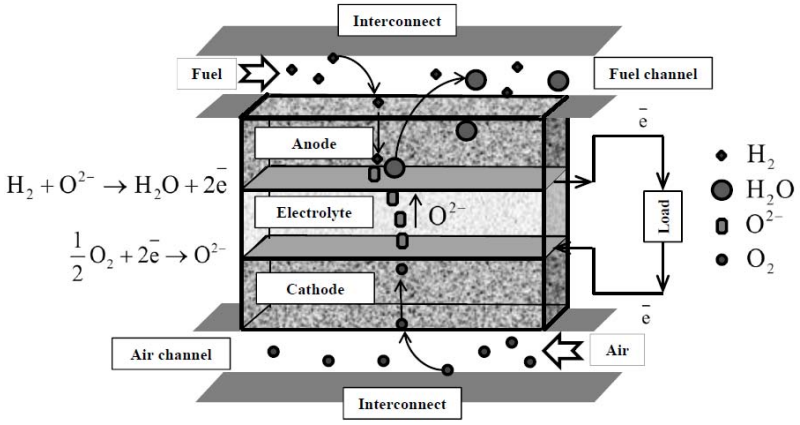

Figure 2.1 - Schematic view for the working principle of a planar SOFC

Due to high operating temperature, one of the important requirements for the SOFC materials is to have closely matching thermal expansion coefficients; therefore, all other components' materials are chosen based on the selection of the electrolyte film. The main function of the anode and cathode electrodes is to facilitate the reduction and oxidization reactions respectively, between the reactants (fuel and oxygen), ions and electrons. Therefore, they need to be conductive for the electrons and ions without being consumed or destroyed at the reactive environment and high operating temperature. In this regard, they are mostly made of the cermet materials. In this regard, Ni-YSZ cermet and Lanthanum Strontium Manganite (LSM) are the commonly used materials for the anode and cathode respectively [20, 21].

Furthermore, interconnect facilitates transport of the electrons between the electrochemically active layers at the anode and cathode electrodes and the external circuit. Additionally, it is in direct contact with the electrodes and all reactants. Therefore, interconnects need to be chemically and mechanically stable, electrically

conductive and its thermal expansion should be matched with the other components [22, 23]. Lanthanum chromite and ferric stainless steel are the most common ceramic and metallic materials used for interconnects [22, 24]. Furthermore, fuel and air gas channels are formed on interconnects to distribute the reactants across the anode and cathode electrodes. Therefore, different flow field designs are possible depending on the relative positioning of the fuel and air channels, which can greatly affect distribution of the reactants' concentration, temperature and reaction rate. Figure 2.2 shows the most common flow field configurations of a planar SOFC.

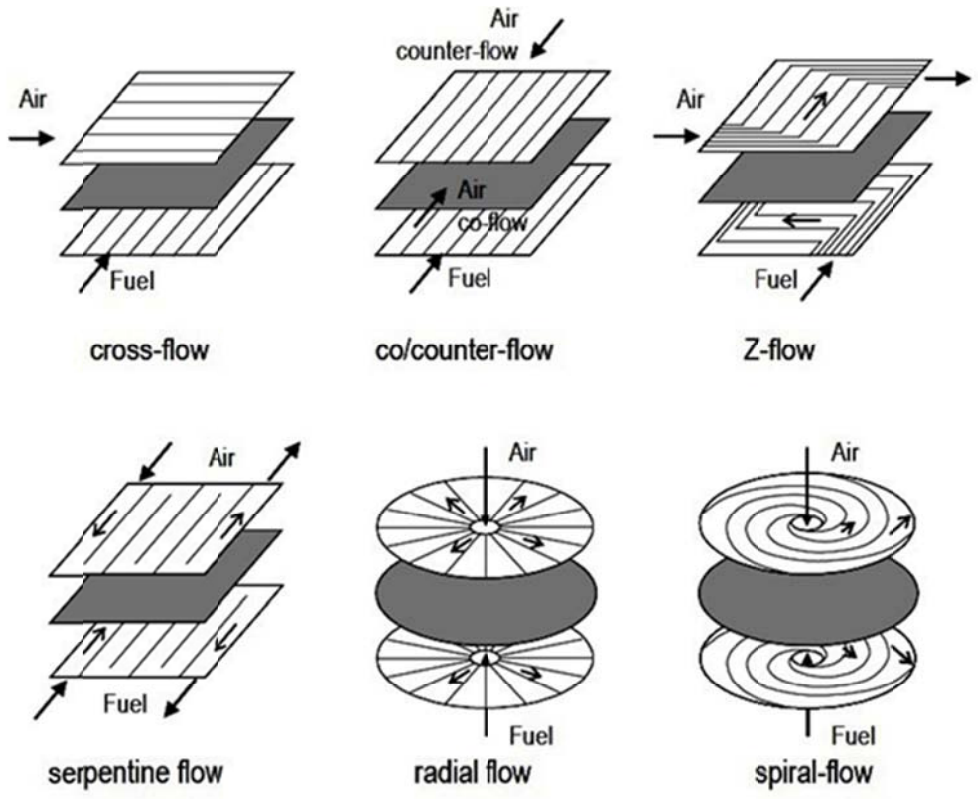

Figure 2.2 - Typical flow field configurations of a planar SOFC[25]

In addition to the above, the basic components can be fabricated into a variety of configurations among them the tubular and planar designs are the most common. Although the planar SOFCs are capable of achieving high power density, their design and development progressed slower than the tubular one because of the sealing problem that is associated with their manufacturing [26]. This problem is

almost solved by the improvements in materials and development of lower temperature SOFCs; therefore, the number of papers published on the modelling of the planar design has increased considerably [27].

2.4. SOFC Modelling Approach

For an SOFC, a relatively large number of physical, chemical and electrochemical processes occurring simultaneously can be described at different time and length scale [28]. The control of these processes requires primarily an understanding of SOFC physics and chemistry as well as the capability to modify one or more interdependent process parameters in a given direction [6]. In this regard, mathematical models are essential tools in examining and understanding the effects of various operating parameters and designs, as well as promising for the SOFC development. For the physically based SOFC models, the mathematical relationships are derived from the physical conservation laws and governing equations [9]; however, a challenge is to further improve multi-scale modelling approach for fuel cell design. A great number of papers can be found on SOFC modelling. Nevertheless, given the wide scope of applications, the model developed for various purposes are at different levels of complexity and details. Though there is no clear-cut delineation between the models and their classifications. Some general classifications are based on the model dimensionality, scales and predictions under steady state or dynamic operating conditions [9, 27, 29, 30]. In this section, a comprehensive literature review of the physically based SOFC models published in the open literature is presented. The models covered in this section are classified into three categories as follows.

2.4.1. Electrode Level Modelling

Recently, a promising alternative is studied extensively to reduce the operating temperature by adopting anode supported structure in SOFC instead of the electrolyte support. For a thinner layer of electrolyte film, SOFC can be operated in a moderate temperature of 600 - 800°c [31]. Furthermore, the commonly used Ni-based porous support provides internal reforming environment, which increases the applicability of the cell to methane-containing fuels without the need for converting

methane to hydrogen in an external reformer. Therefore, one of the important fields of the SOFC modelling at the electrode level is to explore the influences of the structural parameters on the reaction rates and transport processes inside the porous electrodes [32].

Thought the electrode level models was initiated by Costamagna et al. [33]. They developed a 1D model in which, the electrodes were treated as a mixture of the electronic and ionic conductor particles. Their model takes into account the morphological properties of the electrode on charge transport and the electrochemical reaction, while mass transfer through the porous electrode was neglected. That means they assumed uniform concentration of the reactants throughout the porous electrode. However, due to the consumption of the reactants at the reaction sites, this assumption is not valid. Chen et al. [34] presented 1D polarization model of a solid oxide fuel cell to show the sensitivity of the cell voltage drop to changes in thickness of the respective cell components. They used general form of the Butler-Volmer equation with constant exchange current density to calculate the activation overpotential. Additionally, the effects of both ordinary and Knudsen diffusions were considered in the mass transfers through the porous electrode. However, their model was developed under constant operating temperature and for the hydrogen fuel as the only anodic reactants. Another paper from Chen et al. [35] detailed the development of the same model. Lehnert et al. [36] developed 1D SOFC model to explain reactants' transports inside the anode as well as the electrochemistry and methane reforming kinetics under certain operating temperature. Their study highlighted the effects of the anode micro-structural parameters on the SOFC performance. Recently, Ni et al. [32] provided better understanding about the effects of the electrode microstructure and temperature on the coupled transport and reaction rates. In their study a 1D model was developed along the length of the electrode thickness. It was concluded that in methane fed SOFC, all overpotentials decrease with increasing of temperature. Moreover, it was found that both porosity and pore size grading can effectively improve the SOFC performance by significant reduction of the gas diffusional resistance within the porous electrodes. Furthermore, Yakabe et al. [37] presented a 3D model of a single unit planar SOFC to estimate the concentration polarization at the anode electrode. In their model, the flow phenomena were simulated using the finite volume method

and the distribution of the gaseous species was calculated. They found that the shift reaction effectively reduces the concentration polarization when the fuel utilization is high. To deeply understand the multi-scale transport processes and chemical reactions in the anode, Yuan [38] developed a 3D CFD model for a computational domain including of the porous anode, fuel gas flow channel and solid interconnect. The simulation results from that model reveals the combined effects of the reforming and electrochemical reaction rates on temperature distribution and transport processes of the anodic reactants. The similarity between the models developed by Lehnert et al. [36], Ni et al. [32], Yakabe et al. [37] and Yuan [38] was the consideration of the electrochemical reaction at the electrode-electrolyte interface while the internal reforming reaction assumed to happen in the anode porous structure. However, it is widely reported in the open literature that the electrochemical reaction not only occurs on the electrode-electrolyte interface but also extended to a distance of 10-50 μm from the electrolyte [39, 40]. Recently Hussain et al. [41] developed a 3D model describing the transport of multi-component gas mixture inside the anode. In their model, the computational domain was considered for a single fuel and air gas channels with the electrodes and electrolyte in between. More examples of the SOFC models, which allow sensitivity analysis on the performance of the cell with respect to the electrode micro-structural parameters can be found in references [42, 43].

On the electrode level, another important field of modelling concerns with the reaction kinetics at the electrode-electrolyte interfaces. In this regard, dynamic methods, such as the electrochemical impedance spectroscopy (EIS), are indispensable [44]. EIS is a powerful technique for fuel cell diagnosis which can give information on individual losses, including the electrochemical reaction kinetics, mass transfer and ohmic resistances [45]. In other words, when an excitation or perturbation signal (voltage or current) at multiple frequencies is imposed on a SOFC, a corresponding output signal, which is determined by the coupling of electrical, electrochemical, chemical and transport processes, gives the characteristic impedance. Therefore, in SOFC diagnosis, the EIS technique serves mainly as a tool to investigate the reaction mechanisms and, to optimize design and fabrication of the cell components. Though, EIS diagnosis consists mainly of three main elements: impedance data, impedance modelling and fitting algorithm [45]. In

general, EIS data are interpreted using impedance models, which play a decisive role in the process of the numerical impedance experiments. Among different impedance models, the equivalent circuit models (ECM) is phenomenological and easily accepted and understood; therefore it has been used extensively to characterize the physiochemical processes in SOFCs [46, 47]. However, the equivalent circuit approach is primarily electrical model and although it gives a good picture of the contribution of different loss mechanisms but these voltage losses do not represent physically meaningful potential steps in the path along the PEN structure thickness [48, 49]. Additionally, there is no straight forward mathematical correlation between the parameters of ECMs and the parameters of SOFCs [45]. To address these problems, development of the physically based dynamic models from the conservation equations is very helpful to simulate the electrochemical impedance spectra. Zhu and Kee[50] developed a physically based 1D transient model including species transport in porous electrodes, elementary heterogeneous chemical reaction, ion conduction and electrochemical charge transfer for simulating electrochemical impedance spectra. In this model spatial variation of the species concentration at the fuel and air compartments were neglected, porous media transport was represented by the dusty gas model and the electrochemical charge transfer was modelled with a modified Butler-Volmer formulation. However, the effects of double layer capacitances at the electrode-electrolyte interfaces were neglected. Similarly, Bessler[51] developed a new computational approach for simulating impedance spectra and modelled elementary reactions and diffusion processes at SOFC anode as a system of physically derived conservation equations and without considering the effect of the electrode-electrolyte double layer capacitances. This model yields chemical and physical parameters without the necessity of applying equivalent circuit models. It focused on the (electro-) chemical and mass transport contributions to the impedance that was also referred to as the faradic impedance. In another research, Hofmann and Panopoulos[49] presented detailed dynamic model for a planar SOFC to simulate steady state and dynamic performances, with a specific capability of simulating the electrochemical impedance spectra. However, distributed charge transfer equation has not been taken into account, so that the charge transfer and potential steps only occur lumped at the interfaces of the electrodes and electrolyte membrane and the physical meaning of the linear current density has not been included. Therefore, in line with the real physics, it is

necessary to include the distributed effects of the electrode-electrolyte double layer capacitance to the dynamic response of the current density at different layers.

2.4.2. Cell and Stack Level Modelling

In addition to the electrode-level models, a large number of papers for physical modelling of the cell and stack have been published in the open literature. These models have been developed from the physical principles to investigate the cell and stack internal processes and broadly classified from three dimensional (3D) to the most simplified zero dimensional (0D). In this section, a brief review of the physically based cell and stack level models will be presented.

In SOFCs, the fuel utilization and the average cell temperature can be controlled by the reactants' delivery rates and the gas inlet temperature [9]. Although increased fuel flow tends to increase uniformity of the reactants' distribution along the electrode active area, it decreases fuel utilization [7]. Additionally, it is possible to have a uniform flow distribution by insuring that, the pressure drop in the inlet and outlet manifolds is much lower than that in the gas channels [52]. Therefore, managing the pressure drop, gas flow and the inlet temperature are the crucial factors, which in turn affect the overall performance of the cell and stack [9]. With respect to flow uniformity, the geometrical design factors such as the number of manifolds and their structure, gas channel design and overall gas flow pattern are the important parameters to be considered [53]. In this regard, Koh et al. [53] developed a hydrodynamic model for the U-type and Z-type gas flow patterns in a typical fuel cell stack. Using that model, the effects of the geometrical factors on pressure and flow distribution in fuel cell stack were calculated. They found that incorrect manifold design has more significant effect on pressure profile, which may consequently results in flow maldistribution. Furthermore, Maharudrayya et al. [54]applied analytical approach to a typical fuel cell distributor plate to analyse flow distribution and pressure drop in Z- and U- type parallel channel configurations. From their study, it was shown that channel design and dimension of the inlet and outlet headers can affect the flow uniformity as well. In another research, Maharudrayya et al. [55] conducted 2D CFD simulation to analyse the flow structure and pressure loss for the laminar flow through serpentine channels and over a range

of curvature and aspect ratios. They found that curvature has a significant effect on occurrence of the flow separation in the bend regions. Liu et al. [56] and Li et al. [57] studied the effect of the multiple levels of the channel bifurcation structure and dimensions on the uniformity of flow distribution with 2D CFD models. However, development of 3D model of the flow field design with realistic boundary condition is a more reliable approach for the flow distribution analysis [3]. In this regard, Bi et al. [52] developed a 3D CFD model to perform intensive CFD calculation for analysing flow distribution in planar SOFC stack without including the effects from chemical and electrochemical reactions. They found that the ratio of the inlet to outlet manifold width is a key geometrical parameter influencing the flow uniformity in stack. Huang et al. [58] investigated flow uniformity in various flow field design and its influence on the performance of a planar SOFC experimentally and numerically. In their study, several 3D CFD models were established to simulate the hydraulic experiments and to evaluate the performance of a single cell stack. Their models were built for different design of interconnects and over the wide range of the hydraulic Reynolds number. It was concluded that new flow field design with two inlets – one outlet manifold is superior to the one inlet – one outlet design proposed by Yakabe et al. [59]. Additionally their new design can effectively improve the degree of flow uniformity in interconnects, temperature uniformity of the PEN structure and overall performance of the cell. In another study, Qu et al. [60] analysed the electrochemical processes of a planar SOFC to evaluate the performance of the proposed SOFC design with corrugated bipolar plates serving as the gas channels and current collector. Additionally, Danilov and Tade[61] presented a 3D CFD model of a planar SOFC to reflect the influences of various factors including different anode flow field design and reaction kinetics on the overall performance of the cell. According to Liu et al [56], it is expected that efforts for developing new flow fields to improve the uniformity of the flow distribution remain as an interesting topics for engineers and researchers. However, in addition to the importance of the uniform flow distribution, operating conditions and different fuel and air flow configurations also influence SOFC performance. For example, Ferguson et al. [62] and Recknagle et al. [7] introduced a 3D model for a typical planar SOFC, which allows computation of the local distribution of temperature, current density and species concentration under the effects of different co-, counter- and cross-flow of air and fuel configurations. Xia et al. [63] developed a

3D CFD model to investigate the effects of the inlet operating parameters such as the inlet flow rates and temperature on the performance of a one cell stack of the planar SOFC under the influence of the co- and counter flow configurations. Furthermore, Janardhanan and Deutschmann[64] developed a 2D CFD model for an internally reforming anode supported SOFC. Their study mainly focused on the analysis of detailed chemical processes within the anode, electrochemical processes and losses of SOFC running on CH4 rich fuel under the isothermal operating condition.

The solid oxide fuel cells, like many other process equipment, are typically designed by considering only their steady state characteristics. However, dynamic performance is crucial as well in designing fuel cells that have a long lifetime and then, in the past few years, dynamic modelling has gained importance [30]. For example, Achenbach [65] presented three dimensional and time dependent model of a planar SOFC to discuss the effect of different co-, counter- and cross flow configuration on distribution of the current density and solid temperature across the cell. In his study, the response of the cell voltage to a load step change was analysed. Li et al. [66] developed a two dimensional model of a direct internal reforming SOFC stack operating with cross flow configuration. In their study, not only the steady state performance analysis but also dynamic responses to step changes in fuel flow rate, air flow rate and stack voltage were discussed. Furthermore, it was shown that the dynamic responses are different at each point of the stack. Additionally, Serincan et al. [67] developed a transient 2D CFD model for a tubular SOFC. They investigated dynamic responses of the current density to the failure in fuel supply and step changes in the cell voltage.

As it was shown, three and two dimensional models are typically developed to study the combined impacts of the fuel and air flow directions, flow field design, reactions and operating conditions on the overall performance of the cell and stack. In these models, the processes occurring within the PEN structure have been greatly simplified and they are usually solved using the commercial CFD packages. Although CFD techniques are powerful tools in the study of flow and transport phenomena inside fuel cells, such approaches for the complete SOFC modelling, including chemical and electrochemical reaction mechanisms, lead to highly

complex descriptions, which are time consuming with respect to set up and simulation. As a result, although there is limited number of 3D and 2D models for transient study; they are not practically applicable for SOFC system analysis, dynamic simulations and for control purposes [68]. In this regard, quasi 2D, reduced 1D, and lumped parameter SOFC models seemed to be more promising.

Quasi 2D models are popular since they reduce the computational time. In such models, 1D gas flows in the gas channels are coupled with transverse transport of the reactants' species in the porous electrodes by using the boundary conditions at the gas channel-electrode interfaces [69]. For example, Zhu et al. [70] presented a quasi 2D model for a typical anode supported SOFC to analyse heterogeneous chemistry and electrochemistry with the assumption of isothermal operating condition. Their simulation results showed the capability of implementing elementary heterogeneous chemical kinetics in the form of multi-step reaction mechanisms into the SOFC model. Lai et al. [71] and Burt et al. [72] presented quasi two dimensional models for the efficient computation of the current density, species concentration and temperature distributions in a planar SOFC stack and under the steady state operating condition. In their models, 2D control volume approach was implemented to simulate the stack physics while maintaining adequate computational speed. However, in the model presented by Burt et al. [72], simulations were done in a parallel computing environment that reduced the computational time more significantly. Xue et al. [73] used the same numerical approach for a single tubular SOFC unit to simulate steady state performance and transient characteristics of the cell under time varying voltage. Although simulation results from quasi 2D models have better accuracy than those from 1D and 0D SOFC models, the simulation results were mainly reported along a single axis of the computational domain.

In 1D models, which are an improvement over the existing 0D ones [74], the cell is represented as a line, gas channels are modelled as the plug flow reactors and the PEN structure is considered as a thin layer separating the fuel and air channels [9, 69]. Aguiar et al. [75, 76] proposed a 1D SOFC dynamic model to investigate transient behaviour of the co- and counter flow SOFC to load step changes and the impact of the operational parameters on the steady state performance. Their model has been developed for the mass and energy transfer processes with an electrochemical sub-

model to relate reactants' concentration and temperature to the voltage, current density and other cell variables. In another study, Yingwei et al. [77] developed 1D dynamic model of a planar methane fuelled SOFC to investigate steady state performance and dynamic responses of temperature, current density and voltage to step changes in load and the inlet gas flow rates while transient response of the charge transfer process was neglected as well. They found that the inlet air flow rate has a great impact on the cell temperature distribution and can be used as the manipulated parameter for temperature control. Cheddie and Munroe [74] presented a 1D dynamic SOFC model by developing a system of governing differential equations over 1D control volume. In their study the effects of the number of nodal points on the computational time and temperature prediction were analysed. Additionally, temperature and voltage responses to the load step changes were investigated. Similarly, Wei Kang et al. [78] developed a reduced 1D dynamic model of a planar methane fuelled SOFC by adopting control volume approach along the gas flow direction. Furthermore, interconnects, gas channels and the PEN structure were integrated together, the current density distribution was considered to be uniform within the SOFC and the cell voltage was determined by the average gas molar fractions and cell temperature. The results from the reduced model were evaluated with a detailed 1D and simplified lumped parameter SOFC models. They concluded that accuracy of the reduced model was not affected significantly by the simplifications while it was an improvement over the lumped parameter model.

In the path toward the model simplification, 0D models are the simplest ones, in which spatial variations are not taken into account and spatial averaging in all directions is performed. For example, Wang and Nehrir[79] developed a physically based dynamic model for a tubular SOFC in which, the components' diffusion were described by the Stefan-Maxwell formulation and the gas channels were modelled as the well mixed reactors. In their study, the dynamic characteristics of the model were investigated in small, medium and large time scales, from millisecond to minutes and then, double layer charging and discharging effects were modelled by the equivalent circuit approach. The work of Campanari[80] and Lin et al. [81] are the other illustrations of the application of this type of SOFC models for the cell performance investigation. More examples of the zero dimensional SOFC models will be reviewed through the following system level models.

Once again, due to the fast response of the charge transfer process to the step change in voltage or current density, the similarity between most of the cell and stack level dynamic models is that, the transient response of the charge transfer process has been neglected and with few exceptions it was considered as the lumped parameter models. However, for precise calculation of the transient response of the electrochemical reactions, especially when the cell is subjected to a high frequency sinusoidal voltage change, it is necessary to consider unsteady state equation for the charging process of the electrical double layer along with the electrode-electrolyte interfaces [30].

2.4.3. System Level Modelling

System level models play an important role in the development of fuel cells especially in the hybrid SOFC systems [9]. By definition, any combination of a fuel cell and a heat engine can be considered as the hybrid fuel cell system [82]. For the SOFC system modelling, emphasize is focused on interaction of the fuel cell with the other components of the system and not investigation of the inner working of the cell and stack. Therefore, lumped parameter SOFC models are more suitable for system level analysis. Hybrid SOFC systems have a wide range of possible applications, which have been studied extensively by the system level modelling. A comprehensive literature review of modelling of the SOFC system can be found in [27, 29]. However, in this section some of them from the open literature will be reviewed.

One of the primary aims of any system simulation is to evaluate the effects of various parameters on the system performance. For example, Suther et al. [83], developed a steady state thermodynamic model of a hybrid SOFC-GT system in the commercial process simulator, Aspen Plus, which incorporates a zero dimensional model for the planar SOFC stack. Using the developed model, they investigated the impact of some operating parameters such as system pressure, SOFC operating temperature and SOFC fuel utilization factor on the specific work output and efficiency of the hybrid cycle. From thermodynamic perspective, Chan et al. [84] presented a steady state model for a natural gas fed SOFC-GT power generation system. Their model was developed in the general purpose mathematical software,

MATLAB and performed the first law of thermodynamics energy analysis with the particular attention on the effects of operating pressure and fuel flow rate on the performance of the components and system. Based on that study, the authors developed the model further for possible part load simulation [85]. Calise et al. [86] performed a detailed exergy analysis of a highly coupled SOFC-GT hybrid plant using the MATLAB toolboxes. They gave special attention to the sources of inefficiency and analysed their variations with respect to different operating pressure, fuel utilization, fuel to air and steam to fuel ratios and current density. To study the suitability of the SOFCs for aerospace applications, a zero dimensional model for the SOFC stack was also used in conjunction with a propulsion system by Freeh et al. [87]. However, not only steady state but also dynamic behaviour and load characteristics are the key issues that should be addressed for the SOFC based energy systems, which have been considered as the most promising technology in the market of distributed power supply and mobile applications. Therefore, with respect to these particular application, the main goal is to design suitable control strategy to address improvement of transient behaviours, rapid load following, smooth system operation and safety in the desired operating range [88]. For example, Zhu and Tomsovic[89] presented a simplified dynamic model of the SOFC micro turbine system in Laplace time domain to evaluate dynamic performance and control strategy. Kimijima and Kasagi[90] studied part load of a recuperated SOFC-GT cycle, using a 0D SOFC model under variable and fixed shaft speed operation. They pointed out that variable shaft speed operation is favourable in terms of part load performance.

As it was shown above, modellers generally use two different approaches for system level modelling. In the first approach, models for different components of the system can be developed in programming languages such as MATLAB/Simulink platform to solve the governing equations of the system. In the second approach, they develop the stack level SOFC model by themselves and take advantage of commercial software such as Aspen Plus, Hysis and Pro II process simulators to model the conventional components of the system. In both approaches, due to the objective and complexity of the SOFC system models, the SOFC sub-models mostly focused on the thermodynamic aspect and the associated electrochemical processes or developed as a lumped parameter model (0D), which

is the most simplified representation for real physics of the SOFC stack. Therefore, even with appropriate validation, accuracy of the simulation results is questionable. To address this matter, there are some publications that used multidimensional approach to model SOFC stack. For example, Magistri et al. [91] studied simplified versus detailed SOFC stack models and how they affect the performance of the SOFC system. They emphasized the importance of the simplified SOFC model for hybrid system design and detailed model for complete description of the SOFC internal behaviour. Palsson et al. [92] developed a steady state model for a hybrid SOFC-GT system in Aspen Plus by using 2D model of a planar SOFC as a user defined unit, which was integrated with other built-in models for the standard components of the system. In another research, Song et al. [93] developed a quasi 2D steady state model for the SOFC stack to investigate the impacts of system parameters on the performance of the tubular SOFC-GT system. Furthermore, the effect of the co- and counter flow configurations on the system performance was evaluated in that study. With respect to dynamic simulation, Stiller et al. [94] presented a detailed dynamic model of a tubular SOFC system integrated into a simple recuperated GT cycle to investigate steady state and dynamic behaviour of the system to rapid load changes. In their model, the SOFC sub-model was spatially discretised and fully dynamic in terms of mass and heat transfer phenomena. Gas flows were treated as 1D plug flows, while the SOFC solid structures were modelled by a 2D discretization scheme in axial and radial directions.

2.5. Summary

SOFC modelling is performed at various levels, from the electrode level to the cell and stack followed by the system level.

Dynamic characteristics are crucial in fuel cell design. In general, dynamic models at the electrode-level are essential for the electrochemical impedance analysis while at the cell, stack and system level modelling, they are used to investigate transient responses to the step changes in voltage, current and operating conditions at the inlet boundaries. In spite of different applications for the SOFC dynamic models, in most of them, the effect of the charge double layer capacitance on the transient characteristics has been neglected and with a few exceptions it has been considered

as the lumped parameter model and combined with the electrochemical reaction potential steps at the electrode-electrolyte interfaces [49-51, 79]. However, the current density that is measured at the current collector is the sum of the faradic current due to charge transfer electrochemistry, calculated mainly by the Butler-Volmet equation and the current due to charging or discharging of the electrical double layers upon transient conditions [48]. Thus, the existing models cannot reflect the actual physics of the charge transfer processes at the electrode-electrolyte interfaces while one of the main goals of the various modelling approaches is to predict the relationship between the cell voltage and current density under different operating conditions. Although the response of the charge transfer process to the step change in voltage or current density is instantaneous but for precise calculating of the transient response of the electrochemical reactions, especially when the cell is subjected to a varying high frequency sinusoidal voltage or current (that is the case for the impedance analysis), it is necessary to consider the effect of the electrode-electrolyte double layer capacitance. Therefore, an improved understanding is still necessary for physically characterizing the current densities at the electron and ion conducting media upon transient conditions.

In addition, as it comes from the above literature review, maintaining high power output, maximizing operating life and keeping high efficiency are the most important issues regarding the operation of a SOFC. Therefore, we require proper design of the cell and stack as well as the control system. To address this, even though a limited number of 3D and 2D SOFC models were developed to address transient analysis, spatial consideration into SOFC dynamic analysis has been given very little attention from the research community. Furthermore, such models have inherent complexity that makes them computationally intensive and very time consuming. Therefore, they are not practically applicable for SOFC system analysis, dynamic simulations and control purpose [68]. For that reason, quasi two, reduced one and zero dimensional SOFC reactor models seemed to be more promising. However, not all reactors are perfectly mixed, nor do all reactors exhibit plug flow behaviour. Furthermore, the effects of the flow field design, different fuel and air flow configurations and the spatio distribution of the key variables such as temperature, current density and species concentrations cannot be considered in these simplified models. Therefore, even with appropriate validation, accuracy of

the simulation results is questionable and we need a new SOFC model with less complexity and computational dexterity that falls between the most simplified lumped and multi-dimensional models found in the literature.

Finally, as it was shown, all reactions, geometric and micro-structural parameters influence transport processes and fuel cell performance in a complex manner and different ways. However, investigations of the micro-structural effects have been restricted mainly to one-dimensional models, which have been developed along the thickness of the PEN structure and cannot represent the performance of a complete cell; or models with higher dimensionality for a single fuel and air gas channels which do not capture the influences of the geometrical factors properly. On the other hand, the existing 2D and 3DSOFC models for a complete cell or stack are mainly developed to analyse the effects of different flow field design and operating conditions on the flow distribution patterns and steady state performance. Furthermore, they have mainly being built for a hypothetical geometry and validated with the experimental data from the literature that may belong to different geometries. In view of this, the previous studies have examined the effects of geometrical factors and microstructural parameters independently but not simultaneously. Therefore, there is a lack for a 3D CFD model of a real industrial SOFC to facilitate analysis of the effect of different flow field design on pressure and velocity profiles and investigate the distribution of temperature, species concentration and reaction rates under the combined influences of the micro-structural parameters and geometrical factors.

All these provide a rationale for doing further improvement over the existing multi-scale SOFC models that is detailed in the next chapters.

Chapter 3

Dynamic Plug Flow Reactor Model of a Planar SOFC with Modified Charge Balance Equation

3.1. Introduction

With respect to the wide range of applications for the SOFC dynamic models, it is the intention of this chapter to develop a modified physically based plug flow reactor model of a planar SOFC for the steady state and transient performance analysis. Special emphasis is put on using a modified expression for the charge balance equation as the boundary condition between the electrode and electrolyte interfaces. This model can get the capacitor effect of double layers and prediction of steady state and dynamic performances are accomplished in line with the real physics of the charge transfer process.

3.2. PFR Model Development

Figure 3.1 shows the schematic diagram of the planar SOFC as used in this model that consists of interconnect, fuel and air gas channels, cathode and anode electrodes with an ionic conducting electrolyte that is sandwiched in between. For the simplest case of the hydrogen fuel and air system, the charge transfer processes taking place at triple phase boundaries, yield the following half-cell electrochemical reactions:

$$H_2 + O^{2-} \rightarrow H_2O + 2\bar{e} \qquad (3\text{-}1)$$

$$1/2O_2 + 2\bar{e} \rightarrow O^{2-} \qquad (3\text{-}2)$$

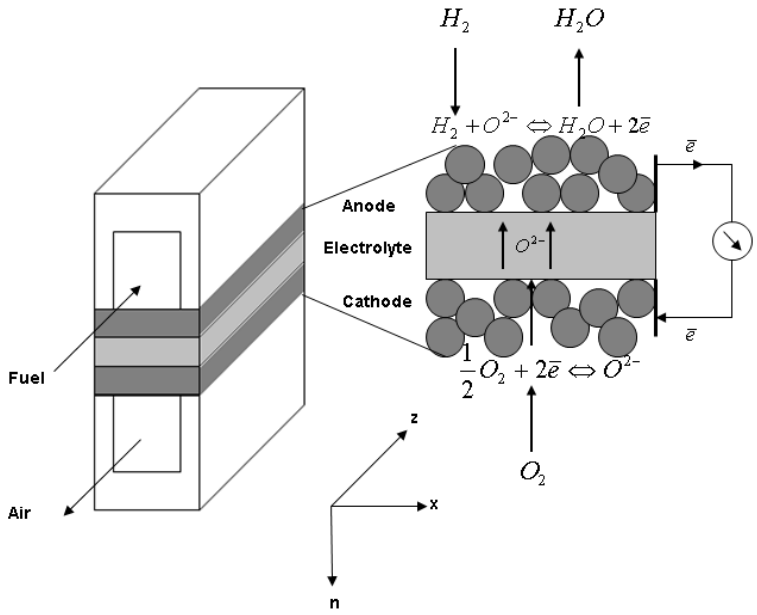

Figure 3.1 - Schematic view of a planar SOFC in PFR model[8]

Additionally, the model developed here is used for the potentiostatic operation of the cell and the assumptions for the model are listed below:

- Triple phase boundary (TPB) is located only at the electrode-electrolyte interface where the charge transfer processes occur.
- Plug flow condition is assumed within the fuel and air channels. Thereby the gas temperature, velocity and composition are only changed along the z-coordinate.
- Electrolyte is an oxygen ion conducting media without current leakage.
- Transverse transport in porous media is taken into account by the component mass balances between the gas channels and electrode-electrolyte interfaces.
- Pressure drop along the gas channels is neglected and ideal gas behaviour is assumed within fuel and air channels.

Based on the above assumptions, transport equations are developed for mass, energy and charge balances along the main flow directions of fuel and air channels and discussed as follows:

3.2.1 1D Mass Transport Equation

The one dimensional transient model for the fuel and air channels may be considered with the following species continuity and overall continuity equations in which, the negative sign is used for the fuel flow [95] and the positive sign is corresponding to the counter current mode of the air flow [96]:

$$\frac{\partial(C^{f,a} y_i^{f,a})}{\partial t} = \pm \frac{\partial(\vec{u}^{f,a} C^{f,a} y_i^{f,a})}{\partial z} + \frac{\nu_i \left| i_F^{A,C} \right|}{2FH^{f,a}} \tag{3-3}$$

$$\frac{\partial(C^{f,a})}{\partial t} = \pm \frac{\partial(\vec{u}^{f,a} C^{f,a})}{\partial z} + \sum_i \frac{\nu_i \left| i_F^{A,C} \right|}{2FH^{f,a}} \tag{3-4}$$

Here, the independent variables are time and the length along gas channels (z), while the dependent variables are the tensor velocities ($\vec{u}$) and species mole fractions (y_i). Although pressure could be determined by solving momentum equation, the pressure variations along a channel are sufficiently small so that the pressure is considered as a constant parameter [95]. Moreover, Faraday's law relates the flux of reactants and products to the Faradic current densities ($i_F^{A,C}$) arising from the half-cell electrochemical reactions.

3.2.2 1D Heat Transport Equation

In a fuel cell, current and temperature distributions are strongly coupled [97]. Thus consideration of the energy balance is essential. In this model, equations for the energy balances are mostly acquired from the work of Aguiar and co-workers [76]; however, some changes were made to adopt the counter flow case. The thermal flux was supposed to be conductive in solid phases including the PEN structure and interconnects while it was considered to be convective in the gas flow direction and between the gas channels and solid parts. That is due to the fact that the thermal conductivity is much higher in the solid regions than in the fluid phases [74]. The model complexity was reduced by neglecting the variation of the reactants' heat capacities and the heat transfer coefficients as considered in [76, 96]. Therefore, the governing energy equations for the fuel and air channels are:

$$C^f c_p^f \frac{\partial T^f}{\partial t} = -\vec{u}^f C^f c_p^f \frac{\partial T^f}{\partial z} + \frac{\hbar^f}{H^f}(T^{PEN} - T^f) + \frac{\hbar^f}{H^f}(T^I - T^f) \quad (3\text{-}5)$$

$$C^a c_p^a \frac{\partial T^a}{\partial t} = \vec{u}^a C^a c_p^a \frac{\partial T^a}{\partial z} + \frac{\hbar^a}{H^a}(T^{PEN} - T^a) + \frac{\hbar^a}{H^a}(T^I - T^a) \quad (3\text{-}6)$$

Here, H is the gas channel height; $\hbar^f$ and $\hbar^a$ are the heat transfer coefficients between the gas channels and solid structures; T^f and T^a are the fuel and air temperatures; T^{PEN} and T^I are the temperature of the PEN structure and interconnect; and $c_p^{f,a}$ is the specific heat capacity of the gas mixture in fuel and air channels.

$$c_p^{f,a} = \sum_i y_i^{f,a} c_{p,i} \quad (3\text{-}7)$$

In planar SOFCs, more often the flow channels have the large aspect ratios (length to height), which are generally reported in the range of 100:1 on the cathode side and 200:1 on the anode side. Therefore, the view factors are small enough to neglect the radiation heat transfer between the PEN and interconnect surfaces[7]. However, due to the geometry of the SOFC that is considered in this model, the aspect ratio is placed in the range of 20:1 that may allow some amount of heat radiation to occur. In view of this, the effect of radiation heat transfer is taken into consideration for the PEN and interconnects temperatures.

$$(\rho c_p)^{PEN} \frac{\partial T^{PEN}}{\partial t} = k^{PEN} \frac{\partial^2 T^{PEN}}{\partial z^2} - \frac{\hbar^f}{\delta^{PEN}}(T^{PEN} - T^f) - \frac{\hbar^a}{\delta^{PEN}}(T^{PEN} - T^a) + \frac{R_h^{rad}}{\delta^{PEN}} + \frac{R_h^{elec}}{\delta^{PEN}} \quad (3\text{-}8)$$

$$(\rho c_p)^I \frac{\partial T^I}{\partial t} = k^I \frac{\partial^2 T^I}{\partial z^2} - \frac{\hbar^f}{\delta^I}(T^I - T^f) - \frac{\hbar^a}{\delta^I}(T^I - T^a) - \frac{R_h^{rad}}{\delta^I} \quad (3\text{-}9)$$

$$R_h^{rad} = \sigma_{EB}\left[(T^I)^4 - (T^{PEN})^4\right] / \left[\frac{1}{\xi^I} + \frac{1}{\xi^{PEN}} - 1\right] \quad (3\text{-}10)$$

$$\delta^{PEN} = \delta^A + \delta_{elyt} + \delta^C \quad (3\text{-}11)$$

Here, δ^A δ^C and δ_{elyt} are thicknesses of the anode, cathode and electrolyte respectively; ξ is the emissivity; and R_h^{elec} is the heat generation, which consists of

the enthalpy changes of the electrochemical reaction and the electrical work from the cell.

$$R_h^{elec} = i_{cell}\left(\frac{\Delta H^{elec}}{n_e F} - E_{cell}\right) \quad (3\text{-}12)$$

Here, ΔH^{elec} represents the enthalpy change for the overall electrochemical reaction at the electrode-electrolyte interfaces; i_{cell} is the cell current density at each point; n_e is the number of electrons transferred through the reaction; F is the Faraday constant and E_{cell} is the cell voltage.

3.2.3 1D Charge Transport Equation

When an electrical load is applied to a composite electrode, the coupling of the electric and ionic conduction properties with electrochemistry, double layer charging or discharging and gas phase transport will lead to a characteristic distribution of the local potential steps [48]. Figure 3.2 presents a schematic for the electric potential distribution of an SOFC.

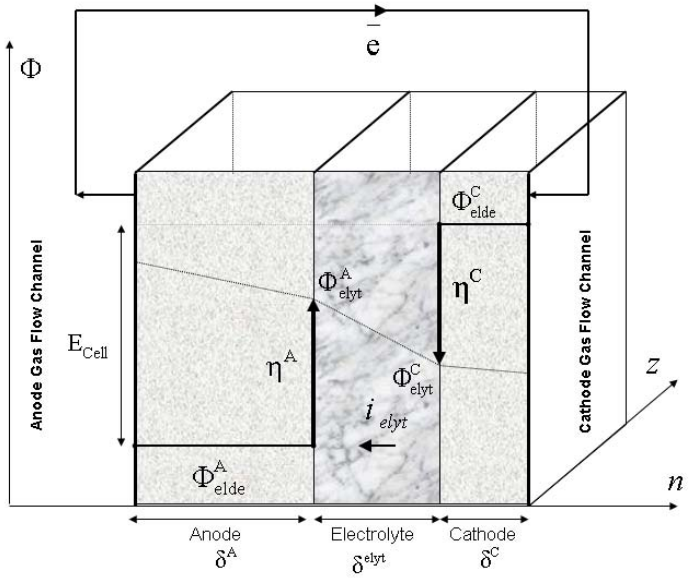

Figure 3.2 - Electric potential distribution in a polarized SOFC with porous electrode[48]

The measured cell voltage is given as the difference between the electric potentials of the current collectors at the anode and cathode sides [96].

$$E_{cell} = \Phi^{C}_{elde} - \Phi^{A}_{elde} \tag{3-13}$$

In addition, the anode and cathode electrodes are at different potentials due to the following electric potential steps at the anode-electrolyte (η^{A}) and cathode-electrolyte (η^{C}) interfaces [48].

$$\eta^{A} = \Phi^{A}_{elde} - \Phi^{A}_{elyt} \tag{3-14}$$

$$\eta^{C} = \Phi^{C}_{elde} - \Phi^{C}_{elyt} \tag{3-15}$$

Here, Φ_{elyt} is the electrolyte potential just beyond the electrodes. To calculate different overpotentials, we need to solve equations (3-13) to (3-15). In this regard, an additional expression is required to describe the variation of η^{A}, and η^{C}. In view of this, the electromagnetic theory postulates the following charge balance equation at the interfaces between two arbitrary phases [98].

$$\frac{\partial Q}{\partial t} = -\nabla . i_L - a_n (i_{n1} - i_{n2}) \tag{3-16}$$

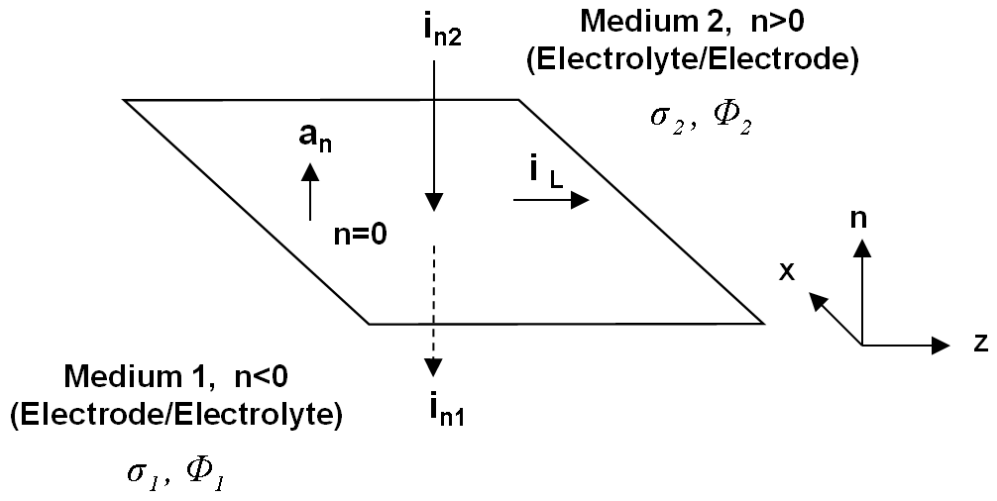

Figure 3.3 - Schematic view of the charge boundary conditions at the interface between two arbitrary media[98]

As it is shown in Figure 3.3, equation (3-16) states that, at any point on the boundary, the time derivative of the surface charge density (Q), is equal to the negative sum of the dimensional divergence of the linear current density (i_L) and differences between the components of the current densities normal to each sides of the boundary (i_{n1} and i_{n2}). In equation (3-16), let the quantities pertinent to medium 1 and 2 be denoted by subscripts 1 and 2 respectively and a_n be the unit normal vector to the surface and directed into medium 1. In addition to above, the electrode-electrolyte interfaces behave like a capacitor in which the surface charge density depends on the potential differences across this double layer. Charge or discharge rate for the anode-electrolyte and the cathode–electrolyte boundaries can be represented as follows [99]:

$$\frac{\partial Q^{A}}{\partial t} = C_{dl}^{A} \frac{\partial}{\partial t}(\eta^{A}) \tag{3-17}$$

$$\frac{\partial Q^{C}}{\partial t} = C_{dl}^{C} \frac{\partial}{\partial t}(\eta^{C}) \tag{3-18}$$

Here C_{dl}^{A} and C_{dl}^{C} are the anodic and cathodic specific double layer capacitances for which, the values reported by Hendriks et al. [100] were used. Furthermore, from the Ohm's law and with respect to the linear current density on each side of the boundary between two different mediums, it can be written as [101]:

$$i_{L,1.}\, r_{L,1} = -\nabla \Phi_1 \tag{3-19}$$

$$i_{L,2.}\, r_{L,2} = -\nabla \Phi_2 \tag{3-20}$$

$$(r_L)_{1,2} = \left(\frac{1}{\delta\, \sigma}\right)_{1,2} \tag{3-21}$$

Here, r_L is the resistance of the boundary between the electrode and electrolyte phases. With attention to the physically uniqueness of the linear current density on the boundary between the electrode-electrolyte and considering the large difference between the electrode and electrolyte conductivities, subtracting equation (3-19) from equation (3-20) results in the following expression for the linear current

density on the boundary between the anode-electrolyte and the cathode-electrolyte respectively:

$$i_L^A = \frac{1}{r_{elyt}} \nabla(\eta^A) \tag{3-22}$$

$$i_L^C = \frac{1}{r_{elyt}} \nabla(\eta^C) \tag{3-23}$$

In 1D SOFC model, considering the gas channel main flow direction and the sign convention that is positive for the anodic current and negative for the cathodic current densities [102, 103], substituting the above equations into equation (3-16) results in the modified 1D charge balance equations between the anode and cathode electrode-electrolyte interfaces as follows:

$$C_{dl}^A \frac{\partial(\eta^A)}{\partial t} = -\frac{1}{r_{elyt}} . \frac{\partial^2(\eta^A)}{\partial z^2} + (i_{elyt} - i_F^A) \tag{3-24}$$

$$C_{dl}^C \frac{\partial(\eta^C)}{\partial t} = -\frac{1}{r_{elyt}} . \frac{\partial^2(\eta^C)}{\partial z^2} + (-i_{elyt} - i_F^C) \tag{3-25}$$

Here, i_{elyt} is the electrolyte current density; i_F^A and i_F^C are the Faradic current densities at the anode and cathode sides respectively, which are obtained as follows.

3.2.4 Physically Based Current Voltage Relationship

As it was shown in Figure 3.2, there is a potential gradient inside the solid electrolyte. However, neglecting potential gradient within the electrode thickness that is due to the high conductivity of this phase, the cell voltage can be represented by combining equations (3-13) to (3-15).

$$E_{cell} = \eta^C - \eta^A - (\Phi_{elyt}^A - \Phi_{elyt}^C) \tag{3-26}$$

Additionally, with respect to the Ohm's law and using a linear approximation of the potential profile in the ionic conducting media (electrolyte), the electrolyte current density is defined as:

$$i_{elyt} = -\sigma_{elyt}\left(\frac{\Phi^{C}_{elyt} - \Phi^{A}_{elyt}}{\delta_{elyt}}\right) \tag{3-27}$$

Substituting equation (3-27) into equation (3-26) leads to the following expression for calculating the electrolyte current density through the ionic conducting media.

$$i_{elyt} = \frac{\sigma_{elyt}}{\delta_{elyt}}.(\eta^{C} - E_{cell} - \eta^{A}) \tag{3-28}$$

$$\sigma_{elyt} = 3.34 \times 10^{4} \times \exp(-10300/T^{PEN}) \tag{3-29}$$

In accordance with the fundamental of electrochemistry, the electrolyte current density entering equation (3-27) is equal to the cell current that is measured at the current collectors [48]. Thus the second term on the right hand side of equation (3-24) and (3-25) is equal to the induced current density due to charging and discharging of double layers at transient conditions. In this study, the electrochemical reaction was considered as a single step charge transfer process and the Faradic current densities for the anode and cathode electrodes were calculated from the global Butler-Volmer kinetics [104].

$$i^{A}_{F} = i^{A}_{0}\left[\exp\left(\frac{\alpha^{A}_{a}F}{RT}\eta^{A}_{act}\right) - \exp\left(-\frac{\alpha^{A}_{c}F}{RT}\eta^{A}_{act}\right)\right] \tag{3-30}$$

$$i^{C}_{F} = i^{C}_{0}\left[\exp\left(\frac{\alpha^{C}_{a}F}{RT}\eta^{C}_{act}\right) - \exp\left(-\frac{\alpha^{C}_{c}F}{RT}\eta^{C}_{act}\right)\right] \tag{3-31}$$

Here, α^{A}_{a} and α^{A}_{c} are the charge transfer coefficients of the anode side with the values of 2.0 and 1.0 respectively; similarly, α^{C}_{a} and α^{C}_{c} are the charge transfer coefficient of the cathode side with the values of 1.4 and 0.6 respectively [104]. Additionally, i^{A}_{0} and

i_0^C are the anode and cathode exchange current densities, which can be obtained from the following expressions [96].

$$i_0^A = \gamma^A y_{H_2}^{cat} y_{H_2O}^{cat} \exp(-\frac{E_{act}^A}{RT}) \quad (3\text{-}32)$$

$$i_0^C = \gamma^C (y_{O_2}^{cat})^{0.25} \exp(-\frac{E_{act}^C}{RT}) \quad (3\text{-}33)$$

Here, γ^A and γ^C are the pre-exponential coefficients of the anodic and cathodic exchange current densities; E_{act}^A and E_{act}^C are the activation energy of the anodic and cathodic half layer electrochemical reactions under the equilibrium conditions. To integrate the Butler-Volmer global rate laws into SOFC model, we use the definition of the activation overpotential [48, 99].

$$\eta_{act}^A = \eta^A - \eta_{eq}^A \quad (3\text{-}34)$$

$$\eta_{act}^C = \eta^C - \eta_{eq}^C \quad (3\text{-}35)$$

Here, η_{eq}^A and η_{eq}^C represent the anodic and cathodic equilibrium potential steps. Although the Gibbs free energy change (ΔG^0) for the overall cell reaction ($H_2 + \frac{1}{2}O_2 \rightarrow H_2O$) is available in literature [74], that for either of the half reactions, equations (3-1) and (3-2), is difficult to find [4]. therefore, the method developed by Ho et al. [105] is proposed for calculating the following half-cell equilibrium potential steps.

$$\Delta G^0 = \mu_{H_2O}^0 - \mu_{H_2}^0 - \mu_{O_2}^0/2 \quad (3\text{-}36)$$

$$\eta_{eq}^A = E_{ref} + \frac{1}{2F}(\mu_{H_2O}^0 - \mu_{H_2}^0) + \frac{RT}{2F}\ln(\frac{y_{H_2O}^{cat}}{y_{H_2}^{cat}}) \quad (3\text{-}37)$$

$$\eta_{eq}^C = E_{ref} + \frac{1}{4F}\mu_{O_2}^0 + \frac{RT}{4F}\ln(y_{O_2}^{cat}) \quad (3\text{-}38)$$

Component material balances between the electrodes-electrolyte boundaries and the fuel and air gas channels allow for calculation of the reactant and product concentrations at the electrode-electrolyte interfaces [96].

$$y_i^{cat} = y_i^{f,a} + \frac{\nu_i \delta^{A,C} \left| i_F^{A,C} \right|}{2FD_i^{eff} C^{f,a}} \tag{3-39}$$

Here, D_i^{eff} is the effective diffusion coefficient for which, the contribution of the molecular and Knudsen diffusivities was considered (please refer to Appendix A). Moreover, to distinguish the stoichiometric relationships between reactants and products (ν_i), we define a sign convention that is positive for the products; negative for the reactants and zero for the inert components. Finally, as it was shown above, the exchange current densities, equation (3-32) and equation (3-33), and the half-cell equilibrium potential steps, equations (3-37) and (3-38), are calculated from the species mole fractions at the electrode-electrolyte interfaces. In view of this, there is no need for the explicit evaluation of the concentration overpotentials [70].

3.3. Initial and Boundary Conditions in PFR model

Geometry, operating conditions and model input parameters, used in this model are listed in Tables 3.1 and 3.2 respectively. All variables were given an initial value equal to the equilibrium inlet condition to start the simulation. At the same time, boundary conditions at the inlet of the fuel and air gas channels are specified from the inlet gas conditions. The fuel and air gas temperatures, species molar fractions and inlet velocities are given as the constant values (Dirichlet boundary condition) [6]. However, with respect to the pdepe solver that is available in MATLAB, the solution should satisfy a general form of the boundary condition; therefore, at the outlet boundaries, the change of the gas temperatures, species molar fractions and velocities are set to zero in order to approximate the solution of the right and left hand sides (for more information, please refer to MATLAB documentation relevant to initial boundary value problems for PDEs). It should be noted that, both ends of the PEN structure and interconnects are assumed to be insulated; therefore, at these points the spatial derivative of the PEN and interconnect temperatures are zero (Neuman boundary conditions). The same is true for the electric potential steps at both ends of the PEN structure. Furthermore, convective heat transfer is considered at the interface between the gas channels and the PEN structure, while equations (3-

24) and (3-25) represent charge balance boundary conditions between the electrode and electrolyte interfaces.

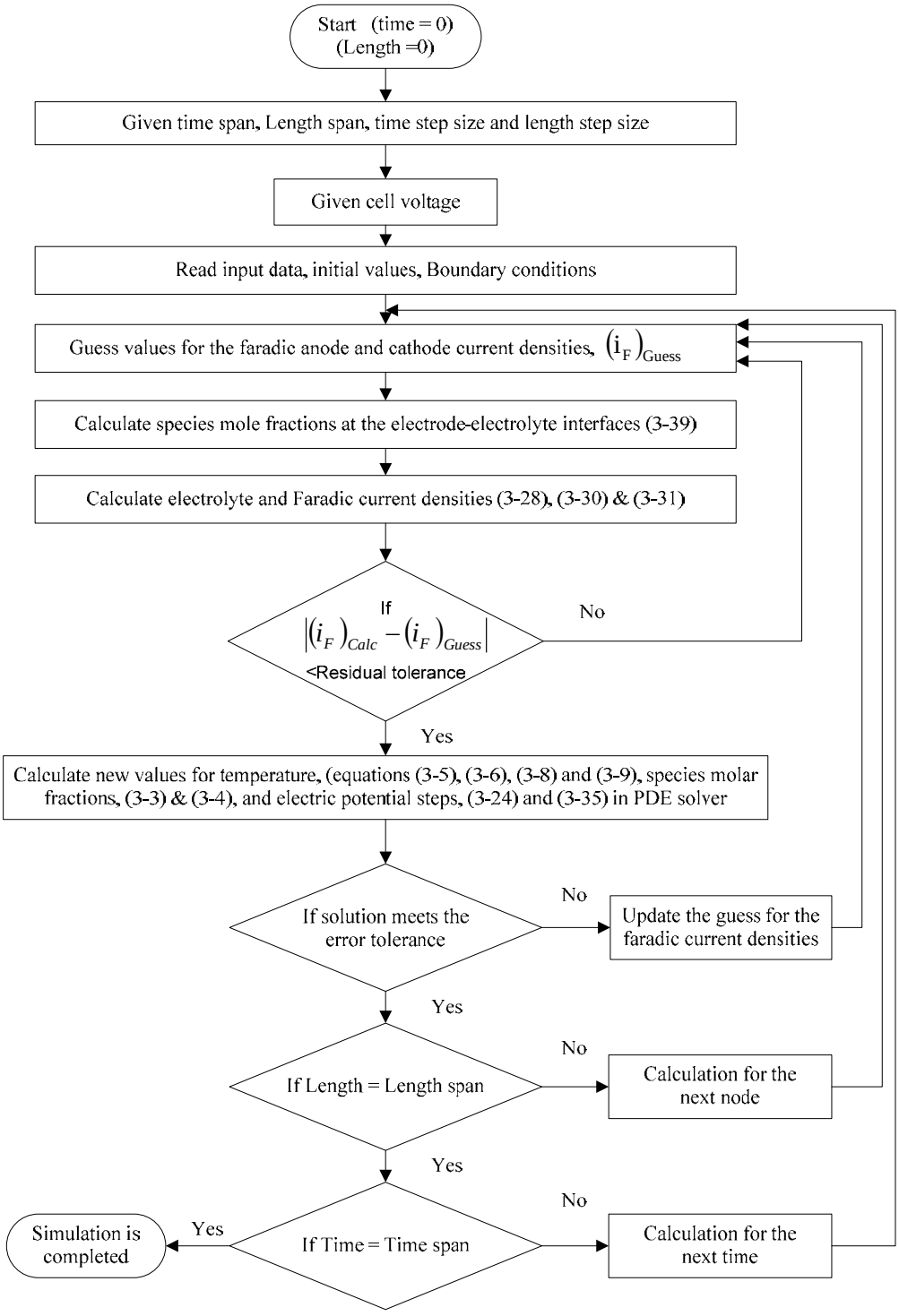

Figure 3.4 – Flow chart of solution technique for PFR model

Figure 3.4 shows the computational procedure for the model and numerical simulation technique, which are implemented as a MATLAB code. All governing equations were solved simultaneously with the in-built PDE solver. The PDE solver converts the partial differential equations to ODEs using a second-order spatial discretization based on the fixed set of the specified nodes. The discretization method is described in [106]. The time integration is done with ODE15s that is another in-built solver specified for the ordinary differential equations. At each step, the ODE solver estimates the local error of the solution. This error must be less than or equal to the acceptable error, which is a function of the specified values of the relative and absolute tolerances.

Table 3.1 – Geometry and operating conditions for the PFR model[104, 107]

Parameter	**Value**
Fuel/air channel height H^f / H^a, m	1.0×10^{-3}
Channel length L, m	19×10^{-3}
Anode thickness δ^A, μm	700
Cathode thickness δ^C, μm	50
Electrolyte thickness δ_{elyt}, μm	10
Interconnect thickness δ^I, μm	500
Fuel inlet velocity $\vec{u}^f$, m/s	1.25
Air inlet velocity $\vec{u}^a$, m/s	1.87
Inlet H_2 molar fraction in fuel y_{H_2-in}, %	73 ~ 97
Inlet O_2 molar fraction in air y_{O_2-in}, %	0.21
Pressure, atm.	1
Inlet fuel and air Temperature T_{in}, K	1023

3.4. Simulation Results and Discussion

The above section presents a complete set of one dimensional mathematical relation governing the steady state and dynamic behaviour of SOFC. Using these equations, a MATLAB code was developed to simulate the SOFC operation. In this

section, we first check the validity of this model; after that, we evaluated the steady state simulation results and finally the dynamic responses to a voltage step change and to a frequently-time varying sinusoidal voltage were analysed and compared.

Table 3.2 – Input parameters for PFR model[76, 96, 104]

Parameter	**Value**
Convective heat transfer coefficient ($\hbar^{f,a}$)	25
H2 molar heat capacity ($c_{p,\,H_2}$)	30
H2O molar heat capacity ($c_{p,\,H_2O}$)	44
O2 molar heat capacity ($c_{p,\,O_2}$)	36
N2 molar heat capacity ($c_{p,\,N_2}$)	34
PEN emissivity, (ξ^{PEN})	0.8
Thermal conductivity of the PEN structure (k^{PEN})	2
PEN heat capacity (c_p^{PEN}, J.kg^{-1}K^{-1})	500
PEN density (ρ^{PEN})	5900
Interconnect emissivity (ξ^{I})	0.1
Thermal conductivity of the interconnect (k^{I})	25
Interconnect heat capacity (c_p^{I}, J.kg^{-1}K^{-1})	500
Interconnect density (ρ^{I})	8000
Charge transfer coefficient, (α_A^A)	2.0
Charge transfer coefficient, (α_C^A)	1.0
Charge transfer coefficient, (α_A^C)	1.4
Charge transfer coefficient, (α_C^C)	0.6
Anode activation energy (E_{act}^A)	120000
Cathode activation energy (E_{act}^C)	110000

3.4.1. Evaluation of the Results from PFR Model

Figure 3.5 shows the comparison of the simulation results corresponding to each fuel composition at different voltage with the experimental data reported by Keegan et al. [107].

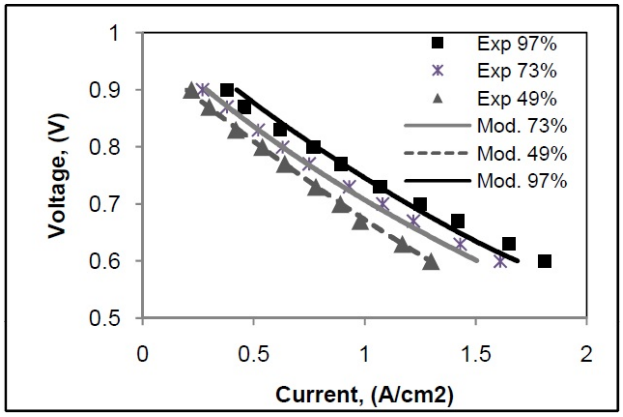

Figure 3.5 – PFR model - Comparison of the predicted V-I curve from PFR model with experimental data[107]

In order to carry out the comparison between the experiment and the simulation results, we inserted the same operating conditions into the proposed model. However, geometry and some physical and electrochemical parameters were not addressed properly in the experimental work and then in case of the geometrical parameters, they were collected from the work of Chaisantikulwat et al. [104] who compared their simulation results with the same experimental data. With respect to the effect of the geometry that is not included in 1D model, some discrepancies between the simulation and experimental results were expected. Additionally, under the same operating condition, as the hydrogen concentration increased, more current can be taken out from the cell; therefore, the influence of geometry and uncertainty for the model input parameters become more significant and the discrepancy between the predicted results and experimental data increased. However, it can be clearly observed that the simulation results had captured the overall trend of the experimental data. On average, the simulation results from the model in the range of 0.9 to 0.7 volt agreed best with the experimental values.

3.4.2. Steady State Simulation Results from PFR Model

The steady state simulation results along the cell length at 0.8V and 1023K are discussed here. Figure 3.6 (a) illustrates the distribution of Faradic and electrolyte current densities at the electrode-electrolyte interfaces. Consistent with the PEN temperature and species concentration profiles, the maximum current density is placed at the air outlet and as it was expected, under the steady state condition, Faradic current is equal to the electrolyte current density and double layer induced current is zero. The non-uniform distributions of the current densities reveal the nonlinear inter relations among all parametric changes. Figure 3.6 (b) indicates the temperature distribution in the PEN structure, interconnect and gas channels. As it was shown, the PEN temperature is the highest which increased a bit along the air flow direction. This is due to the heat source term from the electrochemical reaction that is placed in this layer and cooling effect of the air flow which is most effective near the air inlet. Depending on the heat transfer coefficients, temperature of interconnect is more uniform than the PEN structure. Consistent with the counter flow direction, in fuel and air gas channels, the temperature increased toward the outlets. Furthermore, under the coupling effects of temperature and current density, the anode overpotentials decreased along the cell length. However, as it was shown in Figure 3.6 (c) and (d), depending on the model input parameters; cathode activation overpotential is higher than the anode side. Figure 3.6 (e) to (g), illustrate the concentration distribution of the reactants. Hydrogen was consumed through the fuel direction while the concentration of water increased due to the flux from the anode-electrolyte interface to the gas channel. Similarly, the oxygen concentration decreased through the air flow direction that is due to the electrochemical reaction at the cathode-electrolyte interface.

3.4.3. Dynamic Results from PFR Model -Voltage Step Change

In this section, the transient behaviour of the cell was analysed. In the first case, as it was shown in Figure 3.7, we investigated the cell transient performance induced by the step change of the cell voltage from 0.8 to 0.75 volt at 50^{th} second with the rest of the boundary condition kept constant.

Dynamic response of the current densities to the voltage step decrease exhibit initial sudden jump that is due to the instantaneous electrochemical reaction, taking place at the electrode-electrolyte interfaces. After the first initial response, a slow transient period that is mainly influenced by the PEN temperature was observed. However, the transient response of the current density is very complex and related to all parametric changes, which are associated with the entire fuel cell activity [108]. As it was explained above, the electrolyte current density is equal to the one that is measured at the current collectors. On the other hand, the electrolyte current is equal to the sum of the Faradic current, due to charge transfer electrochemistry, and the current due to charging and discharging of the electrical double layers upon transient conditions. Thus for a very short time, the initial response of the electrolyte current is significantly higher than the Faradic current density due to the sudden intensive discharge of the capacitance double layer. As it was shown, the cell response to the charging or discharging process is fast; therefore, in most practical purposes, this transient behaviour for the voltage step change is neglected [30]. In addition to the above, at the anode side and immediately after the first initial jump, the Faradic current density decreased in a short period that was observed as the undershot of its dynamic response. This is due to the larger mass transfer time scale through the electrode porous media. As it was shown in Figure 3.7 (d), the magnitude of the change for the cathode activation overpotential is higher which reveals the higher resistance of the electrochemical reaction at the cathode side. Thus the response of the Faradic current density was affected and consequently at the cathode side, the mass transfer limitation is not spotted at the anode side. Increasing the current density leads to more heat release from the electrochemical reaction which results in a gradual temperature rise. The response of the activation overpotentials in Figure 3.7 (c) and (d) are consistent with temperature and current density. After the first sudden increase, under the effects of the PEN temperature, they show a moderate decrease toward the new steady state condition. Furthermore, at the instant of this momentary increase of the current density, a sudden change in the mass source term of the component balance equation occurs and the sudden change of the reactant's concentration were observed. Followed by a slow change that is mainly due to the combined effects of the temperature and the slow dynamics of the current density was detected. The same trend of the SOFC transient responses to a voltage step change were also reported by other authors [67].

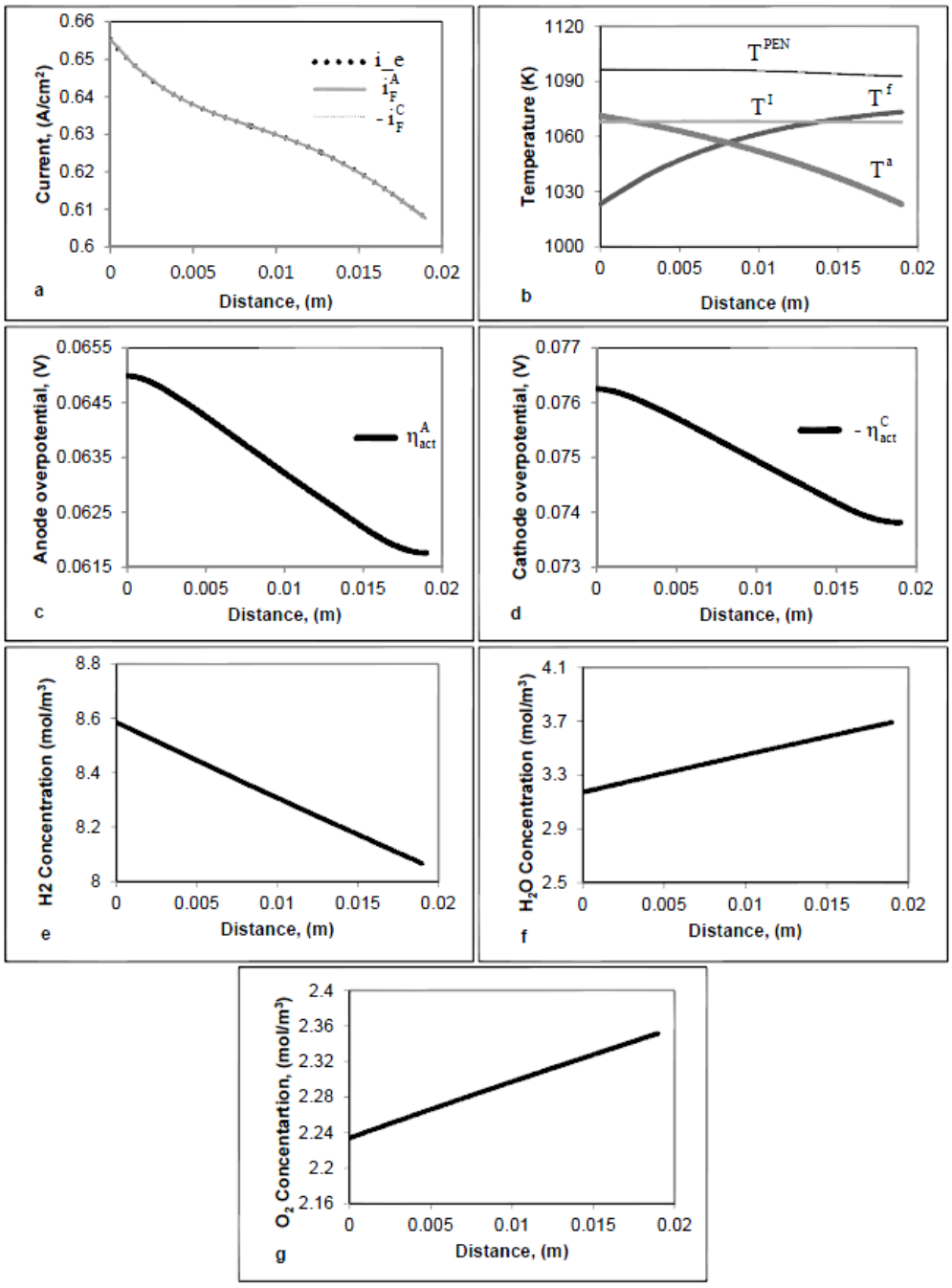

Figure 3.6 - Steady state simulation results along the cell length for 73% hydrogen fuel at 0.8 volt

3.4.4. Dynamic Results from PFR Model - Sinusoidal Voltage Change

Figures 3.8 and 3.9 show the sinusoidal voltage change as presented in equation (3-40) and the SOFC dynamic response to this time dependent alternating sinusoidal voltage respectively.

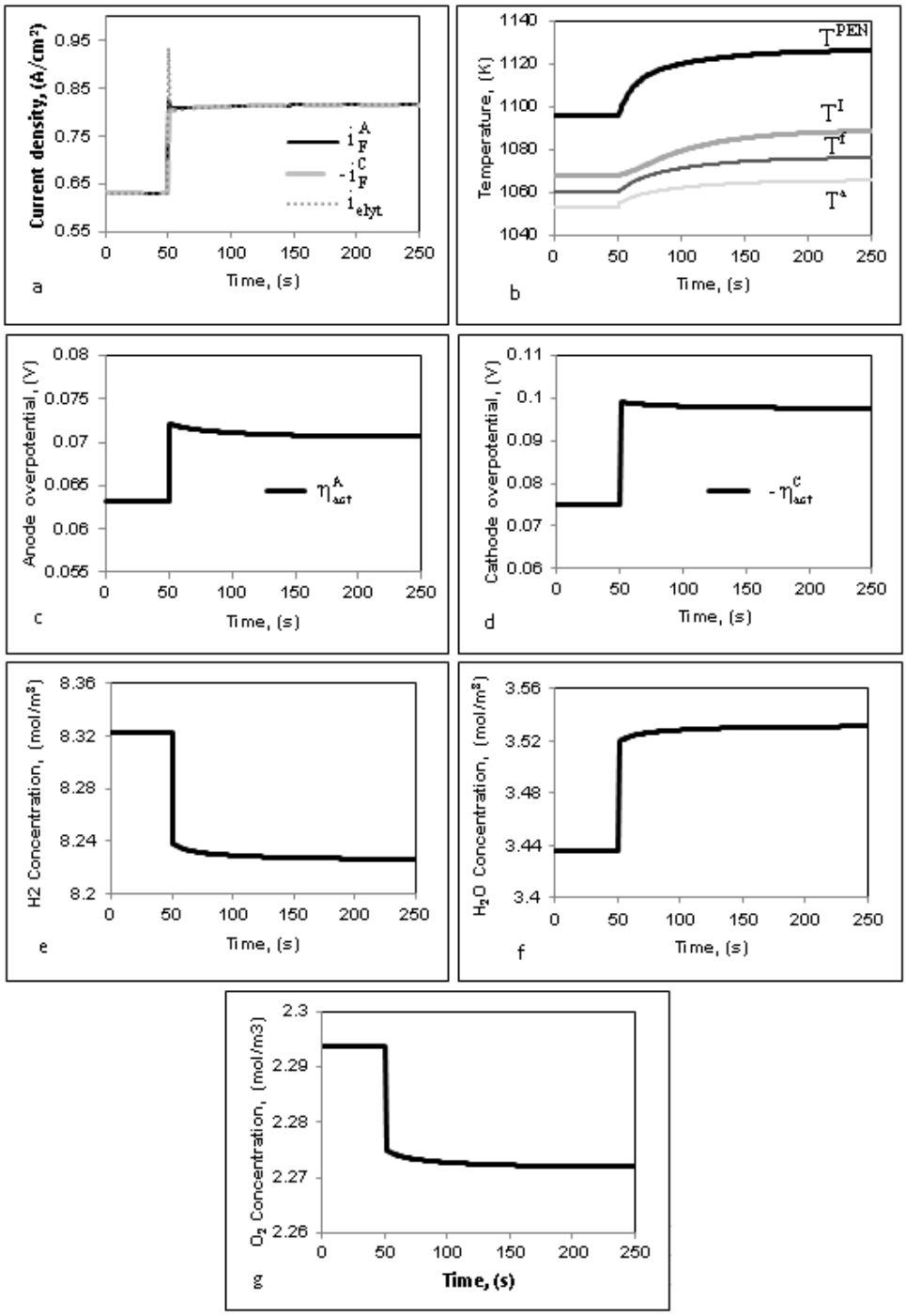

Figure 3.7 - Dynamic response of the cell to a voltage step change from 0.8 to 0.75 volt at the half length of the cell (z=L/2)

$$E_{cell} = E_{bias} + E_{amp}.\sin(\omega t) \tag{3-40}$$

$$\varpi = 2\pi f \tag{3-41}$$

Here E_{bias} is the bias voltage equal to 0.8 volt; E_{amp} is the amplitude voltage and ω is the angular frequency in radians. For SOFC measurements, a frequency range of 0.01 Hz to 1.0 MHz and amplitude of 10 to 50mV are normally chosen[45]. However, the effects of double layer induced current occurred at high frequency range around 10^2 kHz [49]. In view of this, a typical sinusoidal voltage with the frequency of 10^2 KHz and amplitude of 0.05 volt was used as the sinusoidal input voltage.

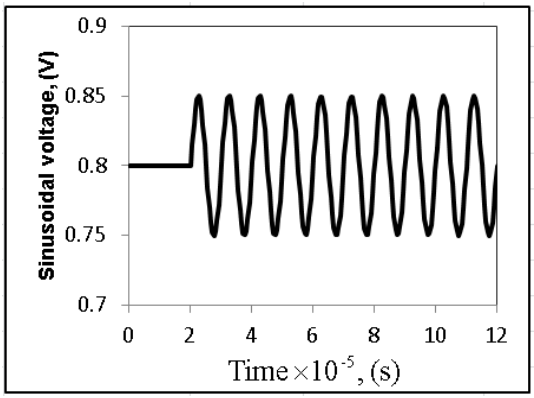

Figure 3.8 - Sinusoidal voltage change with amplitude of 0.05 volt and frequency of 10^2 KHz

As shown in Figure 3.9, in comparison with the cell response to a voltage step change, reactants' concentration and temperature are almost constant that is due to their characteristic time constants, which are of the order of seconds and minutes respectively [30] and hence, they are not sensitive to the high frequency voltage change. Furthermore, due to the moderate sinusoidal voltage change, the first initial overshoot of the electrolyte current density was not detected. However, double layer induced current adds up with the Faradic current and despite the case for a voltage step change, a continual difference between the Faradic and electrolyte current densities was observed. Since the Faradic current is directly related to the activation overpotential [49], its dynamic response to a continual varying sinusoidal voltage is a bit different at the anode and cathode side. However, from equations (3-17) and (3-18), it is evident that this difference could be extended depending on the value of double layer capacitance. Figure 3.10, compares dynamic responses of the current densities and overpotentials at two different capacities. As shown in that Figure, for the lower capacity ($C_{dl} = 0.8$), double layer induced current density is

negligible and the Faradic and electrolyte current densities are almost identical. However, for the higher value of double layer capacity ($C_{dl} = 1.63$), the differences between Faradic and electrolyte current densities increased and Faradic currents were a bit phase shifted with respect to the electrolyte current density. This is mainly due to the intensity of the charging and discharging processes and the resistance of the electrochemical reaction to the periodic voltage changes. At the cathode side, the higher resistance of the half-cell electrochemical reaction causes less change for the Faradic current and consequently, the activation overpotential become less sensitive to a sinusoidal variation in voltage.

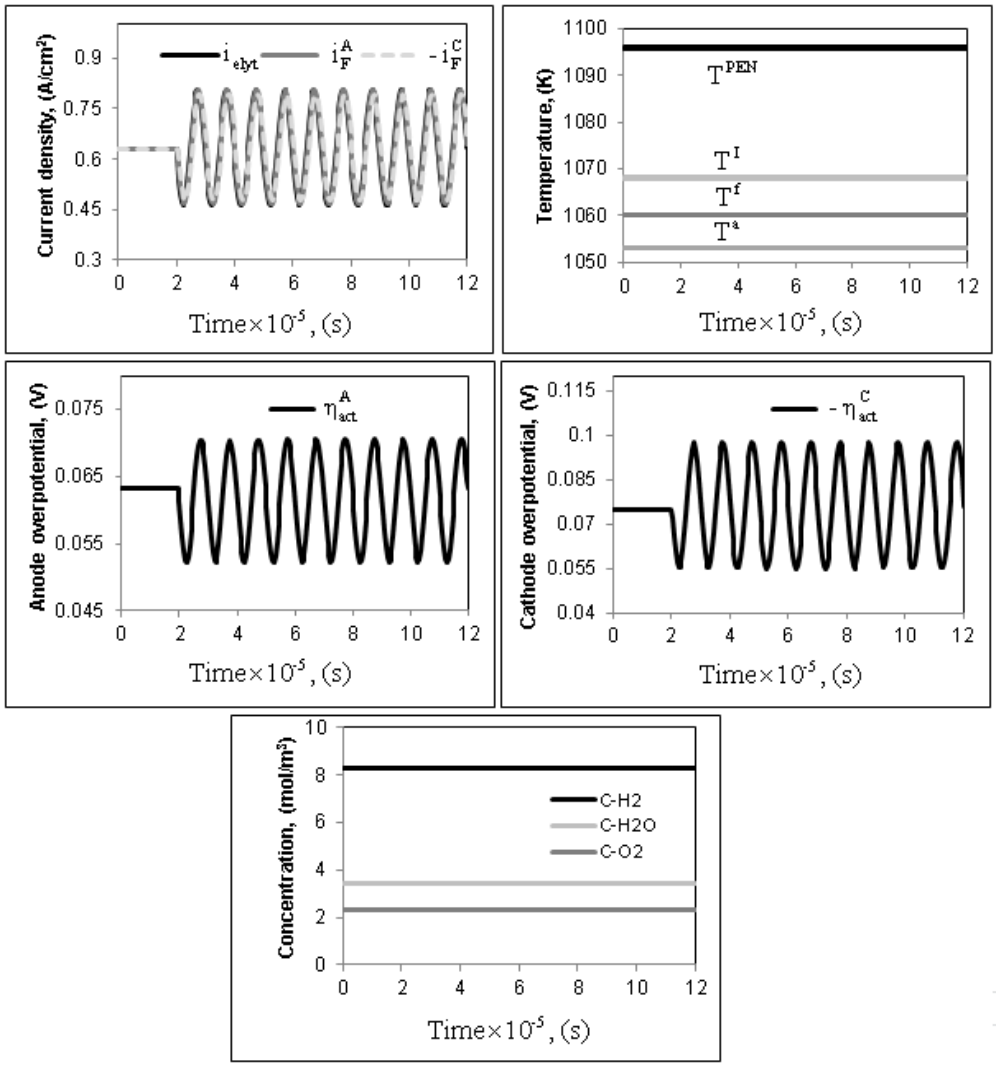

Figure 3.9 - Dynamic response of the cell to a sinusoidal voltage change with capacity of 1.29 Fm-2 at the half length of the cell (z=L/2)

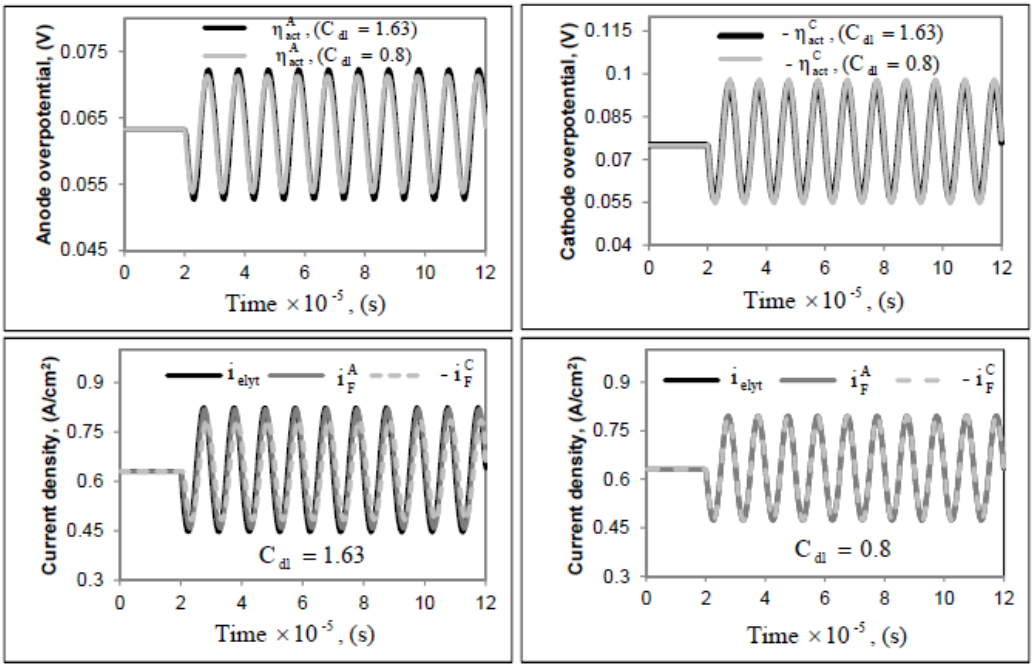

Figure 3.10 - Effects of double layer capacity on dynamic responses of the current densities and overpotentials at the half length of the cell (z=L/2)

3.5. Summary

In this work, physically based dynamic plug flow reactor model accounting for mass, heat and charge transports was developed to analyse the steady state and dynamic performances of a planar SOFC. This model can get the capacitor effect of double layer on charge transfer process. Furthermore, modified expression for the charge transfer between the electron and ion conducting phases facilitates physically based characteristics of the Faradic and electrolyte current densities. The simulation results revealed the nonlinear interactions among temperature, current densities, species concentrations and overpotentials. As expected, under the steady state condition, no charging or discharging process occurred and the Faradic and electrolyte current densities are identical. However, transient response of the current density is very complex and depends on all parametric changes which are associated with the entire fuel cell processes. In response to a voltage step change, apart from the first initial jump of the electrolyte current density, double layer charging or discharging process has insignificant effect on transient behaviour. Moreover, depending on the reaction and diffusional resistances, the Faradic current density can be influenced further. However, the slow dynamics of the cell

to a voltage step change is mainly governed by temperature. In comparison with the voltage step change, when SOFC is subjected to a time varying sinusoidal voltage, temperature and reactants' concentration are not sensitive to the high frequency and they remain almost constant. This is a good evidence which allows us to consider isothermal condition in our future research on fuel cell impedance analysis under the effects of the high frequent sinusoidal voltage change. Additionally, depending on the double layer capacity and frequent charging and discharging process, a continual difference between the Faradic and electrolyte current densities was observed. As a result, under the effect of sinusoidal voltage change, dynamic response of the cell is mainly controlled by the electrochemical reaction and charging or discharging of double layer capacity. However, there is a direct relation between the Faradic current densities and overpotentials. Thus for the cathode-electrolyte interface with higher resistance of the half-cell electrochemical reaction, the activation overpotential and consequently the Faradic current become less sensitive to the sinusoidal variation of voltage. Considering the importance of the periodic responses of the cell to a time varying voltage for the SOFC impedance studies, this physically based model is applicable for numerical impedance analysis that could be the subject of the future studies. Therefore, it can provide practical application for analysing the kinetic behaviour and material properties. In particular, using this model for the electrode microstructure grading, we can effectively improve the SOFC performance due to the subsequent effects of the electrode properties on double layer capacities and the resistance of the porous electrodes to the gas diffusion process.

Chapter 4

New dynamic Tanks in Series Reactor Model of a Planar SOFC from a Network of Several Continuous Stirred Tank Reactors

4.1. Introduction

Models of different complexity are required in the iterative process of designing a solid oxide fuel cell (SOFC). Models having less complexity and computational dexterity that falls between the most simplified lumped and multi-dimensional models are the ideal ones for the SOFC system analysis, dynamic simulations and control purposes. In view of that, the aim of this chapter is to develop a new tank in series reactor (TSR) model of a planar SOFC from a network of several continuous stirred tank reactors (CSTR). The model presented in this work can serve as an early step in the iteration by means of accelerating two dimensional simulation of the planar SOFC under potentiostatic operating mode to get the effects of different co, counter and cross flow direction on the fuel and air utilization, distribution of current, temperature and species concentration and finally dynamic responses to the voltage step change. This model includes species mass balances to the gas channels and diffusion layers, energy balances for the fuel and air channels and also for the PEN structures. Moreover, charge balance equations were defined as the boundary condition at the electrode-electrolyte interfaces and facilitate analysing charge transfer process and calculation of the activation overpotential.

4.2. TSR Model Development

Several CSTR fuel cells can be connected as the reactor network to approximate more complicated flow fields. Figure 4.1 illustrates the application of new tank in series reactor model for different co-, counter- and cross flow directions of fuel and

air in a planar solid oxide fuel cell in which, the main components of an SOFC consist of the fuel and air gas channels and the PEN structure.

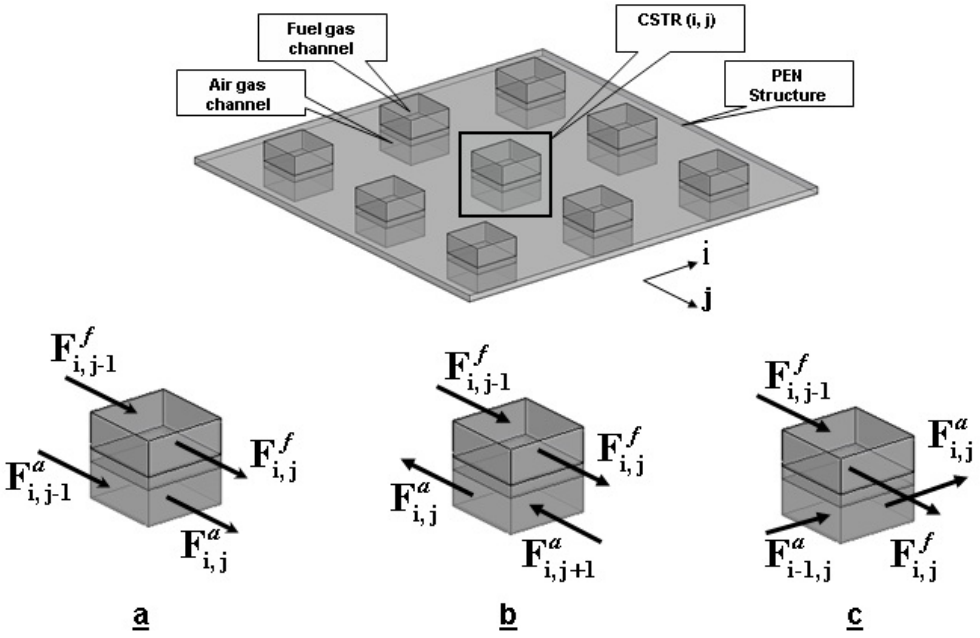

Figure 4.1 - Schematic view of different fuel and air flow direction for one of the compartments, CSTR ($_{i,\,j}$), in TSR model of a planar SOFC;
a) co-flow; b) counter-flow; c) cross-flow[108]

This model is based on the following assumptions:

- Each fuel and air compartment is treated as a continuous stirred tank reactor;
- Electrochemical reactions occur at the electrode-electrolyte interfaces;
- Fuel cell operates with hydrogen/air under the potentiostatic operating mode and constant total pressure;
- Ohmic drops in current collectors and electric connections are negligible;
- The gas mixtures in fuel and air compartments are treated according to the ideal gas law;

- Due to the large aspect ratio, the radiation heat transfer is not considered[7, 109, 110].

Since in this work, the modelling objective is to develop a new tank in series reactor (TSR) model of a planar SOFC from a network of several continuous stirred tank reactors (CSTR), two types of models are presented in the following sections. First, a CSTR model of the planar SOFC is derived which assumed uniform current, temperature and species concentration throughout different parts of that single CSTR slot including both the fuel and air gas channels and the PEN structure. However, in line with the real physics, this may not be true for a complete cell and distribution of different parameters should be considered. Thus, the second type of model is presented as a new tank in series reactor model that is based on several CSTR compartments, which can be connected as a reactor network to estimate the distribution of current, temperature and species concentration throughout the complete cell and finally dynamic responses to a voltage step change under different co-, counter- and cross flow directions of the fuel and air were obtained.

4.2.1. CSTR Model of the Planar SOFC

Figure 4.2 shows the schematic view of a planar SOFC as a single continuous stirred tank reactor.

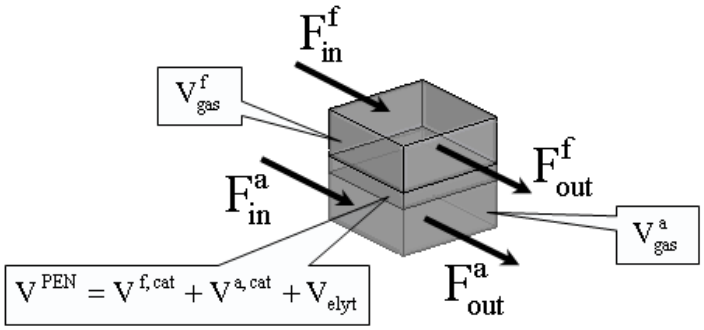

Figure 4.2 - Planar SOFC as a continuous stirred tank reactor (CSTR)

Various phenomena occur in the fuel cell such as mass and heat transfers, charge transfer, and the electrochemical reactions. Based on the above assumptions, component balance equations for the fuel and air gas channels are written as follows:

$$C^{f} V_{gas}^{f} \frac{dy_{H_2}^{f}}{S.dt} = y_{H_2\text{-in}}^{f} \frac{F_{in}^{f}}{S} - y_{H_2}^{f} \frac{F_{out}^{f}}{S} - \frac{C^{f} D_{H_2}^{eff}}{\delta^{A}} (y_{H_2}^{f} - y_{H_2}^{cat}) \tag{4-1}$$

$$C^{f} V_{gas}^{f} \frac{dy_{H_2O}^{f}}{S.dt} = y_{H_2O\text{-in}}^{f} \frac{F_{in}^{f}}{S} - y_{H_2O}^{f} \frac{F_{out}^{f}}{S} - \frac{C^{f} D_{H_2O}^{eff}}{\delta^{A}} (y_{H_2O}^{f} - y_{H_2O}^{cat}) \tag{4-2}$$

$$C^{a} V_{gas}^{a} \frac{dy_{O_2}^{a}}{S.dt} = y_{O_2\text{-in}}^{a} \frac{F_{in}^{a}}{S} - y_{O_2}^{a} \frac{F_{out}^{a}}{S} - \frac{C^{a} D_{O_2}^{eff}}{\delta^{C}} (y_{O_2}^{a} - y_{cat}^{O_2}) \tag{4-3}$$

In fuel cells, the reacting species are diffusing from the gas channels through the porous electrode to the electrode-electrolyte interface; then the component balance equations for catalyst layers are written as follows:

$$C^{f} V_{cat}^{f} \frac{dy_{H_2}^{cat}}{S.dt} = \frac{C^{f} D_{H_2}^{eff}}{\delta^{A}} (y_{H_2}^{f} - y_{H_2}^{cat}) - R_{r,H_2} \tag{4-4}$$

$$C^{f} V_{cat}^{f} \frac{dy_{H_2O}^{cat}}{S.dt} = \frac{C^{f} D_{H_2O}^{eff}}{\delta^{A}} (y_{H_2O}^{f} - y_{H_2O}^{cat}) + R_{r,H_2O} \tag{4-5}$$

$$C^{a} V_{cat}^{a} \frac{dy_{O_2}^{cat}}{S.dt} = \frac{C^{a} D_{O_2}^{eff}}{\delta^{C}} (y_{O_2}^{a} - y_{O_2}^{cat}) - R_{r,O_2} \tag{4-6}$$

The energy balances for the fuel and air channels and the PEN structure (solid volume) are written as follows:

$$V_{gas}^{f} C^{f} c_{p}^{f} \frac{dT^{f}}{S.dt} = (\frac{F_{in}^{f}}{S} h_{in}^{f} - \frac{F_{out}^{f}}{S} h_{out}^{f}) + R_{h}^{f} \tag{4-7}$$

$$V_{gas}^{a} C^{a} c_{p}^{a} \frac{dT^{a}}{S.dt} = (\frac{F_{in}^{a}}{S} h_{in}^{a} - \frac{F_{out}^{a}}{S} h_{out}^{a}) + R_{h}^{a} \tag{4-8}$$

$$V^{PEN} \rho c_{p}^{PEN} \frac{dT^{PEN}}{S.dt} = R_{h}^{PEN} \tag{4-9}$$

The electrode-electrolyte interface is analogous to that of a capacitor. From the previous chapter, the next charge balance equations are valid for the anode and cathode-electrolyte interfaces.

$$C_{dL}^{A}\frac{d\eta^{A}}{dt}=(i_{elyt}-i_{F}^{A}) \tag{4-10}$$

$$C_{dL}^{C}\frac{d\eta^{C}}{dt}=(-i_{elyt}-i_{F}^{C}) \tag{4-11}$$

Munder et al. [102] used the above charge balance equations for solid oxide fuel cell under galvanostatic operating mode. As shown in the previous chapter and also the work of Danilov and Tade[61], in the case of potentiostatic operating mode, the source term on the right side of equations (4-10) and (4-11) is the difference of currents in electrode and electrolyte media in compliance with the electromagnetic theory.

4.2.2. TSR Model for the Co-Current Flow Direction

Figure 4.1a illustrates the application of the tank in series reactor model (TSR) for the co-current flow of fuel and air in a planar SOFC. For the TSR model of fuel cells with co-current flow direction, the mass balance equations for the components in the fuel and air gas channels are written as follows:

$$C^{f}V_{gas-i,j}^{f}\frac{dy_{H_2\text{-}i,j}^{f}}{S_{i,j}dt}=y_{H_2\text{-}i,j-1}^{f}\frac{F_{i,j\text{-}1}^{f}}{S_{i,j}}-y_{H_2\text{-}i,j}^{f}\frac{F_{i,j}^{f}}{S_{i,j}}-\frac{C^{f}D_{H_2}^{eff}}{\delta^{A}}(y_{H_2\text{-}i,j}^{f}-y_{H_2\text{-}i,j}^{cat}) \tag{4-12}$$

$$C^{f}V_{gas-i,j}^{f}\frac{dy_{H_2O\text{-}i,j}^{f}}{S_{i,j}.dt}=y_{H_2O\text{-}i,j-1}^{f}\frac{F_{i,j\text{-}1}^{f}}{S_{i,j}}-y_{H_2O\text{-}i,j}^{f}\frac{F_{i,j}^{f}}{S_{i,j}}-\frac{C^{f}D_{H_2O}^{eff}}{\delta^{A}}(y_{H_2O\text{-}i,j}^{f}-y_{H_2O\text{-}i,j}^{cat}) \tag{4-13}$$

$$C^{a}V_{gas-i,j}^{a}\frac{dy_{O_2\text{-}i,j}^{a}}{S_{i,j}.dt}=y_{O_2\text{-}i,j-1}^{a}\frac{F_{i,j\text{-}1}^{a}}{S_{i,j}}-y_{O_2\text{-}i,j}^{a}\frac{F_{i,j}^{a}}{S_{i,j}}-\frac{C^{a}D_{O_2}^{eff}}{\delta^{C}}(y_{O_2\text{-}i,j}^{a}-y_{O_2\text{-}i,j}^{cat}) \tag{4-14}$$

In these equations, the first and second terms on the right hand side represent the convective mass transfer rates associated with the fuel and air flow streams. The last term on the right side of the above equations presents the species mass

diffusion between the gas channels and catalyst layer. Additionally, $V^{f}_{gas\,-i,\,j}$ and $V^{a}_{gas\,-i,\,j}$ are the volume of each fuel and air gas compartment (tank i, j), which are calculated as follows.

$$V^{f}_{gas\,-i,\,j} = V^{f}_{gas}/(n_{i}\,n_{j}) \tag{4-15}$$

$$V^{a}_{gas\,-i,\,j} = V^{a}_{gas}/(n_{i}\,n_{j}) \tag{4-16}$$

Here V^{f}_{gas} and V^{a}_{gas} are the total volume of the fuel and air gas channels, respectively, and n is the number of tanks in i and j directions. In the co-current flow scheme, the fuel and air exit streams from tank $i, j-1$ are the inlet streams into tank i, j. Thus, the exiting flow rates from the gas channels of each tank ($F^{f}_{i,\,j}$ and $F^{a}_{i,\,j}$) depend on the flow rates of the previous tank as well ($F^{f}_{i,\,j-1}$ and $F^{a}_{i,\,j-1}$).

$$F^{f}_{i,j} = F^{f}_{i,j-1} - \frac{C^{f} D^{eff}_{H_2} S_{i,j}}{\delta^{A}}(y^{f}_{H_2\text{-}i,j} - y^{cat}_{H_2\text{-}i,j}) - \frac{C^{f} D^{eff}_{H_2O} S_{i,j}}{\delta^{A}}(y^{f}_{H_2O\text{-}i,j} - y^{cat}_{H_2O\text{-}i,j}) \tag{4-17}$$

$$F^{a}_{i,j} = F^{a}_{i,j-1} - \frac{C^{a} D^{eff}_{O_2} S_{i,j}}{\delta^{C}}(y^{a}_{O_2\text{-}i,j} - y^{cat}_{O_2\text{-}i,j}) \tag{4-18}$$

In these equations C is the gas molar density; $S_{i,j}$ is the electrode area of each tank, and $y_{i,j}$ is the species molar fraction in each gas compartment. The effective diffusivity and species molar fraction at the catalyst layer of each compartment are represented as D^{eff} and, $y^{cat}_{i,j}$ respectively.

Component balance equations for species in anode and cathode catalyst layers are written as follows:

$$C^{f} V^{f}_{cat-i,j} \frac{dy^{cat}_{H_2,i,j}}{S_{i,j}.dt} = \frac{C^{f} D^{eff}_{H_2}}{\delta^{A}}(y^{f}_{H_2\text{-}ij} - y^{cat}_{H_2\text{-}i,j}) + R_{r,H_2\text{-}i,j} \tag{4-19}$$

$$C^{f} V^{f}_{cat-i,j} \frac{dy^{cat}_{H_2O\text{-}i,j}}{S_{i,j}.dt} = \frac{C^{f} D^{eff}_{H_2O}}{\delta^{A}}(y^{f}_{H_2O\text{-}ij} - y^{cat}_{H_2O\text{-}i,j}) + R_{r,H_2O\text{-}i,j} \tag{4-20}$$

$$C^{a}V^{a}_{cat-i,j}\frac{dy^{cat}_{O_2\text{-}i,j}}{S_{i,j}.dt}=\frac{C^{a}D^{eff}_{O_2}}{\delta^{C}}(y^{a}_{O_2\text{-}ij}-y^{cat}_{O_2\text{-}i,j})+R_{r,O_2\text{-}i,j} \tag{4-21}$$

Here the variable $R_{r\text{-}i,j}$ represents the mass flux in each compartment via electrochemical reaction. Faraday's law relates the flux of reactants to the electric current arising from the electrochemical reaction as will be shown in equations (4-62) to (4-64). Again, $V^{f}_{cat\text{-}i,j}$ and $V^{a}_{cat\text{-}i,j}$ are the volumes of the catalyst layer of each fuel and air compartment (tank $_{i,j}$), which are calculated as follows:

$$V^{f}_{cat-i,j}=V^{f}_{cat}/(n_i n_j) \tag{4-22}$$

$$V^{a}_{cat-i,j}=V^{a}_{cat}/(n_i n_j) \tag{4-23}$$

The energy balances for the fuel and air gas channels and the PEN structure for each compartment (tank$_{i,j}$) are written as follows:

$$C^{f}V^{f}_{gas-i,j}c^{f}_{p}\frac{dT^{f}_{i,j}}{S_{i,j}.dt}=(\frac{F^{f}_{i,j-1}}{S_{i,j}}h^{f}_{i,j-1}-\frac{F^{f}_{i,j}}{S_{i,j}}h^{f}_{i,j})+R^{f}_{h\text{-}i,j} \tag{4-24}$$

$$C^{a}V^{a}_{gas-i,j}c^{a}_{p}\frac{dT^{a}_{i,j}}{S_{i,j}.dt}=(\frac{F^{a}_{i,j-1}}{S_{i,j}}h^{a}_{i,j-1}-\frac{F^{a}_{i,j}}{S_{i,j}}h^{a}_{i,j})+R^{a}_{h\text{-}i,j} \tag{4-25}$$

$$V^{PEN}_{i,j}\rho c^{PEN}_{p}\frac{dT^{PEN}_{i,j}}{S_{i,j}.dt}=R^{PEN}_{h\text{-}i,j} \tag{4-26}$$

The governing equations for the fuel and air temperature are formulated with the inlet and outlet energy transfer fluxes from the gas flow streams (the first and second terms on the right hand sides of equations 4-24 and 4-25) and the source terms $R^{f}_{h\text{-}i,j}$ and $R^{a}_{h\text{-}i,j}$, which represent the amount of heat fluxes given from the PEN structure. The variable $R^{PEN}_{h\text{-}i,j}$ represents a heat flux for the amount of heat accumulation in the PEN structure (solid volume). The energy source terms can be calculated from equation (4-65) to (4-67).

The charge balance equations for the anode-electrolyte and the cathode-electrolyte interfaces are given as follows:

$$C_{dL}^{A}\frac{d\eta_{i,j}^{A}}{dt}=(i_{elyt\text{-}i,j}-i_{F\text{-}i,j}^{A}) \tag{4-27}$$

$$C_{dL}^{C}\frac{d\eta_{i,j}^{C}}{dt}=(-i_{elyt\text{-}i,j}-i_{F\text{-}i,j}^{C}) \tag{4-28}$$

For the tanks with $j = 1$, which represents the inlet sections of the fuel and air gas channels, we obtain the component balances as follows:

$$C^{f}V_{gas-i,1}^{f}\frac{dy_{H_2\text{-}i,1}^{f}}{S_{i,1}.dt}=y_{H_2\text{-}in}^{f}\frac{F_{i,in}^{f}}{S_{i,1}}-y_{H_2\text{-}i,1}^{f}\frac{F_{i,1}^{f}}{S_{i,1}}-\frac{C^{f}D_{H_2}^{eff}}{\delta^{A}}(y_{H_2\text{-}i,1}^{f}-y_{H_2\text{-}i,1}^{cat}) \tag{4-29}$$

$$C^{f}V_{gas-i,1}^{f}\frac{dy_{H_2O\text{-}i,1}^{f}}{S_{i,in}.dt}=y_{H_2O\text{-}in}^{f}\frac{F_{i,in}^{f}}{S_{i,1}}-y_{H_2O\text{-}i,1}^{f}\frac{F_{i,1}^{f}}{S_{i,1}}-\frac{C^{f}D_{H_2O}^{eff}}{\delta^{A}}(y_{H_2O\text{-}i,1}^{f}-y_{H_2O\text{-}i,1}^{cat}) \tag{4-30}$$

$$C^{a}V_{gas-i,1}^{a}\frac{dy_{O_2\text{-}i,1}^{a}}{S_{i,1}.dt}=y_{O_2\text{-}in}^{a}\frac{F_{i,in}^{a}}{S_{i,1}}-y_{O_2\text{-}i,1}^{a}\frac{F_{i,1}^{a}}{S_{i,1}}-\frac{C^{a}D_{O_2}^{eff}}{\delta^{C}}(y_{O_2\text{-}i,1}^{a}-y_{O_2\text{-}i,1}^{cat}) \tag{4-31}$$

$$F_{i,1}^{f}=F_{i,in}^{f}-\frac{C^{f}D_{H_2}^{eff}S_{i,1}}{\delta^{A}}(y_{H_2\text{-}i,1}^{f}-y_{H_2\text{-}i,1}^{cat})-\frac{C^{f}D_{H_2O}^{eff}S_{i,1}}{\delta^{A}}(y_{H_2O\text{-}i,1}^{f}-y_{H_2O\text{-}i,1}^{cat}) \tag{4-32}$$

$$F_{i,1}^{a}=F_{i,in}^{a}-\frac{C^{a}D_{O_2}^{eff}S_{i,1}}{\delta^{C}}(y_{O_2\text{-}i,1}^{a}-y_{O_2\text{-}i,1}^{cat}) \tag{4-33}$$

For the tanks with $j = n_j$, corresponding to the outlet section of fuel and air gas channels, we define mean outlet variables as:

$$F_{out}^{f}=\frac{\sum_{i=1}^{n_i}F_{i,n_j}^{f}}{n_i};\ y_{H_2\text{-}out}^{f}=\frac{\sum_{i=1}^{n_i}y_{H_2\text{-}i,n_j}^{f}F_{i,n_j}^{f}}{F_{out}^{f}};\ T_{out}^{f}=\frac{\sum_{i=1}^{n_i}T_{i,n_j}^{f}F_{i,n_j}^{f}}{F_{out}^{f}} \tag{4-34}$$

$$F_{out}^{a}=\frac{\sum_{i=1}^{n_i}F_{i,n_j}^{a}}{n_i};\ y_{O_2\text{-}out}^{a}=\frac{\sum_{i=1}^{n_i}y_{O_2\text{-}i,n_j}^{a}F_{i,n_j}^{a}}{F_{out}^{a}};\ T_{out}^{a}=\frac{\sum_{i=1}^{n_i}T_{i,n_j}^{a}F_{i,n_j}^{a}}{F_{out}^{a}} \tag{4-35}$$

The developed mathematical model takes into account the following phenomena:

- Convective mass transport in fuel and air gas channels of each compartment;
- Transvers transport of gases in the catalyst layers of each compartment;
- Electrochemical oxidation of hydrogen at the anode-electrolyte interface;
- Electrochemical reduction of oxygen in the cathode-electrolyte interface;
- Charge balances at electrode-electrolyte interfaces;
- Energy balances in fuel and air gas channels and for the PEN structure (solid phase) of each compartment.

4.2.3. TSR Model for the Counter-Current Flow Direction

Figure 4.1b illustrates the application of the tank in series model (TSR) for counter-current flow of fuel and air in a planar solid oxide fuel cell. An appropriate unsteady state TSR model with counter-flow of fuel and air is obtained from material balances as follows:

$$C^{f} V^{f}_{gas-i,j} \frac{dy^{f}_{H_2\text{-}i,j}}{S_{i,j}.dt} = y^{f}_{H_2\text{-}i,j-1} \frac{F^{f}_{i,j-1}}{S_{i,j}} - y^{f}_{H_2\text{-}i,j} \frac{F^{f}_{i,j}}{S_{i,j}} - \frac{C^{f} D^{eff}_{H_2}}{\delta^{A}} (y^{f}_{H_2\text{-}i,j} - y^{cat}_{H_2\text{-}i,j}) \qquad (4\text{-}36)$$

$$C^{f} V^{f}_{gas-i,j} \frac{dy^{f}_{H_2O\text{-}i,j}}{S_{i,j}.dt} = y^{f}_{H_2O\text{-}i,j-1} \frac{F^{f}_{i,j-1}}{S_{i,j}} - y^{f}_{H_2O\text{-}i,j} \frac{F^{f}_{i,j}}{S_{i,j}} - \frac{C^{f} D^{eff}_{H_2O}}{\delta^{A}} (y^{f}_{H_2O\text{-}i,j} - y^{cat}_{H_2O\text{-}i,j}) \qquad (4\text{-}37)$$

$$C^{a} V^{a}_{gas-i,j} \frac{dy^{a}_{O_2\text{-}i,j}}{S_{i,j}.dt} = y^{a}_{O_2\text{-}i,j+1} \frac{F^{a}_{i,j+1}}{S_{i,j}} - y^{a}_{O_2\text{-}i,j} \frac{F^{a}_{i,j}}{S_{i,j}} - \frac{C^{a} D^{eff}_{O_2}}{\delta^{C}} (y^{a}_{O_2\text{-}i,j} - y^{cat}_{O_2\text{-}i,j}) \qquad (4\text{-}38)$$

In the counter-flow scheme, the fuel side exit streams from thank ($_{i,\ j-1}$) are also the inlet streams into tank ($_{i,j}$). In the air gas channels of each compartment, the exit streams from tank ($_{i,\ j+1}$) are also the inlet streams into tank ($_{i,j}$); therefore, the exiting flow rates from the fuel gas channels depend on the flow rates of the previous tank, and the exiting flow rate from the air gas channels depends on the flow rate of a forward tank.

$$F^{f}_{i,j} = F^{f}_{i,j-1} - \frac{C^{f} D^{eff}_{H_2} S_{i,j}}{\delta^{A}} (y^{f}_{H_2\text{-}i,j} - y^{cat}_{H_2\text{-}i,j}) - \frac{C^{f} D^{eff}_{H_2O} S_{i,j}}{\delta^{A}} (y^{f}_{H_2O\text{-}i,j} - y^{cat}_{H_2O\text{-}i,j}) \quad (4\text{-}39)$$

$$F^{a}_{i,j} = F^{a}_{i,j+1} - \frac{C^{a} D^{eff}_{O_2} S_{i,j}}{\delta^{C}} (y^{a}_{O_2\text{-}i,j} - y^{cat}_{O_2\text{-}i,j}) \quad (4\text{-}40)$$

The species balance equations for the ij -tank volume in the anode and cathode catalyst layers are written as equations (4-19) to (4-21). The energy balances for the fuel and air gas channels for each compartment ($tank_{i,j}$) are written as follows, and those for the PEN structure are the same as those in equation (4-26).

$$C^{f} V^{f}_{gas-i,j} c^{f}_{p} \frac{dT^{f}_{i,j}}{S_{i,j}.dt} = (\frac{F^{f}_{i,j-1}}{S_{i,j}} h^{f}_{i,j-1} - \frac{F^{f}_{i,j}}{S_{i,j}} h^{f}_{i,j}) + R^{f}_{h\text{-}i,j} \quad (4\text{-}41)$$

$$C^{a} V^{a}_{gas-i,j} c^{a}_{p} \frac{dT^{a}_{i,j}}{S_{i,j}.dt} = (\frac{F^{a}_{i,j+1}}{S_{i,j}} h^{a}_{i,j+1} - \frac{F^{a}_{i,j}}{S_{i,j}} h^{a}_{i,j}) + R^{a}_{h\text{-}i,j} \quad (4\text{-}42)$$

The charge balance equations for the anode-electrolyte and the cathode-electrolyte interfaces are the same as those in equations (4-27) and (4-28). For the tanks with $j = 1$ and $j = n_j$, corresponding to the inlet section for counter-flow of fuel and air, respectively, we obtain:

$$C^{f} V^{f}_{gas-i,1} \frac{dy^{f}_{H_2\text{-}i,1}}{S_{i,1}.dt} = y^{f}_{H_2\text{-}in} \frac{F^{f}_{i,in}}{S_{i,1}} - y^{f}_{H_2\text{-}i,1} \frac{F^{f}_{i,1}}{S_{i,1}} - \frac{C^{f} D^{eff}_{H_2}}{\delta^{A}} (y^{f}_{H_2\text{-}i,1} - y^{cat}_{H_2\text{-}i,1}) \quad (4\text{-}43)$$

$$C^{f} V^{f}_{gas-i,1} \frac{dy^{f}_{H_2O\text{-}i,1}}{S_{i,1}.dt} = y^{f}_{H_2O\text{-}in} \frac{F^{f}_{i,in}}{S_{i,1}} - y^{f}_{H_2O\text{-}i,1} \frac{F^{f}_{i,1}}{S_{i,1}} - \frac{C^{f} D^{eff}_{H_2O}}{\delta^{A}} (y^{f}_{H_2O\text{-}i,1} - y^{cat}_{H_2O\text{-}i,1}) \quad (4\text{-}44)$$

$$C^{a} V^{a}_{gas-i,n_j} \frac{dy^{a}_{O_2\text{-}i,1}}{S_{i,n_j}.dt} = y^{a}_{O_2\text{-}in} \frac{F^{a}_{i,in}}{S_{i,n_j}} - y^{a}_{O_2\text{-}i,n_j} \frac{F^{a}_{i,n_j}}{S_{i,n_j}} - \frac{C^{a} D^{eff}_{O_2}}{\delta^{C}} (y^{a}_{O_2\text{-}i,n_j} - y^{cat}_{O_2\text{-}i,n_j}) \quad (4\text{-}45)$$

$$F^{f}_{i,1} = F^{f}_{i,in} - \frac{C^{f} D^{eff}_{H_2} S_{i,1}}{\delta^{A}} (y^{f}_{H_2\text{-}i,1} - y^{cat}_{H_2\text{-}i,1}) - \frac{C^{f} D^{eff}_{H_2O} S_{i,1}}{\delta^{A}} (y^{f}_{H_2O\text{-}i,1} - y^{cat}_{H_2O\text{-}i,1}) \quad (4\text{-}46)$$

$$F^{a}_{i,n_j} = F^{a}_{i,in} - \frac{C^{a} D^{eff}_{O_2} S_{i,n_j}}{\delta^{C}} (y^{a}_{O_2\text{-}i,n_j} - y^{cat}_{O_2\text{-}i,n_j}) \quad (4\text{-}47)$$

For tanks with $j = 1$ and $j = n_j$, corresponding to the outlet section for co-flow of air and fuel, respectively, we define mean outlet variables as follows:

$$F^{f}_{out} = \frac{\sum_{i=1}^{n_i} F^{f}_{i,n_j}}{n_i};\ y^{f}_{H_2\text{-}out} = \frac{\sum_{i=1}^{n_i} y^{f}_{H_2\text{-}i,n_j} F^{f}_{i,n_j}}{F^{f}_{out}};\ T^{f}_{out} = \frac{\sum_{i=1}^{n_i} T^{f}_{i,n_j} F^{f}_{i,n_j}}{F^{f}_{out}} \tag{4-48}$$

$$F^{a}_{out} = \frac{\sum_{i=1}^{n_i} F^{a}_{i,1}}{n_i};\ y^{a}_{O_2\text{-}out} = \frac{\sum_{i=1}^{n_i} y^{a}_{O_2\text{-}i,1} F^{a}_{i,1}}{F^{a}_{out}};\ T^{a}_{out} = \frac{\sum_{i=1}^{n_i} T^{a}_{i,1} F^{a}_{i,1}}{F^{a}_{out}} \tag{4-49}$$

4.2.4. TSR Model for the Cross-Flow Direction

The coupling of reactor elements shown in Figure 4.1c is the basis for our analysis of planar cross-flow SOFC as a chemical reactor. The detailed species balance equations for cross-flow of fuel and air gas channels at each compartment are written as follows:

$$C^{f} V^{f}_{gas-i,j} \frac{dy^{f}_{H_2\text{-}i,j}}{S_{i,j}.dt} = y^{f}_{H_2\text{-}i,j-1} \frac{F^{f}_{i,j-1}}{S_{i,j}} - y^{f}_{H_2\text{-}i,j} \frac{F^{f}_{i,j}}{S_{i,j}} - \frac{C^{f} D^{eff}_{H_2}}{\delta^{A}} (y^{f}_{H_2\text{-}i,j} - y^{cat}_{H_2\text{-}i,j}) \tag{4-50}$$

$$C^{f} V^{f}_{gas-i,j} \frac{dy^{f}_{H_2O\text{-}i,j}}{S_{i,j}.dt} = y^{f}_{H_2O\text{-}i,j-1} \frac{F^{f}_{i,j-1}}{S_{i,j}} - y^{f}_{H_2O\text{-}i,j} \frac{F^{f}_{i,j}}{S_{i,j}} - \frac{C^{f} D^{eff}_{H\ O}}{\delta^{A}} (y^{f}_{H_2O\text{-}i,j} - y^{cat}_{H_2O\text{-}i,j}) \tag{4-51}$$

$$C^{a} V^{a}_{gas-i,j} \frac{dy^{a}_{O_2\text{-}i,j}}{S_{i,j}.dt} = y^{a}_{O_2\text{-}i-1,j} \frac{F^{a}_{i-1,j}}{S_{i,j}} - y^{a}_{O_2\text{-}i,j} \frac{F^{a}_{i,j}}{S_{i,j}} - \frac{C^{a} D^{eff}_{O_2}}{\delta^{C}} (y^{f}_{O_2\text{-}i,j} - y^{cat}_{O_2\text{-}i,j}) \tag{4-52}$$

In the cross-flow scheme, the fuel side exit streams from tank $(i,\ j-1)$, are also the inlet streams into tank (i,j). In the air gas channels of each compartment, the exit streams from tank $(i-1,\ j)$, are also the inlet streams into tank (i,j); therefore, the exiting flow rates from the fuel and air gas channels are defined as follows:

$$F^{f}_{i,j} = F^{f}_{i,j-1} - \frac{C^{f} D^{eff}_{H_2} S_{i,j}}{\delta^{A}} (y^{f}_{H_2\text{-}i,j} - y^{cat}_{H_2\text{-}i,j}) - \frac{C^{f} D^{eff}_{H_2O} S_{i,j}}{\delta^{A}} (y^{f}_{H_2O\text{-}i,j} - y^{cat}_{H_2O\text{-}i,j}) \tag{4-53}$$

$$F^{a}_{i,j} = F^{a}_{i-1,j} - \frac{C^{a} D^{eff}_{O_2} S_{i,j}}{\delta^{C}} (y^{a}_{O_2\text{-}i,j} - y^{cat}_{O_2\text{-}i,j}) \tag{4-54}$$

The species balance equations for $_{ij}$ -tank volume in anode and cathode catalyst layer and the charge balance equations for the anode/electrolyte and the cathode/electrolyte interfaces are written the same as for co and counter flow direction. The energy balances for the fuel and air gas channels for each compartment (tank$_{i,\,j}$) are written as follows and again for the PEN structure is the same as equation (4-26).

$$C^{f} V^{f}_{gas-i,j} c^{f}_{p} \frac{dT^{f}_{i,j}}{S_{i,j}.dt} = (\frac{F^{f}_{i,j-1}}{S_{i,j}} h^{f}_{i,j-1} - \frac{F^{f}_{i,j}}{S_{i,j}} h^{f}_{i,j}) + R^{f}_{h-i,j} \tag{4-55}$$

$$C^{a} V^{a}_{i,j} c^{a}_{p} \frac{dT^{a}_{i,j}}{S_{i,j}.dt} = (\frac{F^{a}_{i-1,j}}{S_{i,j}} h^{a}_{i-1,j} - \frac{F^{a}_{i,j}}{S_{i,j}} h^{a}_{i,j}) + R^{a}_{h-i,j} \tag{4-56}$$

For the tanks $j = n_j$ and $i = n_i$ corresponding to the outlet section for co-flow of fuel and air we define mean outlet variables as follows:

$$F^{f}_{out} = \frac{\sum_{i=1}^{n_i} F^{f}_{i,n_j}}{n_i};\ y^{f}_{H_2\text{-}out} = \frac{\sum_{i=1}^{n_i} y^{f}_{H_2\text{-}i,n_j} F^{f}_{i,n_j}}{F^{f}_{out}};\ T^{f}_{out} = \frac{\sum_{i=1}^{n_i} T^{f}_{i,n_j} F^{f}_{i,n_j}}{F^{f}_{out}} \tag{4-57}$$

$$F^{a}_{out} = \frac{\sum_{j=1}^{n_j} F^{a}_{n_i,j}}{n_j};\ y^{a}_{O_2\text{-}out} = \frac{\sum_{j=1}^{n_j} y^{a}_{O_2\text{-}n_i,j} F^{a}_{n_i,j}}{F^{a}_{out}};\ T^{a}_{out} = \frac{\sum_{j=1}^{n_j} T^{a}_{n_i,j} F^{a}_{n_i,j}}{F^{a}_{out}} \tag{4-58}$$

4.2.5. Electrochemical Sub-Model

Assuming the electrochemical reactions at the anode-electrolyte and cathode-electrolyte are given by equations (3-1) and (3-2) respectively, the full expression of the Butler-Volmer equation was used for the local Faradic current densities as equations (3-30) and (3-31).

$$i^{A}_{F-i,j} = i^{A}_{0}[\exp(\frac{\alpha^{A}_{A} F \eta^{A}_{act-i,j}}{RT_{i,j}}) - \exp(-\frac{\alpha^{A}_{C} F \eta^{A}_{act-i,j}}{RT_{i,j}})] \tag{4-59}$$

$$i^{C}_{F-i,j} = i^{C}_{0}[\exp(\frac{\alpha^{C}_{A} F \eta^{C}_{act-i,j}}{RT_{i,j}}) - \exp(-\frac{\alpha^{C}_{C} F \eta^{C}_{act-i,j}}{RT_{i,j}})] \tag{4-60}$$

In the above equations, $\eta^{A}_{act-i,j} = \eta^{A}_{i,j} - \eta^{A}_{eq-i,j}$ and $\eta^{C}_{act-i,j} = \eta^{C}_{i,j} - \eta^{C}_{eq-i,j}$ in which, $\eta^{A}_{i,j}$ and $\eta^{C}_{i,j}$ are obtained from equations (4-27) and (4-28); $\eta^{A}_{eq-i,j}$ and $\eta^{A}_{eq-i,j}$ are calculated from equations (3-37) and (3-38). Additionally, for SOFC operated under potentiostatic mode (constant voltage) the current density in electrolyte media is found from equation (3-28), which is modified as follows:

$$i_{elyt-i,j} = \frac{\sigma_{elyt}}{\delta_{elyt}}\left(\eta^{C}_{i,j} - E_{cell} - \eta^{A}_{i,j}\right) \tag{4-61}$$

4.2.6. Mass Transfer Source Terms

The component concentration at electrode/electrolyte interface is calculated from flux continuity equation. In fuel cells, the reacting species are transferred from the channel through the porous electrode to electrode/electrolyte interface. The effect of electrochemical reaction on the species concentrations is included in the component flux from the channel to catalyst layer, ($S_{i,j} = S_{cell}/(n_i n_j)$).

$$R_{r,H_2-i,j} = \frac{\nu_{H_2} i^{A}_{F-i,j}}{n^{A}_{e} F} \tag{4-62}$$

$$R_{r,H_2O-i,j} = \frac{\nu_{H_2O} i^{A}_{F-i,j}}{n^{A}_{e} F} \tag{4-63}$$

$$R_{r,O_2-i,j} = \frac{\nu_{O_2} \left| i^{C}_{F-i,j} \right|}{n^{C}_{e} F} \tag{4-64}$$

4.2.7. Heat Transfer Source Terms

The heat transfer equation defines the continuity of heat flux condition in fuel and air gas channels of each compartment and for the PEN structure are defined as follows[96].

$$R^{f}_{h-i,j} = \hbar^{f}\left(T^{PEN}_{i,j} - T^{f}_{i,j}\right) \tag{4-65}$$

$$R^{a}_{h-i,j} = \hbar^{a}\left(T^{PEN}_{i,j} - T^{a}_{i,j}\right) \tag{4-66}$$

$$R_{h\text{-}i,j}^{PEN} = (-\frac{\Delta H_{elec}}{2F} - E_{cell}).i_{cell\text{-}i,j} + (\hbar^{f} + \frac{(c_{p,H_2} - c_{p,H_2O})}{2F} i_{cell\text{-}i,j})(T_{i,j}^{f} - T_{i,j}^{PEN}) + (\hbar^{a} + \frac{c_{p,O_2}}{4F} i_{cell\text{-}i,j})(T_{i,j}^{a} - T_{i,j}^{PEN}) \quad (4\text{-}67)$$

Constitutive equations for physical and thermo-physical properties and convective heat transfer coefficient are taken from the literature[96, 111].

4.3. Numerical Approach in TSR Model

For modelling SOFC with CSTR reactor network as a tank in series (TSR) model we used the operating conditions and geometrical parameters from the work of Ravussin et al. [112]. The fuel gas channels are fed with a gas mixture of 97% H2 and 3% H2O and the inlet air composition at the air gas channels is 21% oxygen and 79% nitrogen. The number of tanks (CSTR reactor) in TSR model can be estimated from bench or numerical experiments. For planar SOFC we set the number of tanks as $n_i = 8$ and $n_j = 8$ corresponding to the TSR model with 704 $(8 \times 8 \times 11)$ nonlinear coupled first order ordinary differential equations. Figure 4.3 shows the flowchart of the solution technique that is developed for the co-current flow direction. This model was implemented in MATLAB and it was initialized with the feed composition and temperature. MATLAB has a number of tools for solving ordinary differential equations. We used one of its rudimentary solvers, ode15s, which was established based on the backward differentiation formula (BDFs, also known as Gear's method) [113, 114]. The geometry and electrochemical parameters of anode and cathode catalyst layers and the operating conditions are listed in Table 4.1 and Table 4.2 respectively.

4.4. Simulation Results and Discussion

4.4.1. Evaluation of the Results from TSR Model

A comparison of the simulated and experimental V-I curve is shown in Figure 4.4. It was observed that the predicted V-I curves had a similar shape to that of the

experimental data[112] reported for counter-current flow of fuel and air. Although the limiting current deviates from the experiments, the simulation results showed similar tailing effects at high current density.

Table 4.1 - Geometry and model input parameters for the planar SOFC in TSR model

Parameter	**Anode**	**Cathode**
Catalyst thickness δ, m	0.25×10^{-3}	0.03×10^{-3}
Porosity ε	0.4	0.4
Pre-exponential kinetic factor γ, A m^{-2}	2.9×10^{8}	7.0×10^{8}
Activation Energy, $J.mol^{-1}$	120000	120000
Charge transfer coefficient α_A	2	1.4
Charge transfer coefficient α_C	1	0.6
Channel height , m	0.75×10^{-3}	
Section area, m^2	5×10^{-3}	
Electrolyte thickness, m	1×10^{-5}	

Table 4.2 - Operating conditions for the planar SOFC in TSR model

Parameter	**Value**
Fuel flow rate, $(mole.s^{-1})$	5.07×10^{-5}
Oxidant flow rate, $(mole.s^{-1})$	6.17×10^{-4}
H_2 mole fraction in fuel	0.97
O_2 mole fraction in oxidant	0.2
Temperature, (K)	1073
Pressure, (atm.)	1

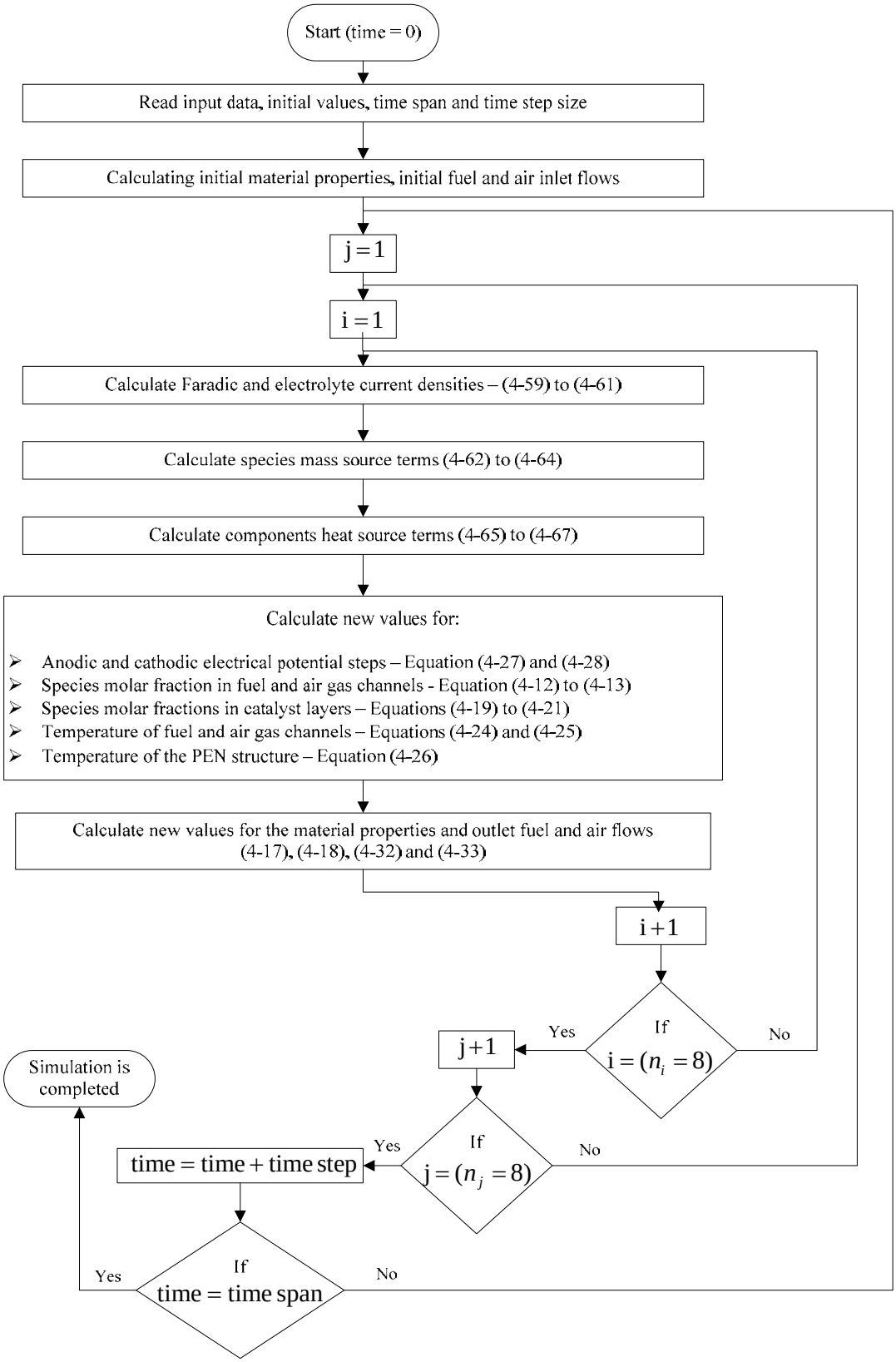

Figure 4.3 - Flowchart of the solution technique for TSR model (Co-Flow)

The deviation of TSR model with $n_i = 8, n_j = 8$ indicates that flow patterns in channels changed with flow rate. The voltage drop at high current density was largely due to the concentration loss, especially at the anode side; therefore, the main reason for this discrepancy was due to non-uniformity of the fuel distribution and at high current density this effect is more significant. High volumetric flow rate of the fuel flow leads to increase uniformity of fuel distribution and also the reaction rates across the active area. Low volumetric flow rates of the fuel flow, on the other hand, leads to non-homogeneous distribution of fuel within the anode compartments; therefore assuming the uniform flow distribution at this study, the predicted V-I curve for the SOFC operating with 400 ml/min of hydrogen fuel, agreed best with the experimental values. The normalized least squares error $\mathrm{LSE}(i)$, in the cell current was calculated for the three cases with different fuel inlet flow rates so as to quantify the deviation of the model from the experimental results.

$$\mathrm{LSE}(i) = \sum_{\aleph=1,\ldots m} \left(e(i)_{\aleph}\right)^2 \tag{4-68}$$

$$e(i)_{\aleph} = \frac{i_{exp,\aleph} - i_{sim,\aleph}}{(i_{exp,\aleph} - i_{sim,\aleph})_{max}} \tag{4-69}$$

Where $e(i)_{\aleph}$ is the normalized error between the experimental and the simulated values of the current density (i). $\aleph$, represents the 'm' number of voltage points for which the errors in current density are calculated; i_{exp} and i_{sim} represent the experimental and the simulated values of the cell current density respectively. The normalized least squares error for the case of 400 ml/min inlet fuel flow rate was 1.9 and those for the cases of 260 ml/min and 180 ml/min fuel inlet flow rates are 2.26 and 2.32 respectively. It can be seen that the model accuracy is better at high fuel flow rates. Additionally average temperature, current density and the fuel and air utilization with different fuel and air flow directions are itemized in Table 4.3.

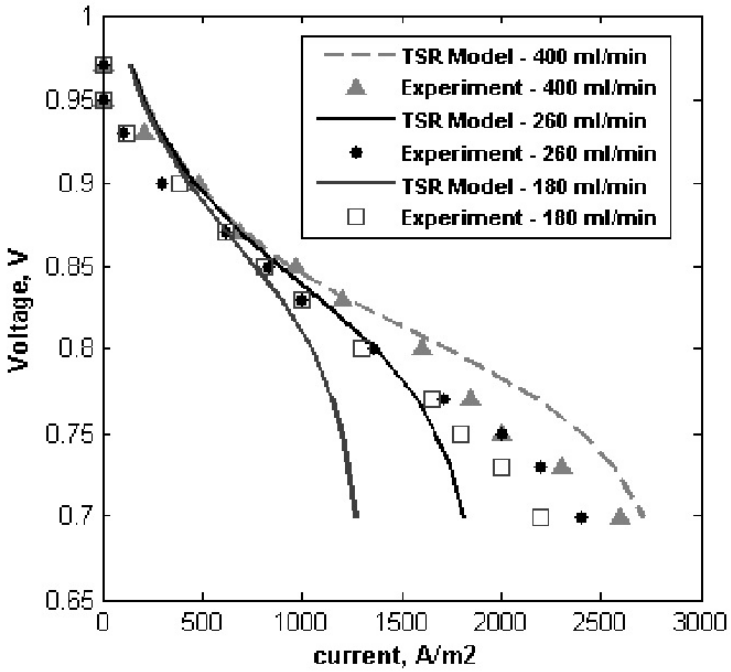

Figure 4.4 - Comparison of the predicted V-I curve from TSR model with experimental data (Counter-Flow) [112]

Table 4.3 - Single cell stack simulation results for different fuel and air flow configurations (Cell voltage = 0.8 V)

Parameter	Co - Flow	Counter - Flow	Cross - Flow
T^{a}_{avg}	1150	1136	1148
T^{a}_{Out}	1216	1235	1223
T^{f}_{avg}	1174	1163	1177
T^{f}_{Out}	1237	1094	1134
T^{PEN}_{avg}	1177	1168	1178
i^{A}_{avg}	1741	1708	1688
FU %	58.5	57	52.5
AU %	12.1	12.3	12.2

Average anode current density at electrode/electrolyte interface was calculated as the mean surface. Under steady state condition, differences among the fuel and air utilization, average current density and temperatures for the fuel and air channels

and for the PEN structure of co, counter and cross flow directions provide support for the influence of the flow direction on the SOFC performance. Fuel utilization and air utilization coefficients are defined as follows:

$$FU = 1 - \frac{y^{f}_{H_2\text{-out}} F^{f}_{out}}{y^{f}_{H_2\text{-in}} F^{f}_{in}} \tag{4-70}$$

$$AU = 1 - \frac{y^{a}_{O_2\text{-out}} F^{a}_{out}}{y^{a}_{O_2\text{-in}} F^{a}_{in}} \tag{4-71}$$

The TSR model is able to predict two-dimensional distribution of concentration, temperature and current density in planar SOFC. Using arrays of several tanks in series, we were able to detect current heterogeneities along the cell array and regions of higher-current densities in the fuel cell.

4.4.2. Steady State Simulation Results from TSR Model

The steady state simulation results for SOFC with different flow directions are given in Figure 4.5 – Figure 4.7. It is shown that decreasing the oxygen concentration through the air flow direction results from the electrochemical reaction at the cathode catalyst layer. For the species concentration among different flow configurations, the primary difference was the two dimensional nature of the cross flow case in comparison with co and counter flow cases. For the co and counter flow direction, the H_2 concentration profile across the full width of the cell decreases uniformly but for the cross flow case we have a minimum point at one side and a maximum point at the other side of the cell width and along the fuel flow direction. When trying to maximize fuel utilization, the minimum point increases severity of the thermal stresses. The concentration of water in fuel gas channels increases due to the component flux from the anode catalyst to the gas channel. In each flow configurations, the PEN temperature increased along the air flow direction and reaching a maximum near the air outlet; that is due to the air flow that was most effective in cooling near the air inlet and carried heat generated in the PEN structure toward the air outlet. Of the three flow configurations, the co-flow direction had the most uniform temperature distribution and smallest temperature difference from the air and fuel inlets to outlets and this is due to the offsetting

effects of the air inlet that is aligned with the fuel inlet. For the counter and cross flow cases, the PEN temperature was highest near the fuel inlet and air outlet. Despite the co and counter flow direction again, the PEN temperature of the cross flow case had two dimensional natures and the most non-uniform distribution. The temperature variation is important for evaluation of thermally-induced stresses due to temperature gradient. Consistent with the temperature distribution, the current density was most uniform in the co-flow case.

In the cross and counter flow direction, current density was high near the fuel inlet and air outlet. Two dimensional nature of the current density for the cross-flow case near the fuel inlet was because of the cooling effect at the air inlet and lower concentration of oxygen at the air outlet. Generally, the cell performance decreases considerably with temperature decrease. This is mainly caused by an increase in both the Ohmic and activation overpotentials [115]. On the other hand, overpotential is strongly dependent on temperature and current density [116]. Increasing the current density causes the activation overpotential to be increased [117]; meanwhile, current density also takes into account the effects of reactants' concentration. As a result, histograms for the co and counter flow cases showed opposite trends in spatial domain, except overpotential and current density. For the co flow SOFC, activation overpotential decreased along the gas flows while the maximum current density was roughly midstream from the gas inlet to outlet due to combined effects of the PEN temperature increase and hydrogen concentration decrease. For the counter flow case, the high temperature region is interchanged and then the maximum current density is placed at the fuel inlet which causes the activation overpotential to become a bit higher at this region. Afterward, under the effects of temperature and current density, the activation overpotential decreased followed by gradual increase. The non-uniform current density reveals the influence of reactants' concentration and temperature distribution. Analysis of the steady-state current and temperature profiles shows that co-current direction of fuel and air provides the most uniform current and temperature distribution and the highest fuel utilization. Additionally, steady state results indicate that the TSR model presented in this work is able to predict the spatial distribution of the variables and can be used for preliminary studies instead of the more complex CFD models.

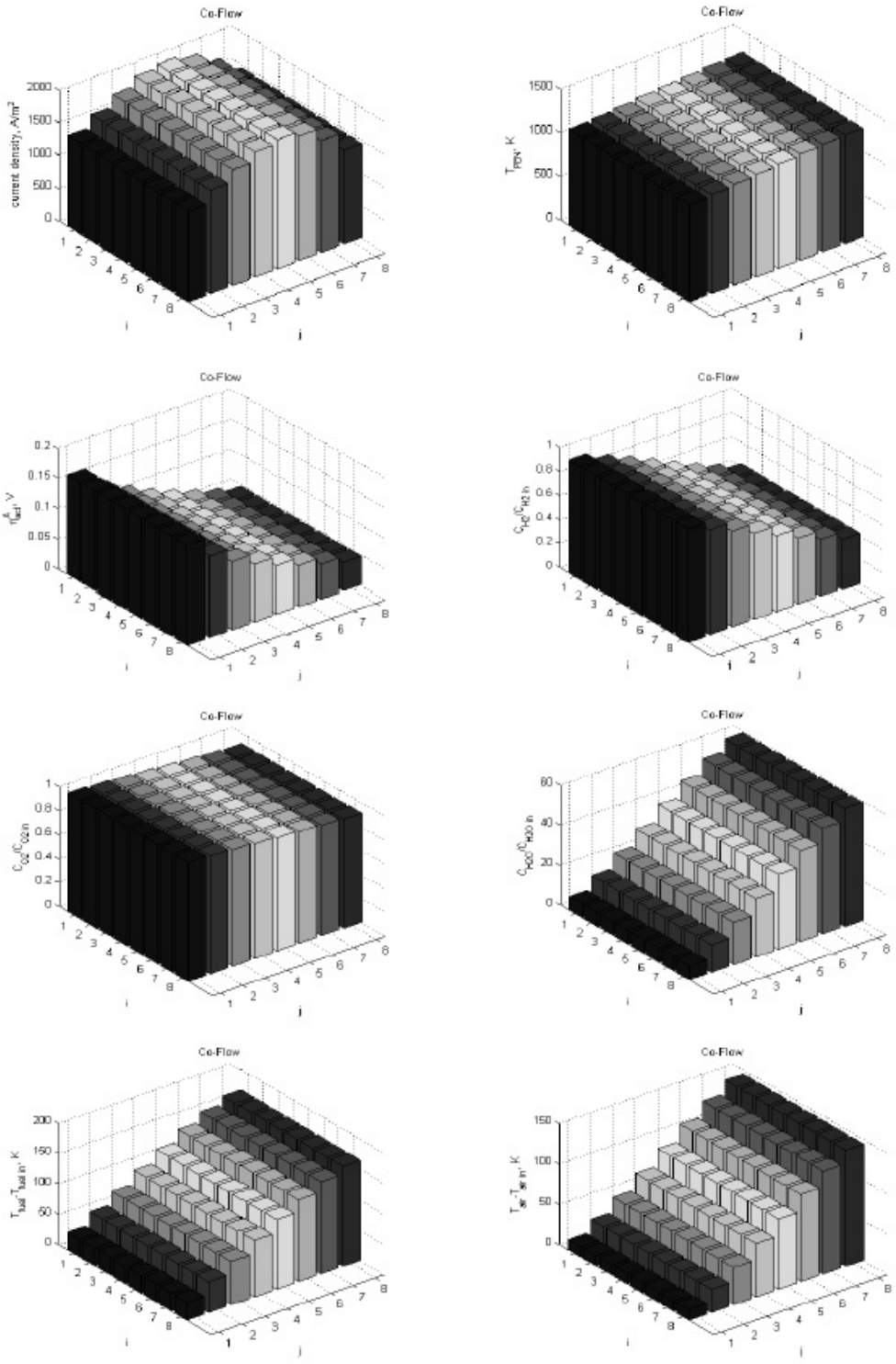

Figure 4.5 - Histograms with steady state simulation results predicted by TSR model for planar SOFC with co-flow direction of fuel and air ($E_{cell} = 0.8V$)

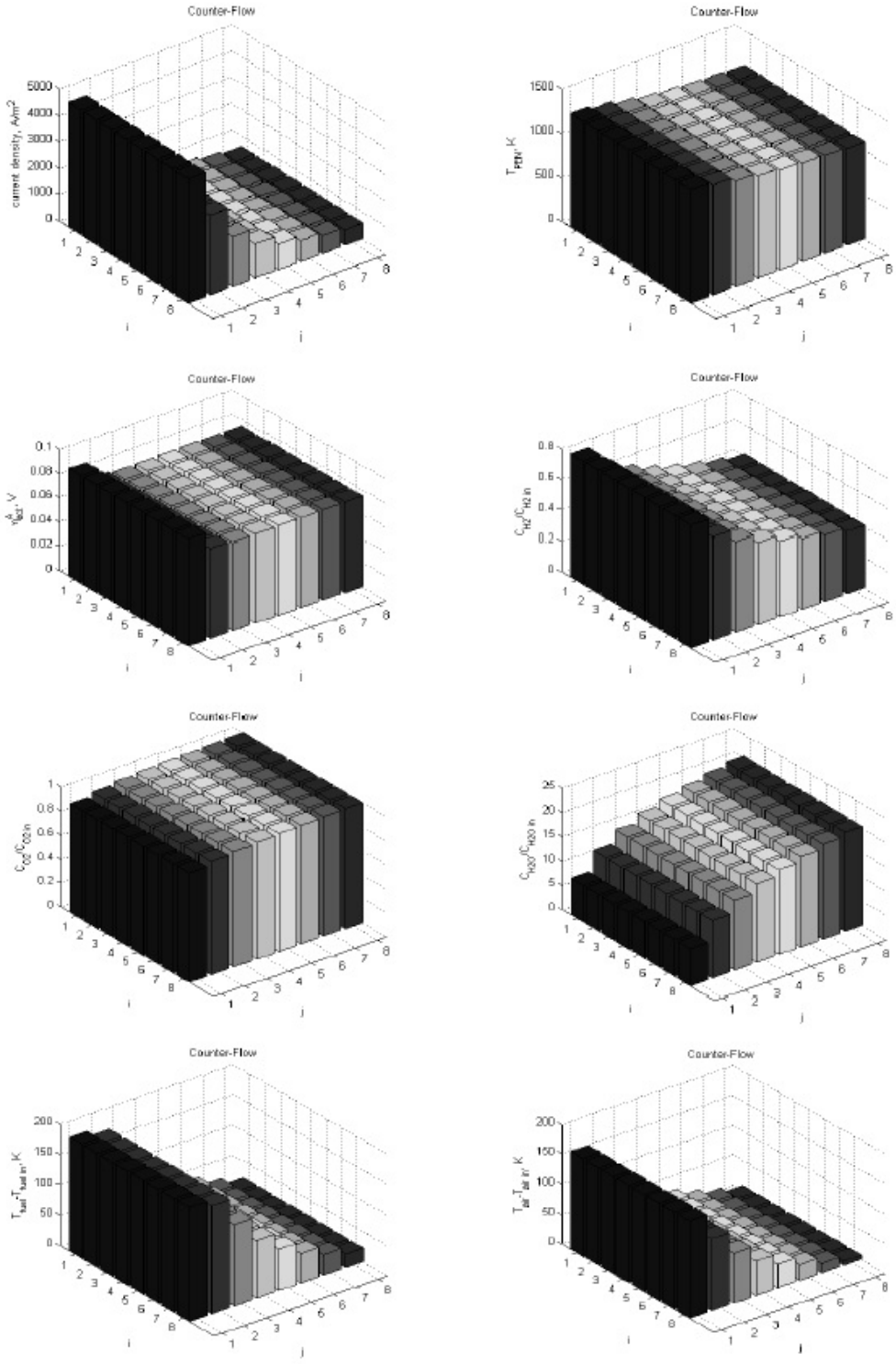

Figure 4.6 - Histograms with steady state simulation results predicted by TSR model for planar SOFC with counter-flow direction of fuel and air ($E_{cell} = 0.8V$)

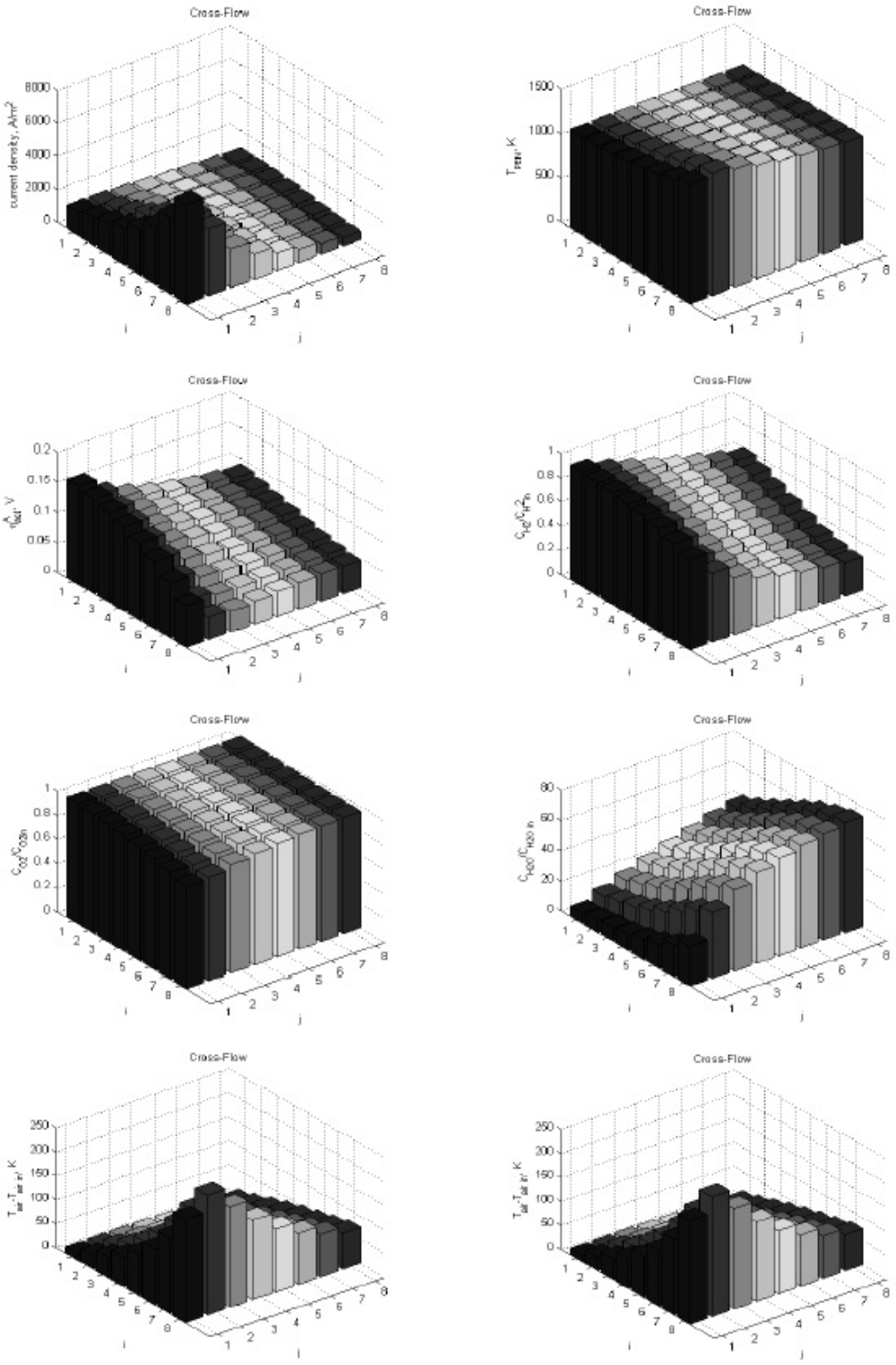

Figure 4.7 - Histograms with steady state simulation results predicted by TSR model for planar SOFC with cross-flow direction of fuel and air ($E_{cell} = 0.8V$)

4.4.3. Dynamic Simulation Results from TSR Model

Finally an investigation of transient behaviour was carried out. Such transient behaviours are critical to SOFC control development. SOFC operation is often subjected to transient condition in external load which can be either load current or load voltage. Since this model was used for simulating of the potentiostatic operating mode, in this section we analysed transient behaviours for the co-, counter and cross flow SOFC induced by the voltage step change from 0.8 to 0.85 volt after 20 seconds with the rest of the boundary conditions kept constant. Figures 4.8 to 4.10 show the cell dynamic responses for different fuel and air flow direction at three different representative points of the cell, CSTR (3, 3), CSTR (4, 4) and CSTR (5, 5).

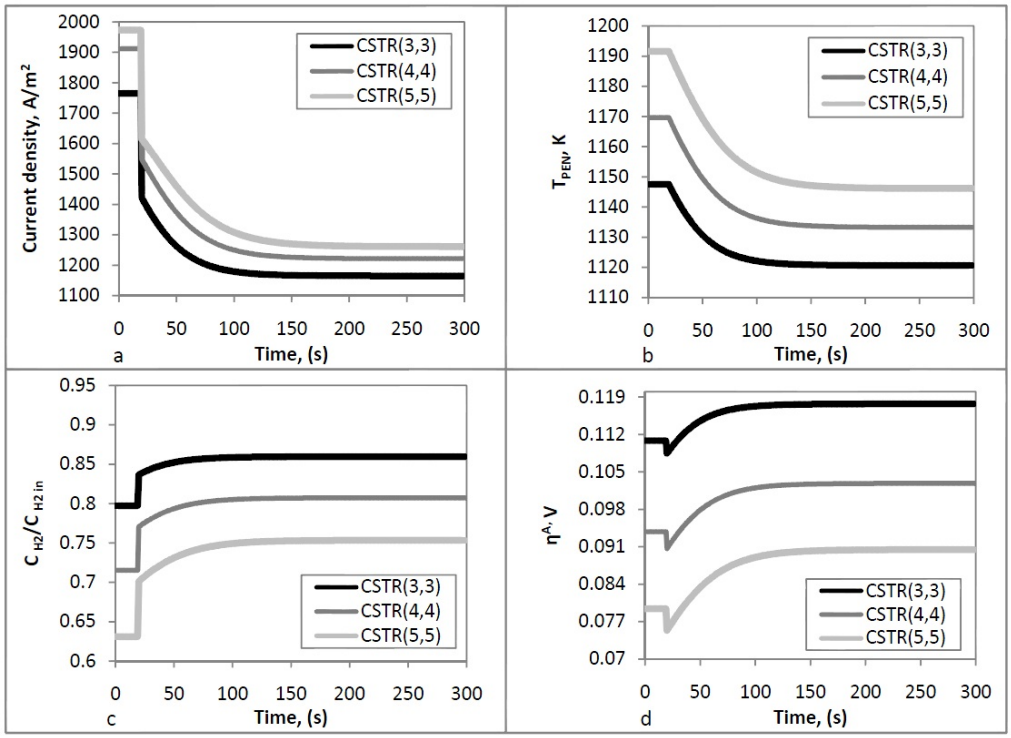

Figure 4.8 - Dynamic simulation results predicted by TSR model for planarSOFC with co-flow direction of fuel and air ($\Delta E_{cell} = +0.5V$)

As one can see from Figures 4.8 to 4.10, numerical dynamic results for the co, counter and cross flow direction show that the cell can obtain very quick current decrease when subjected to a voltage step increase, followed by a slow transient period, leading to the new steady state current. However the transient response of

the cell current density is very complex and related to all parametric changes which are associated with the entire fuel cell activity. The sudden step increase in the cell voltage induces the quick response of the charge transport within the PEN assembly, which leads to immediate decrease in the current density. At the instant of this momentary decrease in the current density, a sudden change in the mass source term of the component balance equation occurs and consequently the hydrogen concentration instantaneously increases, followed by a slow increase that is due to the diffusion effect until the overall system response becomes steady. Simultaneously, the fraction of hydrogen which has not being consumed in the electrochemical reaction accumulated toward the fuel outlets which can influence the slow dynamic of the current density along the fuel flow direction. For better comparison with the numerical steady state results, the hydrogen concentration is normalized with the value of the inlet boundary condition. The reduction of the current density also decreases the heat production which results in temperature decrease. The PEN temperature has the gentlest response and substantial effect on the electrolyte conductivity. Thus the PEN temperature decrease, on the other hand, causes further reduction of the local current density. The same trends of the transient responses obtained from the simulations of this model were also reported by other authors[66, 67, 73, 117-119].

From the Figures, it is evident that both the transient behaviour and the magnitude of the changes in the responses vary at different representative points, as well as with the flow directions. As it was shown in Figure 4.8, for the co flow direction, the magnitude of change for current, temperature, hydrogen concentration and activation overpotential increases toward the fuel and air outlets. This is due to the convective cooling effect of the air flow, which causes the low and high temperature regions to be placed at the air inlet and outlet respectively. At low temperature region, CSTR (3, 3), overpotential is higher which in turn diminishes dynamic response of the current density to the voltage step increase [120].The simulation results of the co flow direction indicate that despite the hydrogen concentration increase, the slow dynamics of the local current density is mainly influenced by the intensity and magnitude of temperature change which causes further decrease in current density. The response of the activation overpotential in

Figure 4.8d is consistent with temperature and current. After the first sudden decrease it shows moderate increase toward the new steady state value.

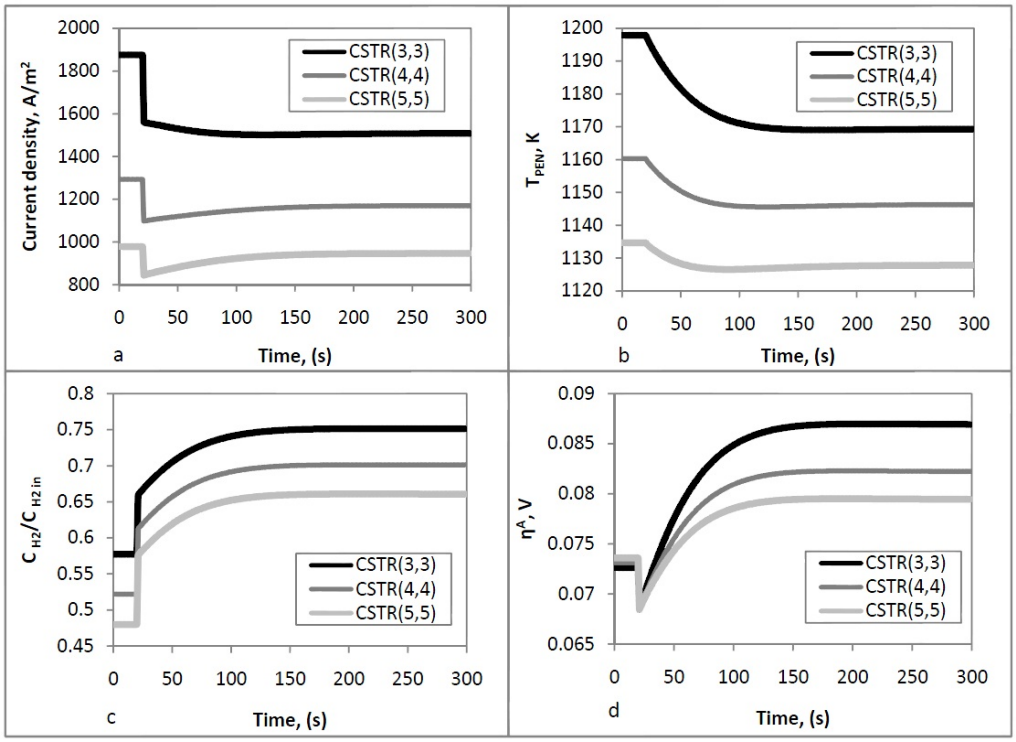

Figure 4.9 - Dynamic simulation results predicted by TSR model for planar SOFC with counter-flow direction of fuel and air ($\Delta E_{cell} = +0.5V$)

Contrary to the co flow case, the counter flow direction (Figure 4.9) shows almost opposite transient behaviour that is due to interchange of the air inlet and high temperature region. For the points near the air outlet, i.e. CSTR (3, 3), the magnitude of change for the local current density is considerably higher which leads to steep and large decrease of temperature. Thus for the points near the air outlet, the slow dynamic response of the local current density is mainly influenced by temperature. On the other hand, for the points near the fuel outlet, temperature change is significantly smaller; meanwhile, as we move toward the fuel outlet dynamic response of the current density tends to be characterized by the initial under-shoot followed by a slower transient that is due to the pronounced effect of the diffusion resistance within porous electrode, hydrogen accumulation toward the fuel outlets and less influence of the PEN temperature.

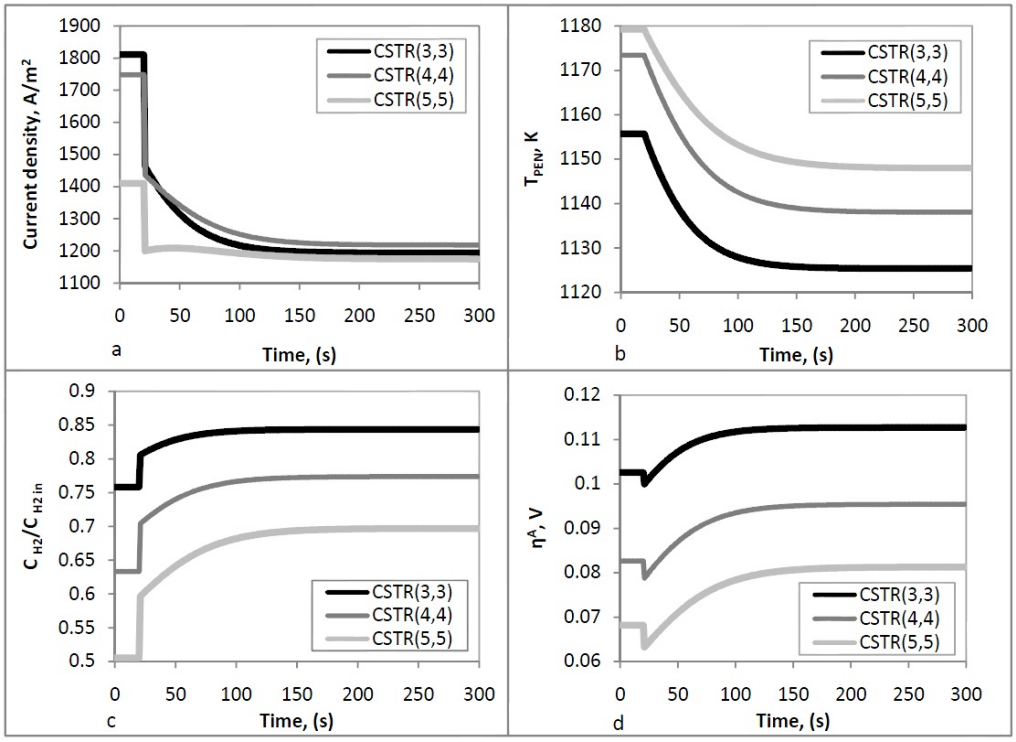

Figure 4.10 - Dynamic simulation results predicted by TSR model for planar SOFC with cross-flow direction of fuel and air ($\Delta E_{cell} = +0.5V$)

As one can see from Figure 4.10, the dynamic responses of the cross flow direction are absolutely consistent with the above justifications. Here under the effects of the cross flow direction of fuel and air, the transient behaviour is a little bit different. However the same as the counter flow direction, again for the points near the air and fuel inlets, i.e. CSTR (3, 3), small amount of hydrogen accumulates and the intensive change of temperature mainly affects the slow dynamic of the local current density. At the same time for the points near the outlets, accumulation of hydrogen increased; therefore, the slow dynamic of the current density is influenced by the combined effects of diffusion, hydrogen accumulation and temperature. Analysis of dynamic responses to a voltage step change show that the co flow direction of fuel and air provides the most uniform transient responses at different points of the cell, meanwhile, compared with the counter and cross flow direction, the PEN temperature dominates the slow dynamic of the current density and almost all dynamic behaviours.

The developed unsteady-state tank in series SOFC model with charge balance will provide a better understanding of main phenomena governing electrochemical reactions in fuel cells. Additionally, the results are useful in understanding the sensitivity of the SOFC performance to the fuel and air flow direction. Intensification of electrochemical processes can be achieved by changing the direction of fuel and air flow.

4.5. Summary

The tank in series model presented in this work takes into account the charge balances at the electrodes and electrolyte interfaces, species mass balances to the gas channels and diffusion layers, energy balances for the fuel and air channels and also for the PEN structures. All simulations were done under the potentiostatic operating mode and using the charge balance equations for the interface between the electron and ion conducting media facilitate calculation of the activation overpotential with no restriction concerning the number of the charge transfer steps. The simulation results from TSR model indicate the influence of flow direction on the steady state and dynamic performances of a planar SOFC with co, counter and cross flow direction of fuel and air. Examination of simulation results indicates the possibility of enhancing the fuel cell performance by decreasing the misdistribution of fields. The results demonstrate a strong coupling between the temperature, concentration, activation overpotential and current density distributions. Among different flow direction, the co-flow case is the most favourable for planar SOFC with improved performance and in response to a voltage step increase, provides the most uniform transient behaviour at different points of the cell. For the co flow direction, temperature dominates the slow dynamics of the local current density while in the low temperature regions of the counter and cross flow cases; the slow dynamics of the current density tends to be characterized by the initial under-shoot followed by a slower transient response. This is due to the combined effects of the diffusion resistance within porous electrode, hydrogen accumulation toward the fuel outlets and influence of the PEN temperature. Design is an iterative process where more and more refined models are required in each phase. The model presented in this work can serve as an early step in the iteration by means of accelerating 2D simulation to get the trend in the distribution of important

variables. Based on the results from this model, decisions on the need for more refined models may be taken. Using this model it is possible to take into account the hydrodynamic behaviour of different flow configurations. Moreover, the model computational time is much less compared to CFD models (less than 3 minutes to solve 704 ordinary differential equations). Future work will concentrate on the optimization of modelling and model based controller design to improve the performance of SOFC stack.

Chapter 5

The Combined Effects of Macro and Micro-Structural Parameters on Predicted Results from 3D Model of a Planar SOFC

5.1. Introduction

In the TSR model, the flow rates at the inlets of all the air and fuel flow channels are all assumed to be uniform. Since this does not provide a very realistic picture, the velocity profiles at the inlet of the channels would be obtained from CFD simulation of the flow field design. Additionally, with respect to different functionalities of the Ni-based electrodes to provide environment for the electrochemical and reforming reactions, not only the uniformity of flow distribution but also the SOFC electrode design is important to allow maximum utilization of the anode functional layers and to balance each of the transport processes and the reactions involved[3, 121]. In other words, micro-structural optimization of SOFC performance requires consideration of the interconnect geometry and flow field effects, in addition to the detailed micro-scale calculation for the anode diffusion layer [122]. In view of this, the purpose of this chapter is based on a research project in collaboration with Ceramic Fuel Cell Ltd. Melbourne-Australia, to analyse the combined effects of different anode flow field design and micro-structural parameters of the anode diffusion layer on the overall performance of the cell. To address this aim, first a 3D model accounting for the effects of different anode flow field design on pressure and velocity profiles is developed. Furthermore, the model is extended to include the effects of the anode micro-structural parameters on spatial distribution of temperature, reaction rates and species concentration profiles for a symmetrical half-layer array of an industrial planar SOFC stack.

5.2. Model Geometry

Figure 5.1a illustrates different anode flow field designs for a symmetrical half-layer array of the planar SOFC stack proposed by CFCL.

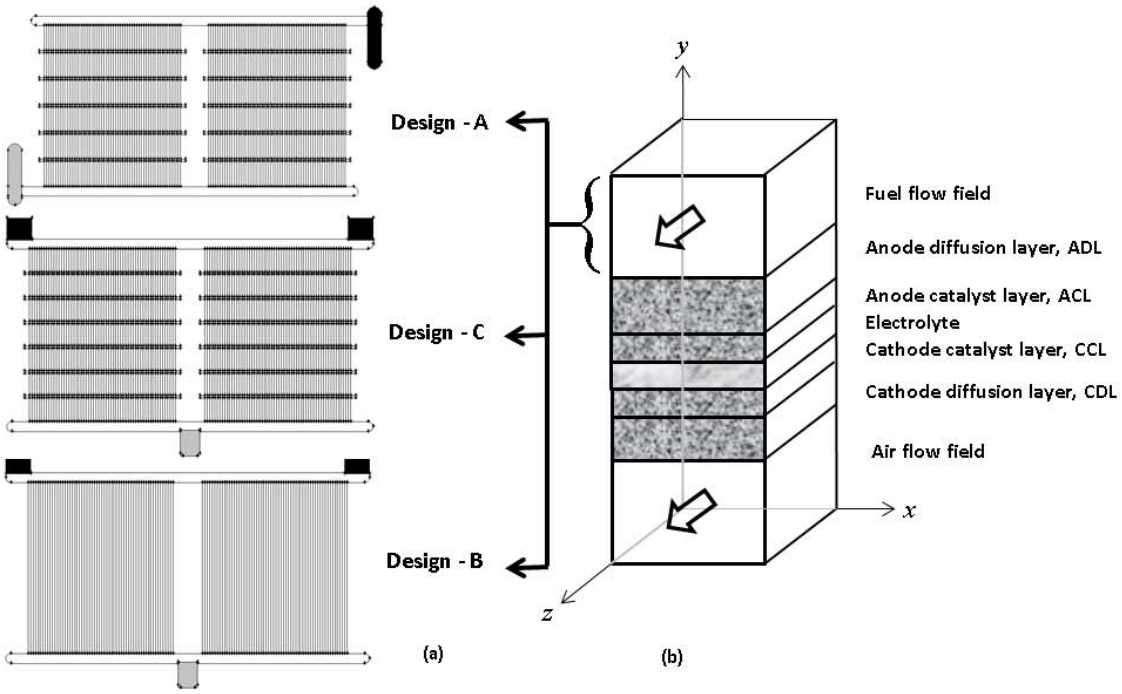

Figure 5.1 - a) Flow field design for a symmetrical half layer array of the SOFC stack consisting of two cells; b) Schematic view of the computational layers

Table 5.1 - Geometrical comparison among three anode flow field design

Flow field design	Channel design	Manifold design
A	Spot design	One inlet for two cells
B	Parallel design	Two inlets for two cells
C	Spot design	Two inlets for two cells

However, to analyse the combined effects of the geometrical factors, micro-structural parameters and catalytic chemical and electrochemical reactions on

pressure, velocity, temperature and species concentration profiles, a general frame work including similar fuel and air flow fields, anode and cathode diffusion layers and a thin film of the electrolyte that is sandwiched between the anode and cathode catalyst layers was considered in this work. Figure 5.1b shows 3D schematic view of these computational domains. Additionally, a comparison among three different flow field designs is summarized in Table 5.1.

5.3. CFD Modelling Assumptions and Equations

Generally, with attention to the computational time and accuracy of the simulation results, we need to make assumptions to reduce the complexity of the model to a manageable level whilst preserving the salient features of the problem at hand [123]. In this regards, the fluid flows can be modelled as incompressible and laminar due to small pressure gradients and flow velocities [124, 125]. Furthermore, gases in the SOFC can be thermodynamically modelled with the ideal gas assumption, because of the high temperature and moderate pressure of the gases in the cell [126]. In view of this, heat capacity, viscosity and thermal conductivity of the gas mixtures are calculated with the ideal gas mixing law of the species' individual values [63, 127]. Individual values are calculated from temperature-dependent polynomial curve [128]. Moreover, similar to the approach considered by Joen[129], the porous electrodes are assumed to be homogeneous bimodal mixture of the electron and ion conducting particles with identical radius within each of the electrode domains. With respect to the modelling equations and based on these assumptions, it should be noted that understanding and predicting SOFC behaviour implies simultaneous calculation of various coupled phenomena, which can be classified into the following categories: (1) mass transfer in fuel flow field, air flow field and functional layers of the porous electrodes; (2) heat transfer in all constituent materials; (3) chemical and electrochemical reactions in diffusion and catalyst layers respectively. Facing these issues, the solid and fluid domains are all divided into some discrete meshes. Similar to the works reported by Autissier et al. [130] and Xia et al. [63], we used the commercial CFD tool FLUENT, able to solve the equations of momentum, energy, species and mass continuity for each computational mesh and added sub-routines to implement the following sub-models for the chemical and electrochemical reaction kinetics.

5.3.1. 3D Momentum Transport Equation

To get the equation of motion we write the following form of the momentum balance over each volume element as shown in Figure 5.2 [131]:

$$\begin{bmatrix}\text{Rate of increase}\\ \text{of momentum}\end{bmatrix}=\begin{bmatrix}\text{Rate of}\\ \text{momentum in}\end{bmatrix}-\begin{bmatrix}\text{Rate of}\\ \text{momentum out}\end{bmatrix}+\begin{bmatrix}\text{External force}\\ \text{on the fluid}\end{bmatrix} \quad (5\text{-}1)$$

Equation (5-1) is a vector equation with components in each of the three coordinate directions x, y and z. First we consider the rates of the flows of the x-component of momentum into and out of the volume element shown in Figure 5.2. Convective and molecular transports are two mechanisms for the momentum enters and leaves each volume element; therefore, the rate at which the x-components of momentum enter across the faces by all mechanisms at the position of x, y and Z are $M_{xx}|_{x}\,\Delta y.\Delta z$, $M_{yx}|_{y}\,\Delta z.\Delta x$ and $M_{zx}|_{z}\,\Delta x.\Delta y$. Additionally the rate at which the x-components of momentum leave the faces at $x+\Delta x$, $y+\Delta y$ and $z+\Delta z$ are $M_{xx}|_{x+\Delta x}\,\Delta y.\Delta z$, $M_{yx}|_{y+\Delta y}\Delta z.\Delta x$ and $M_{zx}|_{z+\Delta z}\,\Delta x.\Delta y$ respectively.

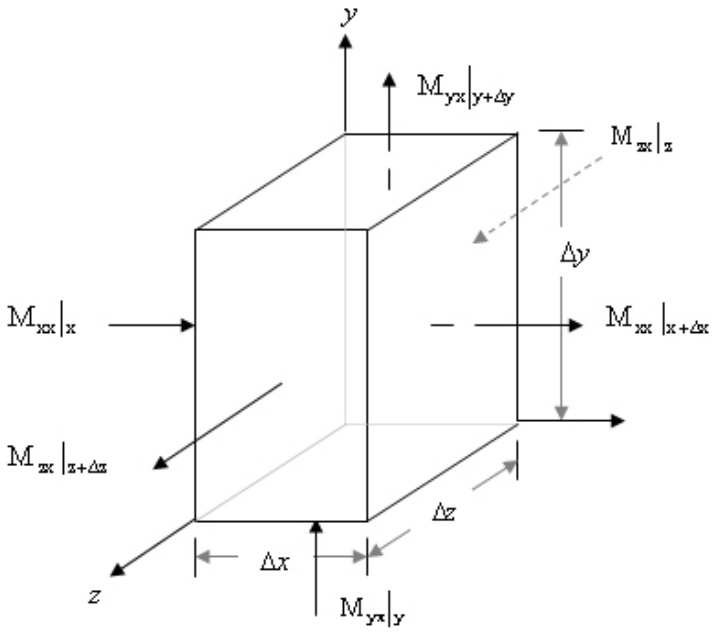

Figure 5.2 - Fixed volume element $\Delta x.\Delta y.\Delta z$, with six arrows indicating the directions of the fluxes of x -momentum through the surfaces by all mechanism[131]

When these contributions are added we get the net rate of addition of x-momentum across all three pairs of faces as follows[131]:

$$\Delta y\Delta z(M_{xx}\big|_{x} - M_{xx}\Big|_{x+\Delta x}) + \Delta z\Delta x(M_{yx}\Big|_{y} - M_{yx}\Big|_{y+\Delta y}) + \Delta x\Delta y(M_{zx}\Big|_{z} - M_{zx}\Big|_{z+\Delta z}) \quad (5\text{-}2)$$

Next there is the external force (typically the gravitational force) acting on the fluid in the volume element. The x-component of this force is:

$$\rho g_x \Delta x.\Delta y.\Delta z \quad (5\text{-}3)$$

Equation (5-2) and (5-3) give the x-components of the three terms on the right side of equation (5-1). The sum of these terms must then be equated to the rate of increase of x-momentum within the volume element ($\Delta x.\Delta y.\Delta z\frac{\partial(\rho\upsilon)}{\partial t}$). When these equations are divided by $\Delta x.\Delta y.\Delta z$and the limit is taken as Δx, Δy and Δz go to zero, the x-component of the momentum balance could result as follows:

$$\frac{\partial}{\partial t}\rho\upsilon = -(\frac{\partial}{\partial x}M_{xx} + \frac{\partial}{\partial y}M_{yx} + \frac{\partial}{\partial z}M_{zx}) + \rho g_x \quad (5\text{-}4)$$

Similar equations can be developed for the y- and z-components of the momentum balance:

$$\frac{\partial}{\partial t}\rho v = -(\frac{\partial}{\partial x}M_{xy} + \frac{\partial}{\partial y}M_{yy} + \frac{\partial}{\partial z}M_{zy}) + \rho g_y \quad (5\text{-}5)$$

$$\frac{\partial}{\partial t}\rho w = -(\frac{\partial}{\partial x}M_{xz} + \frac{\partial}{\partial y}M_{yz} + \frac{\partial}{\partial z}M_{zz}) + \rho g_z \quad (5\text{-}6)$$

By using the vector-tensor notation and when the above x-, y- and z-components of the momentum equation are added together, we get the following differential statement of the conservation of momentum.

$$\frac{\partial}{\partial t}\rho\vec{u} = -[\nabla.M] + \rho g \quad (5\text{-}7)$$

Expanding the combined momentum flux tensor M to the convective momentum flux ($\rho\vec{u}\vec{u}$), and the molecular momentum flux ($p+(\tau)$), we get the following equation of motion:

$$\frac{\partial(\rho\vec{u})}{\partial t}+\nabla(\rho\vec{u}\vec{u})=-\nabla P-\nabla(\tau)+\rho g \tag{5-8}$$

Inclusion of the additional source term S_M, allows the equation of motion to be valid for both the porous media and the fuel gas channels; on the other hand, for the mathematical description of the fluid flow in porous media, the equation of motion can be used with an additional source term which is composed of two parts: a viscous loss term and an inertial loss term; therefore, for a simple homogeneous porous media it can be written as follows [130]:

$$S_M=-(\frac{\mu}{\alpha_p}\vec{u}+C\frac{1}{2}\rho\vec{u}\vec{u}) \tag{5-9}$$

Here α_p is the permeability and C is the inertial resistance factor. In laminar flows through porous media, the pressure drop proportional to velocity and the constant C can be considered to be zero and the non-zero source term can be regarded as a generalized Darcy's model[64, 70, 124].

$$S_M=-\frac{\mu}{\alpha_p}\vec{u} \tag{5-10}$$

$$\alpha_p=\frac{\varepsilon^3 d_p^2}{72\iota(1-\varepsilon)^2} \tag{5-11}$$

5.3.2. 3D Heat Transport Equation

It is known that the temperature distribution in SOFC strongly influences the cell performance. Also many properties of gases and the SOFC's components are strongly temperature dependent; therefore, it is vital to develop a heat transport

model for various heat effects in all computational domains. The energy conservation on the volume element $\Delta x.\Delta y.\Delta z$ can be written as follows[123, 131]:

$$\begin{bmatrix}\text{Rate of change}\\ \text{of energy within}\\ \text{the volume element}\end{bmatrix}=\begin{bmatrix}\text{Net rate of}\\ \text{energy transfer}\\ \text{by convection}\end{bmatrix}+\begin{bmatrix}\text{Net rate of energy}\\ \text{transfer by conduction}\\ \text{and diffusion}\end{bmatrix}+\begin{bmatrix}\text{Net rate of energy}\\ \text{from the work done}\\ \text{on volume element}\end{bmatrix}+\begin{bmatrix}\text{Net rate of energy}\\ \text{from the reaction}\\ \text{in volume element}\end{bmatrix} \quad (5\text{-}12)$$

The total rate of energy from the work done on unit volume of $\Delta x.\Delta y.\Delta z$ and by all the surface forces is given as follows[123, 131]:

$$\left(\left[-\frac{\partial(\upsilon P)}{\partial x}-\frac{\partial(\nu P)}{\partial x}-\frac{\partial(wP)}{\partial z}\right]+\left[\begin{array}{l}\dfrac{\partial(\upsilon\tau_{xx})}{\partial x}+\dfrac{\partial(\upsilon\tau_{yx})}{\partial y}+\dfrac{\partial(\upsilon\tau_{zx})}{\partial z}+\dfrac{\partial(\nu\tau_{xy})}{\partial y}+\\ \dfrac{\partial(\nu\tau_{yy})}{\partial y}+\dfrac{\partial(\nu\tau_{zy})}{\partial z}+\dfrac{\partial(w\tau_{xz})}{\partial z}+\dfrac{\partial(w\tau_{yz})}{\partial z}+\dfrac{\partial(w\tau_{zz})}{\partial z}\end{array}\right]\right).\Delta x.\Delta y.\Delta z \quad (5\text{-}13)$$

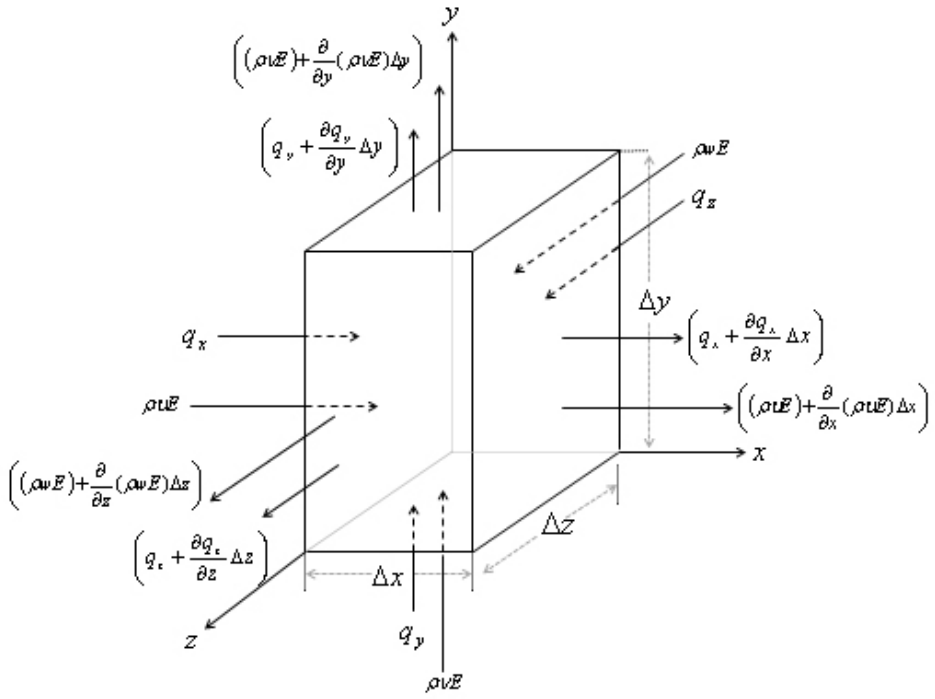

Figure 5.3 - Fixed volume element $\Delta x.\Delta y.\Delta z$ with heat flux vectors through all surfaces [131]

Figure 5.3 shows the x -, y - and z -components of the heat flux vector. For the mixture, the heat flux q is given as the combined effects of the heat conduction

and inner-diffusion; therefore, the net rate of heat transports to the volume element $\Delta x.\Delta y.\Delta z$ and along the x-direction is given as follows:

$$-(\frac{\partial q_x}{\partial x}+\frac{\partial(\rho \upsilon E)}{\partial x})\Delta x.\Delta y.\Delta z \tag{5-14}$$

Similarly, the net rates of heat transfer to the volume element $\Delta x.\Delta y.\Delta z$ along the y- and z-directions are:

$$-(\frac{\partial q_y}{\partial y}+\frac{\partial(\rho vE)}{\partial y})\Delta x.\Delta y.\Delta z \tag{5-15}$$

$$-(\frac{\partial q_z}{\partial z}+\frac{\partial(\rho wE)}{\partial z})\Delta x.\Delta y.\Delta z \tag{5-16}$$

In addition to the above, there is another heat source term $S_h \Delta x \Delta y \Delta z$ that may come from the reaction in the volume element. By using the vector-tensor notation, the sum of Eq. (5-13) to (5-16) and the reaction heat source term must then be equated to the rate of energy changes within the volume element $\Delta x.\Delta y.\Delta z$. When these equations are divided by $\Delta x.\Delta y.\Delta z$ and the limit is taken as $\Delta x, \Delta y$, and Δz goes to zero, the following expression will result[131]:

$$\frac{\partial(\rho E)}{\partial t}=-\nabla.(\vec{u}(\rho E+p))-\nabla(q)+\nabla(\tau.\vec{u})+S_h \tag{5-17}$$

Fourier's law of heat conduction relates the heat flux to the local temperature gradient. Therefore, with attention to the inner diffusion, the net heat flux q, can be considered as follows[131]:

$$q=(-k.\nabla(T)+\sum_{i=1}^{m} h_i J_i) \tag{5-18}$$

Substituting Eq. (5-18) into Eq. (5-17) leads to the equation of energy as follows:

$$\frac{\partial(\rho E)}{\partial t} + \nabla.(\vec{u}(\rho E + P)) = \nabla.(k.\nabla(T) - \sum_i h_i J_i + (\tau.\vec{u})) + S_h \quad (5\text{-}19)$$

Here k is the conductivity, and J_i is the diffusion flux of species *i*. The first three terms on the right hand side of equation (5-19) represents energy transfer due to conduction, species diffusion and viscous dissipation, respectively. As it was mentioned S_h, includes the heat of electro-chemical reactions and any other heat sources we have defined (the units of all source terms are of the form of generated rate per volume).In porous media regions, the equation of energy is solved with modifications to the conduction flux and the transient terms as follows[132]:

$$\frac{\partial}{\partial t}(\varepsilon\rho^f E^f + (1-\varepsilon)\rho^s E^s) + \nabla.(v(\rho^f E^f + P)) = \nabla[k^{eff}\,\mathrm{grad}(T) - (\sum_i h_i J_i) + (\tau.\vec{u})] + S_h \quad (5\text{-}20)$$

Where E^f - total fluid energy, E^s-total solid energy, ε- porosity of the medium, k^{eff} - effective thermal conductivity of the medium that is given by [132]:

$$k^{eff} = \varepsilon k^f + (1-\varepsilon)k^s \quad (5\text{-}21)$$

The properties for different solid components of the cell can be found from literatures as shown in Table 5.2.

Table 5.2 - Property parameters for different solid components of the cell[63]

Components	k^s **($Wm^{-1}K^{-1}$)**	ρ^s **($Kg.m^{-3}$)**	c_p **($KJ.Kg^{-1}.K^{-1}$)**
Anode	6.23	7000	0.65
Cathode	9.6	5620	0.9
Electrolyte	2.7	5560	0.3
Interconnect	13	7700	0.8

5.3.3. 3D Mass Transport Equation

Figure 5.4 shows a volume element $\Delta x.\Delta y.\Delta z$ fixed in space, through which the fluid mixture is flowing. Generally, within this volume, reactions among the various chemical species could occur, and we use the symbol S_i^r to indicate the rate at which species *i* is produced or consumed (component mass source term). The law of conservation of mass for each species *i* in a mixture of m components is written as follows [131]:

$$\begin{bmatrix}\text{Rate of increase/decrease}\\ \text{of component i}\\ \text{in the volume element}\end{bmatrix}=\begin{bmatrix}\text{Rate of addition}\\ \text{of mass across}\\ \text{faces}\end{bmatrix}-\begin{bmatrix}\text{Rate of removal}\\ \text{of mass across}\\ \text{faces}\end{bmatrix}+\begin{bmatrix}\text{Rate of production /}\\ \text{consumption}\\ \text{of mass by}\\ \text{chemical reaction}\end{bmatrix} \quad (5\text{-}22)$$

When the entire mass balance is written down and divided by $\Delta x.\Delta y.\Delta z$, one obtained after letting the size of the volume element decrease to zero:

$$\frac{\partial \rho_i}{\partial t} = -\left(\frac{\partial n_{ix}}{\partial x} + \frac{\partial n_{iy}}{\partial y} + \frac{\partial n_{iz}}{\partial z}\right) + M_{w,i}.S_i^r \quad (5\text{-}23)$$

In Eq. (5-23) the quantities n_{ix}, n_{iy} and n_{iz} are the Cartesian components of the mass flux vector with the combined diffusive and the convective fluxes as follows.

$$n_i = M_{w,i}J_i + \rho_i\vec{u} \quad (5.24)$$

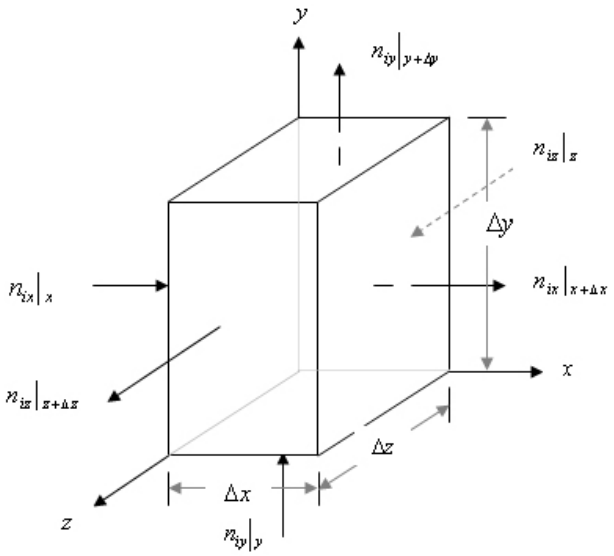

Figure 5.4 - Fixed volume element $\Delta x\Delta y\Delta z$, with mass fluxes through all surfaces by all mechanisms[131]

Substituting Eq. (5.24) and using the vector-tensor notation, Eq. (5-23) may be rewritten as the equation of continuity for species i in a multi-component reacting mixture as follows:

$$\frac{\partial \rho_i}{\partial t} = -(\nabla . \rho_i \vec{u}) - M_{w,i}(\nabla . J_i + (S_i^r)_{overal}) \qquad i = 1,2,3,...m \tag{5-25}$$

Addition of the continuity equations for all m species, with respect to mass average velocity $\sum_{i=1}^{m} J_i = 0$, and the conservation of total mass $\sum_{i=1}^{m} (S_i^r)_{overal} = 0$, leads to the equation of continuity for the mixture as follows:

$$\frac{\partial \rho}{\partial t} = -(\nabla . \rho \upsilon) \tag{5-26}$$

In equation (5-25), J_i represents the diffusive flux of each component i that is given by the following correlation.

$$J_i = -\sum \nabla (C_i D_i^{eff}) - D_i^T \frac{\nabla T}{T} \tag{5-27}$$

In the above equation, D_i^{eff} is the effective diffusion of the reactants (please see Appendix A) and D_i^T represents thermal diffusivity. In addition, the overall component mass source term is given by:

$$(S_i^r)_{overal} = \sum_{\ell=1}^{N_R} (S_i^r)^{\ell} \tag{5-28}$$

Here, N_R is the number of reactions that component i is involved in and $(S_i^r)^{\ell}$ is the component consumption or production rate relevant to each reaction ℓ.

5.3.4. Reaction kinetics

5.3.4.1. Chemical Reactions

Three dimensional simulation involving a complete set of elementary reactions would be difficult to converge and will be computationally expensive[133]; therefore, in this study we considered the overall steam reforming and water gas shift reactions as follows:

$$CH_4 + H_2O \rightarrow 3H_2 + CO \quad (5\text{-}29)$$

$$H_2O + CO \rightarrow H_2 + CO_2 \quad (5\text{-}30)$$

Reforming reaction occurs in the porous anode diffusion layer. Although some models assume a simplified approach of thermodynamic equilibrium [134, 135], a more correct model of the reforming reaction rate is based on the kinetic approach [136]. Several kinetic expressions considering the steam reforming reaction were developed in the literature but specific literature on steam reforming in the presence of typical Ni/YSZ anode material [137, 138]suggest the use of the following general expression to evaluate the reforming reaction rate.

$$R_r^{SMR} = \kappa^{SMR}.p_{CH_4}^{\beta 1}.p_{H_2O}^{\beta 2}.\exp(-\frac{E_{act}}{R.T}) \quad (5\text{-}31)$$

Reaction rate constant (κ^{SMR}), activation energy (E_{act}) and the reaction orders ($\beta 1 \text{and} \beta 2$) vary between the models and rely strongly on the physical and chemical properties of the anode material [139]. Thus, if accuracy is sought, experimental data have to be collected in order to determine realistic values of these factors. In view of this, to compare the effects of different reforming models on predicted results, data from the open literature have been used; in particular the works by Ahmed and Foger [138], Haberman and Young [140] and Achenbach [137], as shown in Table 5.3.

For the water-gas shift reaction different approaches can be found in literature: global reaction mechanism that considers reaction in the anode only [141, 142], global reaction mechanism that considers reaction in the anode and in the fuel gas channels [76, 143] and a more advanced reaction mechanism that includes catalytic surface reaction kinetics for steam reforming, water-gas shift reaction and the Boudouard mechanism [144]. In this work, water gas shift reaction is considered in

both anode electrode and fuel gas channels that is expressed with an equilibrium limited rate expression [140].

$$(S^{r})^{WGS} = \kappa_{f}^{WGS}(p_{H_2O}p_{CO} - \frac{p_{H_2}p_{CO_2}}{k_{eq}^{WGS}}) \quad (5\text{-}32)$$

In the above equation, temperature dependent expression for κ_{f}^{WGS} was deduced from Arrhenius fit of Lehnert's data [145] and the equilibrium constant κ_{eq}^{WGS} was taken from the literature [146].

$$\kappa_{f}^{WGS} = 0.0171\exp(-\frac{103191}{RT}) \quad (5\text{-}33)$$

$$\kappa_{eq}^{WGS} = 1.767 \times 10^{-2}\exp(4400/T) \quad (5\text{-}34)$$

The molar rates of formation of different gas species from the catalytic chemical reactions can be formulated as follows[36]:

$$(S_{CH_4}^{r})^{Chem} = -A_s.R_r^{SMR} \quad (5\text{-}35)$$

$$(S_{CO}^{r})^{Chem} = A_s.R_r^{SMR} - (S^{r})^{WGS} \quad (5\text{-}36)$$

$$(S_{H_2O}^{r})^{Chem} = -A_s.R_r^{SMR} - (S^{r})^{WGS} \quad (5\text{-}37)$$

$$(S_{H_2}^{r})^{Chem} = 3A_s.R_r^{SMR} + (S^{r})^{WGS} \quad (5\text{-}38)$$

$$(S_{CO_2}^{r})^{Chem} = (S^{r})^{WGS} \quad (5\text{-}39)$$

In addition, with respect to the low amount of energy released from the water gas shift reaction, extra heat from the air flow and electrochemical reactions can effectively promote the reforming reaction rate [147]. However, the heat source from the reforming and water gas shift reactions is calculated by the following expressions [61, 127].

$$S_h^{Chem} = -\sum_i h_i(S_i^{r})^{Chem} \quad (5\text{-}40)$$

$$h_i = \int_{T^0}^{T} c_{p,i}\,dT + h_i(T^0) \tag{5-41}$$

$$c_p = \sum_{k=0}^{6} a_k \left(\frac{T}{1000}\right)^k \tag{5-42}$$

Here the values of isobaric molecular heat capacity coefficients, a_k and standard enthalpy of formation, $h_i(T^0)$ are taken from literature [128].

Table 5.3 - Three different models for the methane reforming kinetics

	Authors	Model	Reaction rate constants	E_{act}
SMR-1	Ahmed and Foger	$R_r^{SMR} = \kappa.P_{CH_4}^{0.85}.P_{H_2O}^{-0.35}$	$\kappa = 27.02.\exp(-\frac{E_{act}}{RT})[\frac{mol}{m^2.Pa^{0.5}.s}]$	95000
SMR-2	Achenbach	$R_r^{SMR} = \kappa.P_{CH_4}$	$\kappa = 0.04247.\exp(-\frac{E_{act}}{RT})[\frac{mol}{m^2.Pa.s}]$	82000
SMR-3	Haberman and Young	$(S^r)^{SMR} = \kappa_f^{SMR}(P_{CH_4}P_{H_2O} - \frac{P_{H_2}^3 P_{CO}}{\kappa_{eq}^{SMR}})$	$\kappa_f^{SMR} = 2395.\exp(-\frac{E_{act}}{RT})[\frac{mol}{m^3.Pa^2.s}]$	231266

5.3.4.2. Electrochemical Reaction

The electrochemical reaction occurs at TPB, which often is treated as the mathematical surface or interface boundary condition [148]. However, it is widely reported in the open literature that the electrochemical reaction not only occurs on the electrode-electrolyte interface but also extended to a distance of 10-50 µm from the solid electrolyte[36, 149-151].In the model geometry of this work, TPBs or the electrode catalyst layers were treated as the finite volumes with thickness of 30 µm. However, to reduce the computational time and the model complexity, the electrode catalyst layers were divided into a number of control volumes arranged in a single layer grid. In this way, assuming the electrolyte as the sole contributor to the ohmic losses, the equivalent circuit approach was used to solve the electrochemical sub-model together with all transport equations within the catalyst layers and the effect of the electrochemical reaction rate was taken into account

through the heat and mass source terms of the conservation equations. Additionally, as it was shown in chapter 3, under the steady state operating conditions, Faradic and electrolyte current densities have the identical values equal to the cell current density. Therefore, to simplify the electrochemical sub model, the Faradic current is replaced with the cell current density, which is used for calculating the heat and mass source terms of the conservation equations at catalyst layers [63, 64].

$$R^{elec}_{r,H_2} = \frac{\nu_{H_2}.i_{cell}}{2F} \tag{5-43}$$

$$R^{elec}_{r,H_2O} = \frac{\nu_{H_2O}.i_{cell}}{2F} \tag{5-44}$$

$$R^{elec}_{r,O_2} = \frac{\nu_{O_2}.i_{cell}}{4F} \tag{5-45}$$

Furthermore, under the effects of the electrochemical reaction, the rate of the heat generation is specified as the electrochemical heat source and can be determined as follows [152].

$$R^{elec}_{h} = i_{cell}\left(\frac{\Delta H^{elec}}{2F} - E_{cell}\right) \tag{5-46}$$

Here, ΔH^{elec} is the enthalpy of the electrochemical reactions and E_{cell} is the cell voltage as it was presented in Eq. (3-28). In addition, the reversible electrode potentials are calculated from Eq. (3-37) to (3-38). However, considering the charge transfer coefficients equal to 0.5, activation overpotentials are calculated by inverting Butler-Volmer equations as the similar approach has been suggested by Xia et al. [63].

$$\eta^{A/C}_{act} = \frac{2RT}{n_e F}\sinh^{-1}\left(\frac{i_{cell}}{2i^{A/C}_0}\right) \tag{5-47}$$

In this study, the best fit for the values of the exchange current densities at the anode and cathode ($i^{A/C}_0$) are 3800 and 1800 A/m^2 respectively. Moreover, due to high conductivities of the electrodes, the resistance offered by the anode and

cathode materials are negligible compared to the electrolyte resistance in modern cells [64]. Therefore, to calculate the Ohmic overpotential, only the resistance of the electrolyte is considered. Furthermore, the equilibrium potential steps and activation overpotentials are calculated from temperature and species molar fractions at the catalyst layers and then, there is no need for the explicit evaluation of the concentration overpotentials [70]. In addition, considering the air flow, oxygen is in excess so that its partial pressure could be considered constant in gas channels [61, 132]. In view of this, using the approach, which has been suggested by Danilov and Tade [61], the flux boundary condition similar to equation (3-39) estimates the oxygen molar fraction of the catalyst layer and reduction in model complexity can be achieved. Finally, as it was mentioned above, in FLUENT the units of all source terms are of the form of generation or consumption rate per volume. Therefore, due to the units of the reaction rates, they should be multiplied by the specific surface that is defined as the reactive surface area per unit volume of the particulate reactive domain. Assume that the reactive porous media can be modelled as a binary mixture of the monotonic spherical electrode and electrolyte particles, the statistical properties including the mean particle diameter d_p, the pore radius r_p, and specific surface area A_s can be estimated as follows [99]:

$$\frac{1}{d_p} = \frac{\Psi_{elde}}{2r_{elde}} + \frac{\Psi_{elyt}}{2r_{elyt}} \tag{5-48}$$

$$r_p = \frac{\varepsilon d_p}{3(1-\varepsilon)} \tag{5-49}$$

$$A_s = \frac{6\lambda_s(1-\varepsilon)}{d_p} \tag{5-50}$$

In the above equations, Ψ_{elde} and Ψ_{elyt} are the electrode and electrolyte volume fractions in the anode porous media respectively; r_{elde} and r_{elyt} are the radius of the electrode and electrolyte particles correspondingly and λ_s is an effective factor of the particulate reactive volume that cannot be calculated simply on the basis of the properties of the pure materials. For the porous catalyst layers, the specific surface area is defined as the contact area between connected electrode and electrolyte

particles per unit of the reactive volume. Therefore, the effective factor can be estimated from the coordinate number theory and percolation theory, and based on that the contact specific surface area is given by the following expression as it was originally developed by Costamagna et al. [33].

$$A_s^{contact} = \pi \sin^2\theta . r_{elde}^2 n_t n_{elde} n_{elyt} \frac{Z_{elde} Z_{elyt}}{Z} P_{elde} P_{elyt} \tag{5-51}$$

Here, θ is the contact angle between the electrode and electrolyte particles in the reactive volume; n_t is the total number of particles per unit of the reactive volume; n_{elde} and n_{elyt} are the number fractions of the electrode and electrolyte particles in the reactive volume respectively; Z_{elde} and Z_{elyt} are the coordination numbers of the electrode and electrolyte; P_{elde} and P_{elyt} are the probabilities of the electrode and electrolyte particles and finally Z is the total average coordination number, equal to 6. All these parameters can be calculated from the work of Hussain and Dincer [150] and given as follows:

$$n_t = \frac{1-\varepsilon}{(4/3)\pi r_{elde}^3 \left[n_{elde} + (1-n_{elde})(r_{elyt}/r_{elde})^3 \right]} \tag{5-52}$$

$$n_{elde} = \frac{\psi_{elde}}{\left[\psi_{elde} + \left((1-\psi_{elde})/(r_{elde}/r_{elyt})^3 \right) \right]} \tag{5-53}$$

$$Z_{elde} = 3 + \frac{Z-3}{\left[n_{elde} + (1-n_{elde})(r_{elyt}/r_{elde})^2 \right]} \tag{5-54}$$

$$Z_{elyt} = 3 + \frac{(Z-3)(r_{elyt}/r_{elde})^2}{\left[n_{elde} + (1-n_{elde})(r_{elyt}/r_{elde})^2 \right]} \tag{5-55}$$

$$P_{elde} = \left[1 - (2 - \frac{Z_{elde-elde}}{2})^{2.5} \right]^{0.4} \tag{5-56}$$

$$P_{elyt} = \left[1 - (2 - \frac{Z_{elyt-elyt}}{2})^{2.5} \right]^{0.4} \tag{5-57}$$

$$Z_{elde-elde} = \frac{n_{elde} Z_{elde}^2}{Z} \tag{5-58}$$

$$Z_{elyt-elyt} = \frac{n_{elyt} Z_{elyt}^2}{Z} \quad (5\text{-}59)$$

With respect to the reforming reaction in the anode diffusion layer, the specific surface is defined as the total area exposed by the particles to the gas phase per unit of the reactive volume. In view of this and for the initial clean bed of the porous media with monotonic rigid particles of the same size, the effective factor of the reactive volume is equal to unity [153]. However, due to the contact angle of 15° between the electrode and electrolyte particles, the overlapping regions (contact specific area) should be reduced from the total surface of the rigid particles and the exposed specific surface can be estimated as follows:

$$A_s^{rigid} = \frac{6(1-\varepsilon)}{d_p} \quad (5\text{-}60)$$

$$A_s^{expose} = A_S^{rigid} - A_s^{contact} \quad (5\text{-}61)$$

However, as reported by Bertei and Nicolella [154], neglecting the fraction of the surface lost in contacts, the exposed surface area is overestimated in the order of 11.4% in the worst case for a binary mixture of the mono sized particles.

5.4. Numerical Approach in 3D CFD Model

To investigate the combined effects of the anode flow field design and micro-structural parameters of the anode diffusion layer, a general frame work based on the computational fluid dynamic (CFD) approach was applied to solve all the governing equations. CFD is the art of replacing the integral or derivative forms of the fundamental physical principles of the fluid dynamics with discretised algebraic forms, which in turn are solved to obtain numbers for the flow field values at discrete points in time and/or space [123]. There are several commercial packages for CFD analysis; however, in this work all the governing equations were solved in ANSYS (version 13.0) using the FLUENT solver, which is a control volume based technique to convert differential equations to algebraic ones that can be solved numerically. In this technique we divide the computational domain into a number of smaller, non-overlapping sub domains that means a grid (or mesh) of cells (or control volumes) [123]. In view of this, gradients are needed not only for calculating

values of a scalar at the cell faces, but also for computing diffusion terms and velocity derivatives. Considering the computational time and solution algorithm, Green-Gauss Cell Based method [127] is selected for calculating the gradients. In addition, 2nd order up-wind discretization scheme[123] is selected for the convection terms of each governing equation. For the iterative calculation of the pressure and velocity, FLUENT provides different algorithms; however, in this model, pressure and velocity were coupled using SIMPLE method for implicit time treatment of the flow variables [123, 127]. For the other scalars, which are coupled to the momentum equation, the calculations are done sequentially. Therefore, all transport equations are solved using the commercial FLUENT solver; however, it is linked with a user defined function (UDF) programmed by VC++ for implementing chemical and electrochemical reaction rates and source terms of the conservation equations. For each iteration, local species concentration and temperature are accessed from the solver.

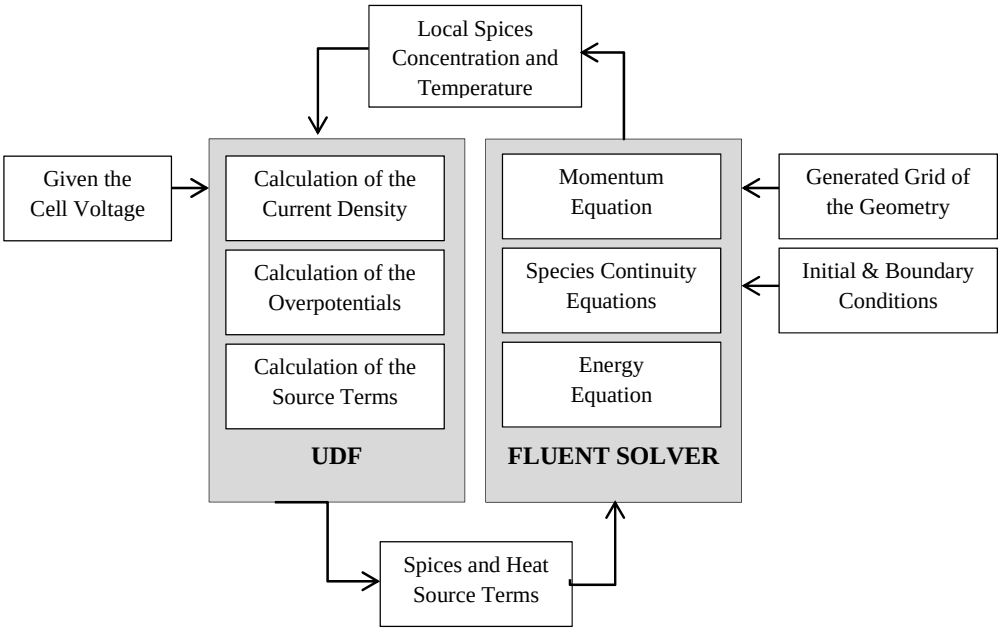

Figure 5.5 - Flowchart of the solution technique for 3D CFD model

Figures 5.5 and 5.6 present the flowchart of the solution technique and the sequence of the SIMPLE method respectively. However, to distinguish between the influences of the purely flow field design, catalytic reforming reaction rate, heat effects from the air flow and the electrochemical reaction rate on pressure, velocity,

temperature and species concentration profiles, simulation was performed for three different cases, which are listed in Table 5.4.

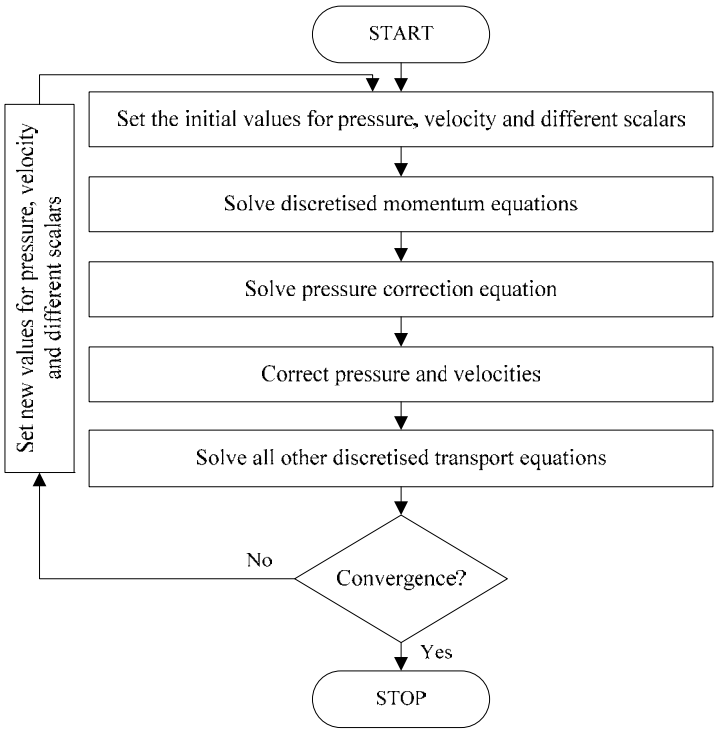

Figure 5.6 - The SIMPLE algorithm[123]

Table 5.4 - Aims for different simulation cases

Case No.	**Aims**
1	Analysis of pressure and velocity profiles for different flow field designs (Design A, B & C)
2	Analysis of the combined effects of geometrical factors, micro-structural parameters and catalytic chemical reactions on temperature and species concentration distributions (Design B)
3	Expansion of case 2 to include heat effects of the air flow and electrochemical reaction rate (Design B)

5.5. Initial and Boundary Conditions in 3D CFD Model

To initialize the numerical solution, we patch different values of the velocities, temperature and species concentration into different computational domains. Therefore, for the fuel and air gas channels and electrode porous media, different flow variables were initialized relevant to their inlet values specified at fuel and air inlet manifolds. For the solid electrolyte, which is impermeable to the reactants, initial values for the species concentration were set to zero and temperature can be set as the values from the fuel or air inlet condition. The inlet operating conditions and parameters used for the developed model can be found in Tables 5.5 and 5.6, respectively.

Table 5.5 - Operating conditions for planar SOFC in 3D CFD model

Parameters	**Anode side**	**Cathode side**
Pressure	1 bar	1 bar
Temperature	1023K	1023K
CH4 % mole	25.66	---
H2 % mole	15.31	---
CO2 % mole	5.08	---
CO % mole	0.098	---
H2O % mole	53.47	---
N2 % mole	0.38	79
O2 % mole	0	21
Fuel Flow	0.067 SLM (Dry gas) 0.073 SLM (Steam)	---
Air Flow	---	0.8 SLM

However, in order to complete the model formulation of an SOFC, boundary conditions at different locations are required. Further, due to interdependent

transport processes in different components of an SOFC, the definition of boundary conditions involved both external and internal boundaries [150].The locations of different internal and external boundaries are illustrated in Figure 5.7.Furthermore, for each case, the boundaries relevant to the involved computational domains are summarized in Table 5.7. The external inlet boundaries (BC1, BC2, BC6), are set as the values for the inlet operating conditions and specified as the mass flow inlet to match the prescribed mass flow rates. At the outlet manifolds (BC3 and BC7), the pressure outlet boundary condition is adopted. Furthermore, as it is shown in Figure 5.7, for all cases, the computational domains only includes the land portion of interconnect; therefore, at external boundaries BC10 and BC16, thermal insulation and impermeable condition for the species transport are specified. Considering the simulation results for design B, which will be shown later, there are symmetrical pressure and velocity profiles for the half layer arrays of two adjacent cells. Therefore, to speed up the computational time, for cases 2 and 3, we specified the symmetrical conditions at the boundaries BC4, BC5, BC8 and BC9.

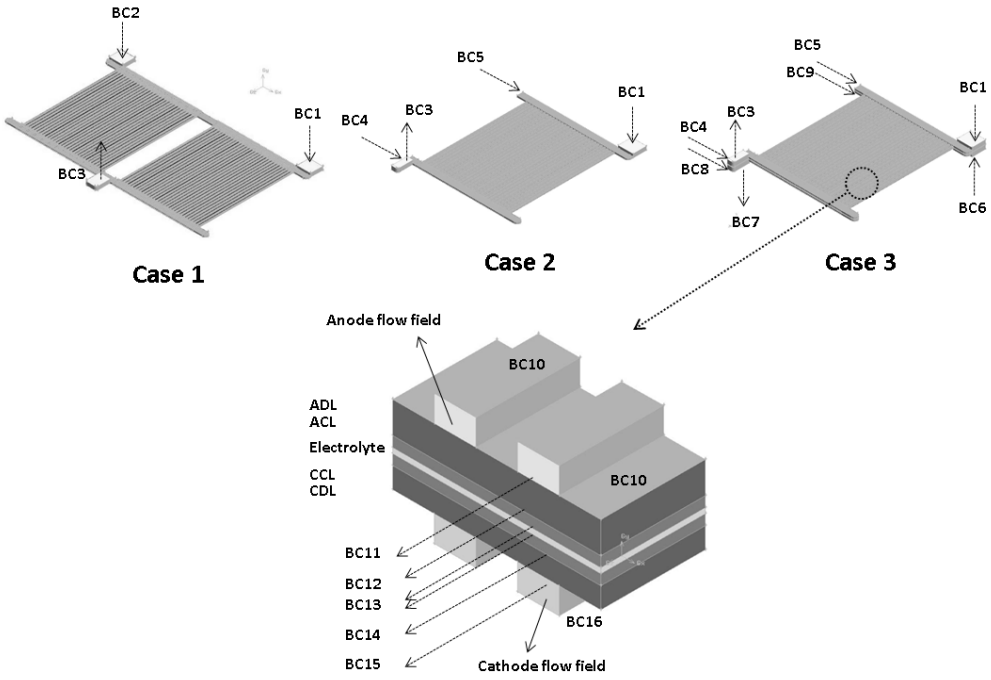

Figure 5.7 - Illustration of locations at which boundary conditions are required in CFD model and for different cases

With respect to the internal boundaries, BC11 and BC15 represent the interfaces between the gas channels and electrode diffusion layers. However, for case 1, diffusion layers are not considered and then these two boundaries are specified as the impermeable wall with thermal insulating condition. For other cases, electrode functional layers are set for the porous media; therefore, the internal boundaries including BC11, BC12, BC14 and BC15 are specified as the interior faces which allows coupling the momentum, energy and species transfer equations. In view of that, varying boundary conditions for different operating variables are specified at these internal boundaries. Finally, with respect to the boundaries between the electrodes and electrolyte (BC13), the adjacent computational domains are coupled to account for the heat effects and zero species diffusion fluxes are specified on these stationary boundaries.

Table 5.4 - Input parameters for 3D CFD model[32, 150]

Thickness of the node and cathode catalyst layers, (μm)	30
Thickness of the electrolyte, (μm)	10
Dimension of different flow field design	According to CFCL layouts (AD 0903 - 18/02/2009)
Porosity of the anode and cathode catalyst layers	0.4
Pore size of the anode and cathode catalyst layers, (μm)	2.0
Volume fractions of the electrode and electrolyte	0.5
Contact angle between electrode/electrolyte particles,(˚)	15

5.1. Simulation Results and Discussion

In this section, grid analysis and model predictions are evaluated first. Additionally, simulation results of case 1 for the effects of various flow field designs on pressure and velocity profiles are discussed. Finally, with respect to the importance of the electrode engineering, simulation results of cases two and three are evaluated for different structural parameters of the anode diffusion layer to predict the true

contribution of the geometrical factors, micro-structural parameters and catalytic reaction rates on spatial distribution of different parameters.

Table 5.5 - Computational domains and involved boundaries for different cases

Case No.	Computational domains	Internal boundaries	External boundaries
1	Fuel gas flow fields for two cells of a layer (design A, B & C)	N/A	BC1, BC2, BC3, BC10, BC11
2	Fuel gas flow field for a single cell of design B with ADL	BC11	BC1, BC3, BC4, BC5, BC5, BC10, BC12
3	Complete cell of design B including fuel flow field, ADL, ACL, Electrolyte, CCL, CDL and air flow field	BC11 ~ BC15	BC1, BC3, BC4, BC5, BC8, BC9, BC6, BC7, BC10, BC16

5.6.1. Grid Sensitivity Analysis

Two aspects that characterise a successful CFD simulation results are convergence and grid independency. For the converged solution, the residual convergence was limited to 10^{-6} for all variables. However, we need to be sure that the solution no longer changes with more iteration. This can be resolved by the transient solution of a dynamic system even then the change in the residuals during the iteration is not much.

For the grid-independent analysis, which is an essential part of any CFD studies, there is no formal way of estimating the errors introduced by inadequate grid design. Thus, the only way to eliminate errors due to coarseness of a grid is a procedure of successive refinement of an initially coarse grid until certain key results do not change [123]. Although the larger the number of cells, the better the solution accuracy and the cost in terms of necessary computer hardware and calculation time are dependent on the fineness of the grid. In view of this, to

confirm that the grid density used in this study was detailed enough, the simulation of case two, which accounts for the effects of the catalytic reforming reaction based on the kinetic model developed by Ahmed and Foger [138] was repeated for different grid sizes.

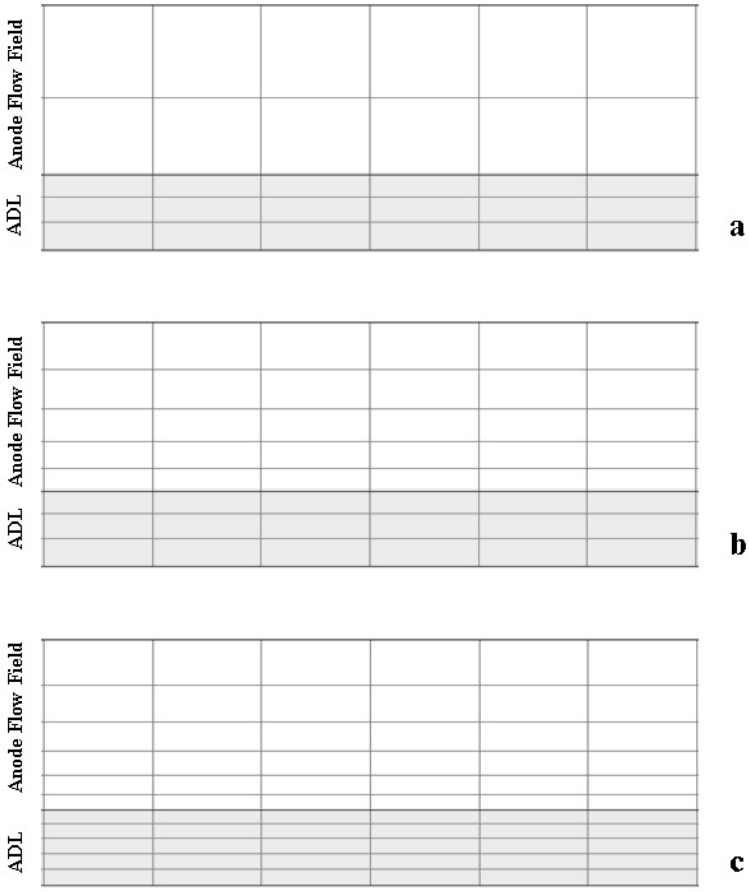

Figure 5.8 - Sample grids used for simulation of case 2; a) Grid density of 323898 cells; b) Grid density of 470490 cells; c) Grid density of 647698 cells

The sample grids used for a portion of the computational domains of case 2 are shown in Figure 5.8. For the sample grid with 323898 cells, the grid is uniform in anode flow field but non-uniform in ADL. However, with respect to the catalytic chemical reactions in ADL, the optimum mesh is expected to be non-uniform within both layers of the computational domains. Therefore, for each specific domain and with attention to the aspect ratio, the mesh size is finer in areas where large variations occur and coarser in regions with relatively little change. Figures5.8 (b) and (c) are the grid samples of totally non-uniform mesh with different densities of 470490 and 647698 cells respectively.

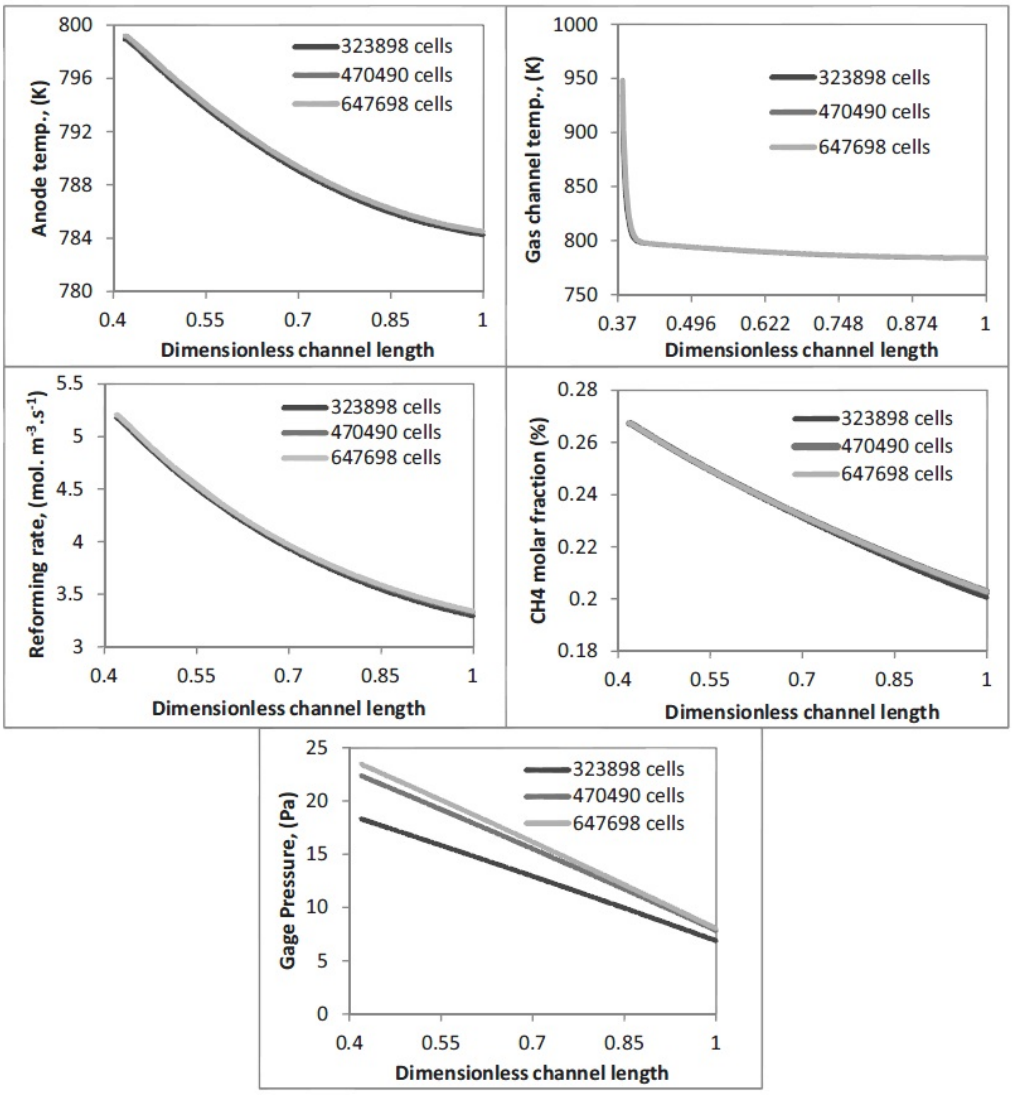

Figure 5.9 - Effects of grid density on predicted results for the key parameters of case 2 along the length of the cell with porosity of 0.4 and pore size of 4.4 µm

In addition, Figure 5.9 shows the comparison of the simulation results for the fine and coarser grids. It can be seen, that the reforming rate and temperature of the electrode and fuel gas channels are affected insignificantly by the grid refinement. However, pressure profiles reveal that the numerical solution is slightly affected by the grid density. Thus, for further analysis and with respect to the computational time, the grid density of 470490 cells is detailed enough to analyse reactions and transport phenomena within the anode diffusion layer and was extendable for case 3 as well.

5.6.2. Evaluation of the Results from 3D CFD Model

To assess the model predictions, the simulation results are evaluated for two different cases (case2 and case 3). Table 5.8 shows the evaluation of 3D simulation results of case 2 obtained from the Ahmed kinetic reforming model by comparison with thermodynamic equilibrium data, simulation results from CFCL 1D model and two other reforming kinetic models presented in Table 5.3.

Table 5.6 - Evaluation for 3D simulation results from case 2

	Thermodynamic Equilibrium based on Gibbs free energy minimization	**CFCL 1D model, Ahmed kinetics (SMR – 1)**	**3D model, Ahmed kinetics (SMR – 1)**	**3D model, Achenbach kinetics (SMR – 2)**	**3D model, Haberman (SMR – 3)**
Outlet CH4 molar fraction (%)	0.1789	0.1890	0.2033	0.1929	0.2201
Outlet H2 molar fraction (%)	0.3037	0.2807	0.2147	0.2342	0.1917
Outlet Temp. (K)	749	737	786	723	851
CH4 Conversion	32%	30%	24.7%	28.6%	18.6%

Although both 1D and 3D models closely approach thermodynamic equilibrium, the 3D simulation shows that flow distribution effects that result from the geometrical design factors (manifold and channel design) and the finite external mass transfer within the gas distribution channels lead to a lower percentage of methane conversion. In other words the 1D model somewhat over-predicts conversion that would be achieved in a real geometry and the 3D model is more representative of the global reaction rate. With attention to different reforming kinetic models, the first aspect to consider is the differences in predicted methane conversion rate. Differences in chemical properties of the anode/catalyst are reflected entirely through their different intrinsic kinetic rates. Consequently, the methane conversions were estimated as 24.7%, 28.6% and 18.6% for the Ahmed, Achenbach and Haberman kinetic models respectively. Lower methane conversion results in less available H2 throughout the cell which consequently can potentially

suppress the current density distribution across the cell active area. Furthermore, the reforming reaction rate is strongly temperature dependent; therefore, different reaction rates lead to different temperature profiles within the anode interior which then can affect prediction of the gas outlet temperature.

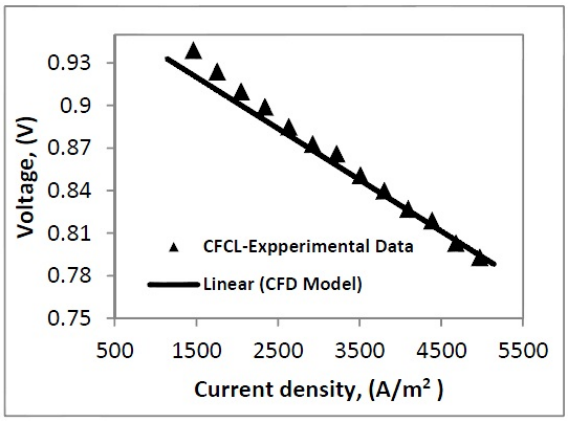

Figure 5.10 - Comparison of the predicted V-I curve from CFD model with experimental data of the same geometry reported by CFCL

Furthermore, the predicted V-I curve is compared with the experimental data of the same geometry reported by CFCL and shown in Figure 5.10. It is worth mentioning that the experimental data and predicted V-I curve are reported under the same operating conditions as it was mentioned in Table 5.5. It can be seen that the CFD model predictions exhibit good agreement in average sense. Similar to the work reported by Xia et al. [63], to accelerate the converged solution, the anode and cathode exchange current densities are considered as the constant fitting parameters. With respect to this mater and uncertainty for different model input parameters which are extracted from the open literature[32, 63, 150], some amount of discrepancy between the predicted results and experimental data is expected. However, the purpose of this work is to develop a 3D CFD model for parametric study of the combined effects for different flow field designs and micro-structural parameters of the anode diffusion layer on the overall performance of the cell. For this reason, the validation goal was not to precisely fit the experimental data, but rather to capture the overall trend of the experimental performance curve.

5.6.3. Effects of Different Flow Field Design

The geometrical factor design including the manifold structure plays an important role in determining the pressure and velocity profiles [53]. Furthermore using a parallel channel configuration has the effect of decreasing the pressure drop; however, it may give rise to the problem of sever flow misdistribution [54]. Thus to analyse the influence of different manifold and channel designs on pressure and velocity profiles, three different anode flow fields were investigated.

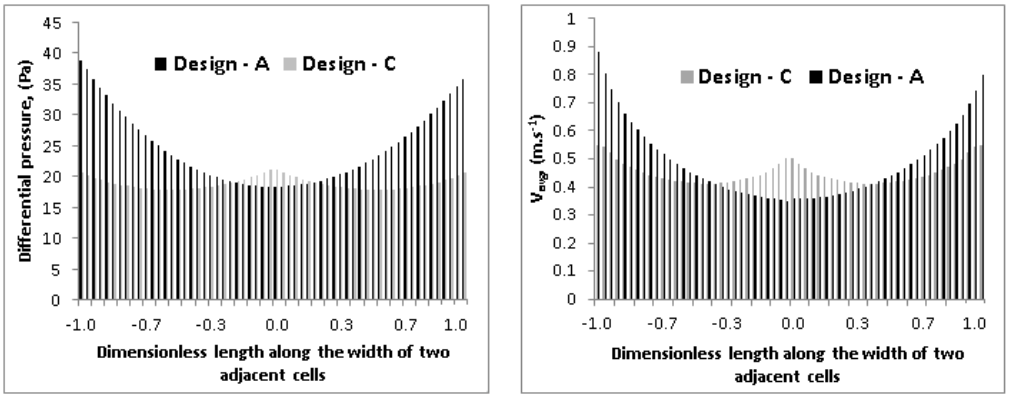

Figure 5.11 - Effects of manifold design on pressure and velocity profiles for case 1 (Comparison between design A and C)

Figures 5.11 and 5.12 present the simulation results along the width of two adjacent cells for the flow field characterisation in different gas channels and without considering any reactions (case 1). In all designs, pressure difference and velocity profiles for channels closer to the inlet and outlet manifolds are higher than that of the middle channels. As it is shown in Figure5.11, due to the identical channel structure of design (A) and (C), the pressure drop along the channels of both designs is comparable. For design (A), the highest pressure drop of about 38 Pa can be found in the channels next to the inlet and outlet manifolds. Corresponding to the direct consequence of the pressure drop, the mean velocity is around 0.9 m/s. However, due to the improvement on inlet manifolds, the parabolic profiles are less pronounced for design (C) and the maximum pressure drop and mean velocity of the channels next to the inlet and outlet manifolds are 23 Pa and 0.55 m/s, respectively. In contrast to design (A), modification of the inlet manifolds as for design (C) established symmetrical pressure and velocity profiles for each individual cell. It is evident that design (A) has significant pressure and velocity

differences within the active area, which can affect species concentration and current density distribution and lead to a lower overall cell performance.

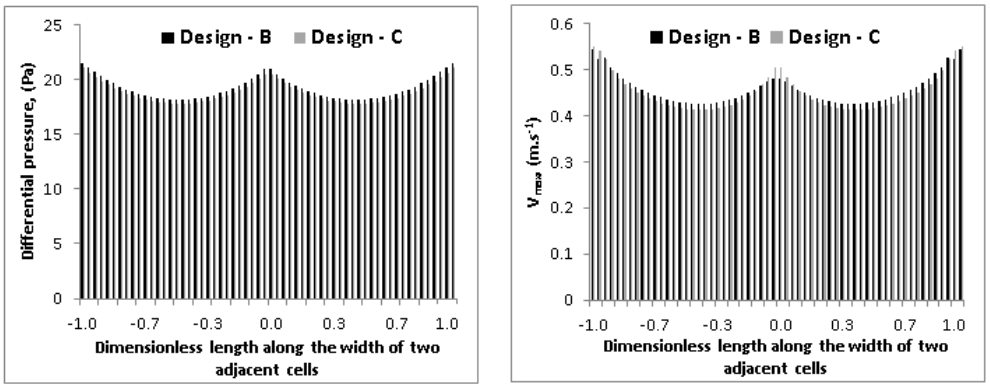

Figure 5.12 - Effects of channel design on pressure and velocity profiles for case 1 (Comparison between design B and C)

Figure5.12 presents the pressure and velocity profiles for two different channel designs. For the spot design, parallel channels are modified by using interlaced ribs, which enable the gas to flow in two directions, while the flow in the parallel design can only proceed along the length of the channels. As can be seen, differential pressure and velocity profiles for parallel and spot designs are quite similar. However, as it is shown in Figure 5.13, for the spot design (design C) at areas adjacent to the conjunction of the horizontal and vertical gas channels, the mean velocity is lower than other parts while design B shows a uniform velocity profile along the length of channels. Therefore, under a high current density, the low velocity regions of design C may causes fuel depletion that may contribute to increasing the severity of thermal stress. In view of this, design (B) is identified as the most homogeneous flow field design.

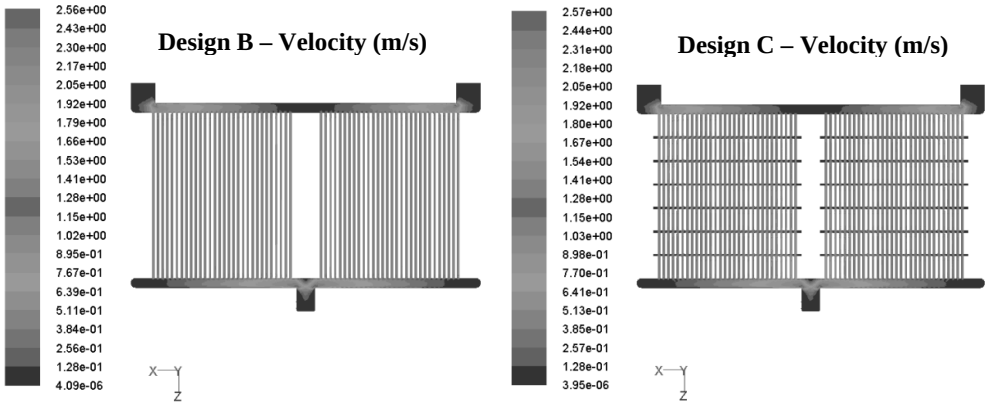

Figure 5.13 - Velocity contours for design B and C

In addition to the above, as it is shown in Figure 5.14, a negative pressure zone was observed at the outlet manifold of all designs that may cause the fluid to flows opposite to its regular direction. In laminar flow condition, curvature is one of the strong reasons for the flow separation [155]; therefore, in general terms we would say that such observed phenomenon may depend on the geometry of the fuel cell or the boundary condition.

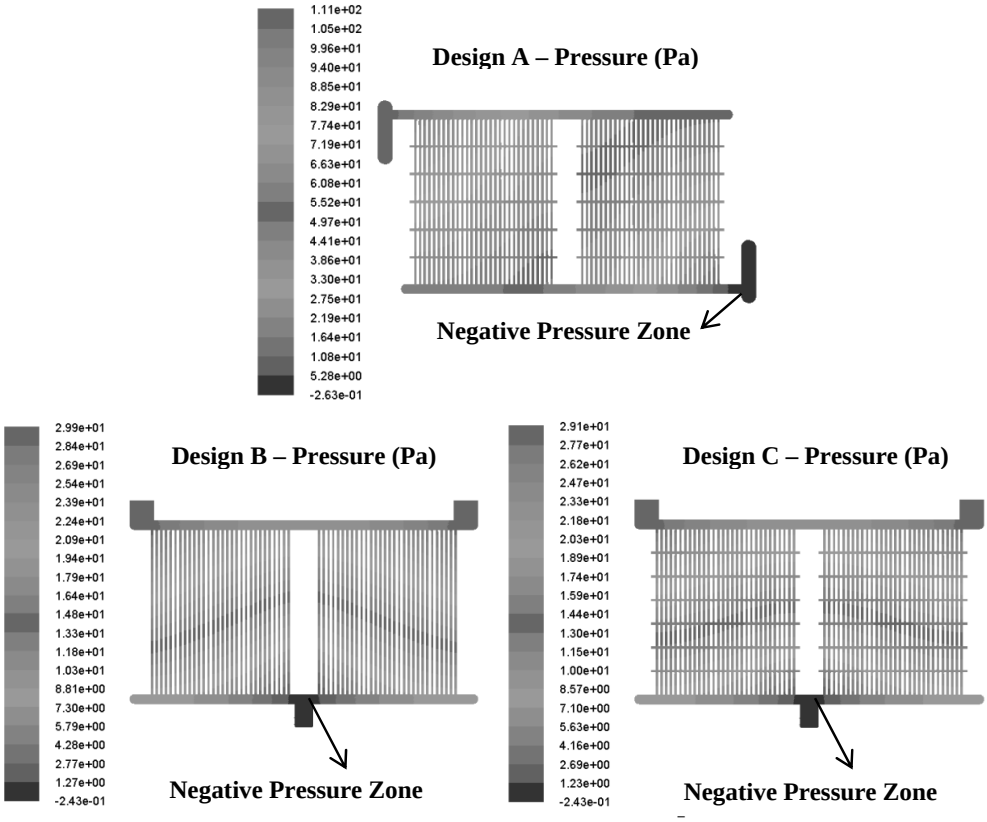

Figure 5.14 - Pressure contours for different designs (A, B and C)

To check the effect of the boundary condition, as it was shown for design (B) through Figure 5.15, under the same boundary condition, when the outlet face was a little bit extended the negative pressure zone disappeared on the extended outlet surface. In addition, the effect of a flow duct structure, which has different curvature, was also examined and as shown in Fig. 5.15 (b), it causes significant improvement over the negative pressure zone. Although analysing the effects of curvature and non-planar double bended geometries on the flow patterns is

complex and need further investigation in future works, according to the simulation results, it can be concluded that under the laminar flow condition and with attention to the effects of curvature, geometrical design of the outlet manifold can influence the creation of the negative pressure zone.

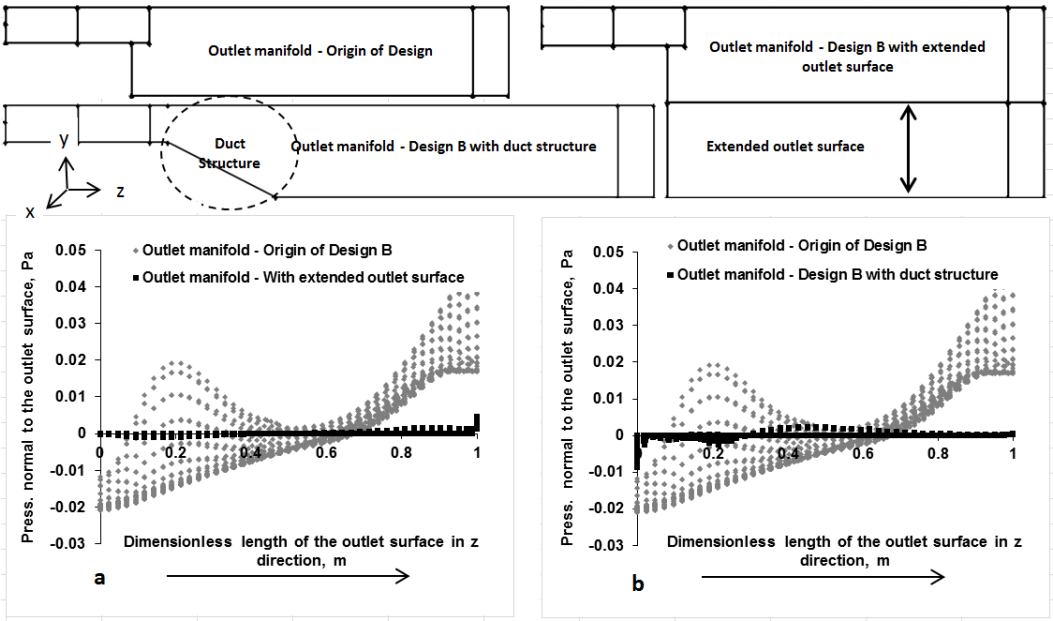

Figure 5.15 - Negative pressure zone for two different outlet manifold designs; a) Comparison with extended outlet surface; b) Comparison with duct structure

5.6.4. Effects of ADL Micro-Structural Parameters

In order to substantiate the effects of the ADL micro-structural parameters on each of the transport processes and the involved reactions, numerical simulation of cases two and three was repeated for different porosities, pore sizes and thicknesses of the anode diffusion layer and then all simulation results are mapped out along three different spatial axes. In view of this, in the following figures, dimensionless thickness represents the distance along the y-axis at 90% length and 50% width of the cell. Additionally, dimensionless width and length signify distances along the x- and z- axis at 90% length and 50% width of the cell respectively.

5.6.4.1. Effects of Porosity

Figure 5.16 illustrates the simulation results of case 2 for different porosity of the anode diffusion layer along the length of the cell.

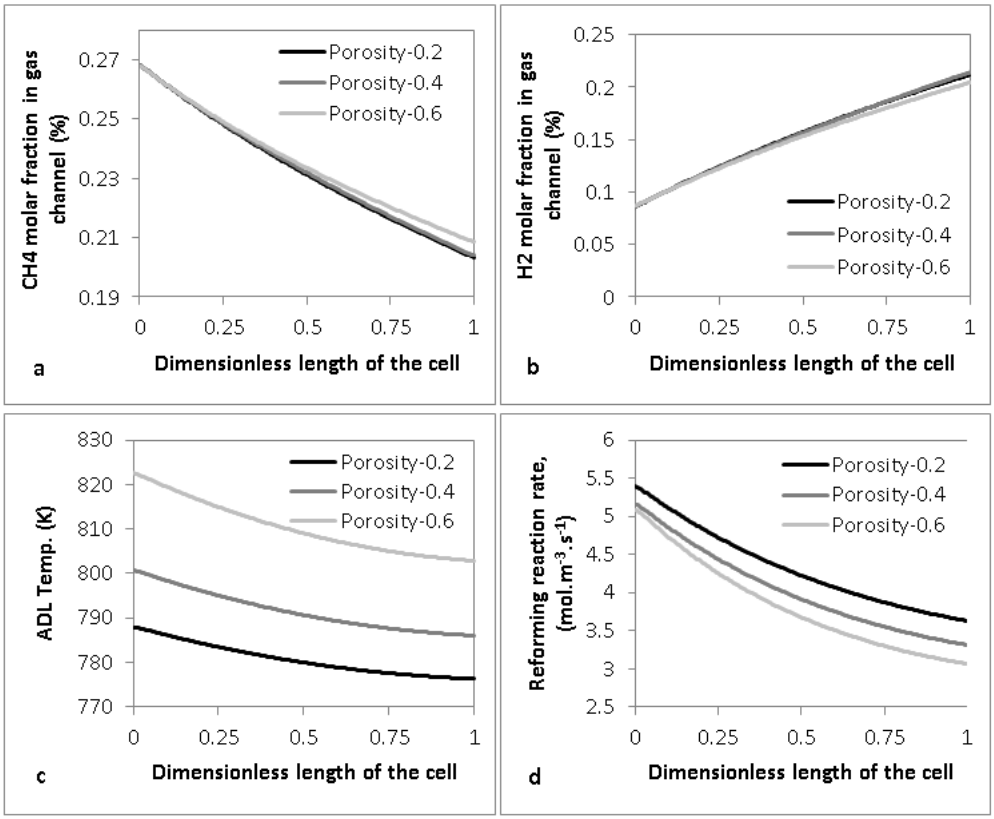

Figure 5.16 - Simulation results for the effect of porosity along the length of the cell (Case 2)

As shown here, without considering the electrochemical reaction and thermal effect of the air flow, reforming reaction rate and temperature drop increase while porosity varies from 0.6 to 0.2. However, under the effect of different porosities and within the initial length of the cell, the differences between the reforming reaction rates are less significant. Furthermore, distributions of methane and hydrogen molar fractions are quite similar for the porosities of 0.2 and 0.4. The results may come from the combined effects of porosity on effective diffusion and catalytic surface area. Increasing the electrode porosity causes the cross section of the gas flow to be increased and promotes the influence of the gas inlet operating

conditions and components' diffusion inside the porous media that is beneficial to the reforming reaction rate. On the other hand, as it was shown in Eq. (5-50). Increasing the electrode porosity means less reactive surface area that is predominant for decreasing of the reforming reaction rate.

In addition, distribution of temperature, reforming reaction rate and species molar fractions along the other spatial paths provide better view for the combined effects of the geometrical factors and micro-structural parameters on transport phenomena within the cell. In this regard, Figure 5.17 shows distribution of various fields along the width of the cell. As shown here, molar fraction of methane is higher in side channels while decreasing the ADL porosity causes the reduction of methane concentration for the mid channels to be increased. This observation reveals the complex interaction between the anode flow field design and micro-structural parameters of the anode diffusion layer. As shown earlier (Figure 5.12), for the channels closer to the inlet and outlet manifolds, gas velocity is higher than that of the mid channels, which in turn decreases the residence time of the reactants. Therefore, in regions with lower residence time, decreasing porosity causes the effects of the components' diffusional resistance to become more significant, which consequently causes less amount of methane to be involved in the reforming reaction. On the contrary, in the mid channels with higher residence time, beneficial effect of the lower porosity on reactive surface area becomes more noticeable and causes the molar fraction of methane to be decreased. The simulation results along the thickness of the cell (Figure 5.18), provides clear evidence for the opposite effects of porosity on effective diffusion and catalytic surface area. In view of this, it is interesting to note that although the reforming reaction rate for the porosity of 0.2 is slightly higher than porosity of 0.4, less amount of hydrogen diffuses towards the anode gas channels.

In short, under the effects of the catalytic chemical reactions, porosity of 0.4 seems to be more appropriate for the performance of the reforming reaction. However, to obtain the optimum value of porosity, we need to include the heat effects of the air channels and do trade-off between the influences of chemical and electrochemical reactions. In view of this, more analysis have been conducted and shown below.

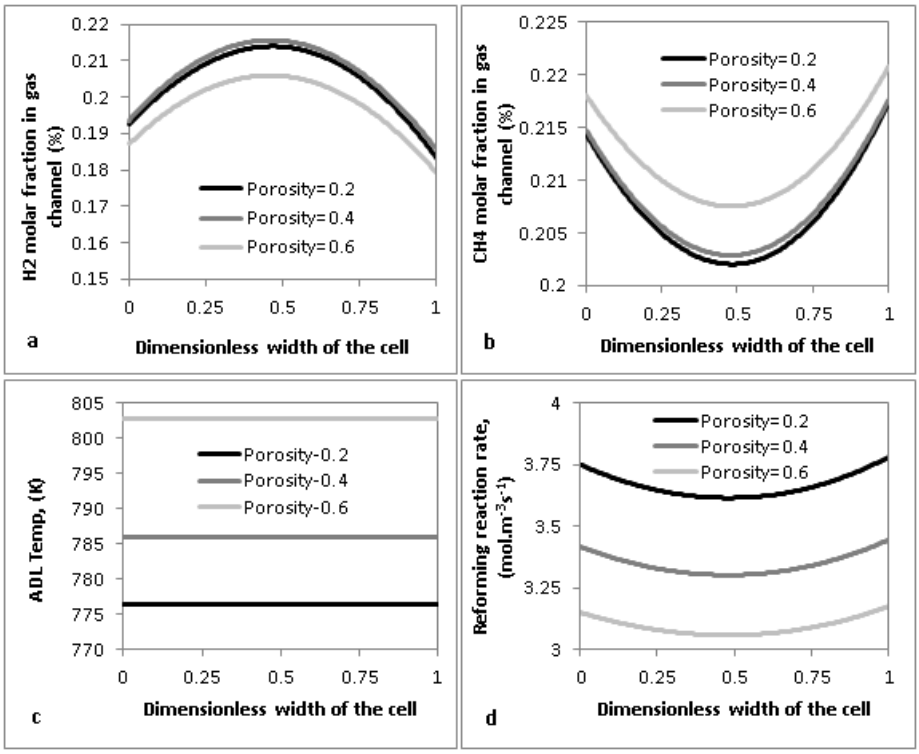

Figure 5.17 - Simulation results for the effect of porosity along the width of the cell (Case 2)

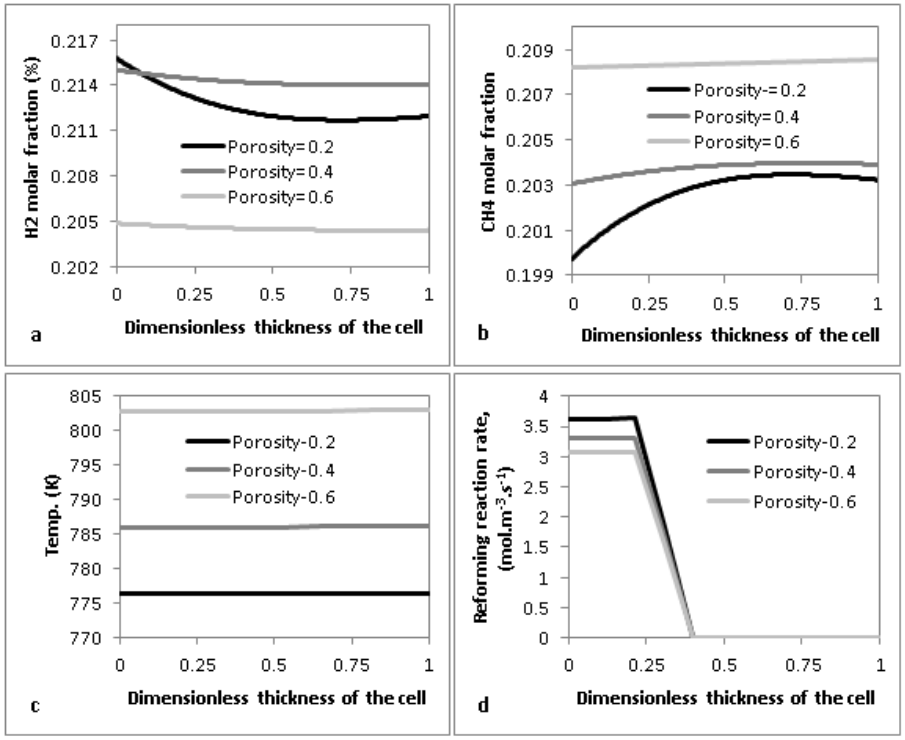

Figure 5.18 - Simulation results for the effect of porosity along the cell thickness (Case 2)

Figure 5.19 shows the simulation results of case 3 for the effects of different porosity on distribution of different parameters along the length of the cell. As shown earlier, decreasing of porosity causes the reactive surface area to be increased. On the other hand, decreasing porosity hinders multi component gas transport within the anode diffusion layer. It consequently increases differences of methane and hydrogen molar fractions between the anode diffusion layer and gas channels (Figure 5.19a, b). In view of this, although at porosity of 0.2, less methane diffuses through the anode diffusion layer, stimulating heat effect of the air flow and electrochemical reaction rate in addition to availability of more reactive surface area offset the resistance of the porous structure to the multi component gas transport. Therefore, it causes the reforming reaction rate within the anode porous media to be increased (Figure 5.19d). Further, it can be seen from Figure 5.19c that decreasing porosity affects distribution of the current density while it causes the location of the maximum current tends to shift towards the inlet regions of the cell. This observation underlines the complex interplay between the reforming and electrochemical reaction rates on distribution of fields. As shown in Figure 5.19e, the cooling effect of the reforming reaction is counterbalanced with the amount of heat released from the electrochemical reactions followed by gradual temperature increase across the length of the cell. In addition, at porosity of 0.2, temperature drop is effectively decreased within the small length of the inlet regions that consequently can improve thermal stability of the cell. Moreover, temperature profile at porosity of 0.6 is placed in between the profiles relevant to porosities of 0.2 and 0.4. This observation again highlights the importance of interplay between the reforming and electrochemical reaction rates. It can also be recognized from Figure 5.19f, that small changes in the anode activation overpotential can result in relatively large changes in current density. This is due to the exponential correlation between these two. Furthermore, it is evident from figure 5.19g that distribution of the ohmic overpotential is dictated by two different variables: current density and temperature.

In continuation of the above descriptions, Figure 5.20 shows the simulation results of case 3 to analyse the effect of different porosity on overall performance and distribution of different parameters along the width of the cell.

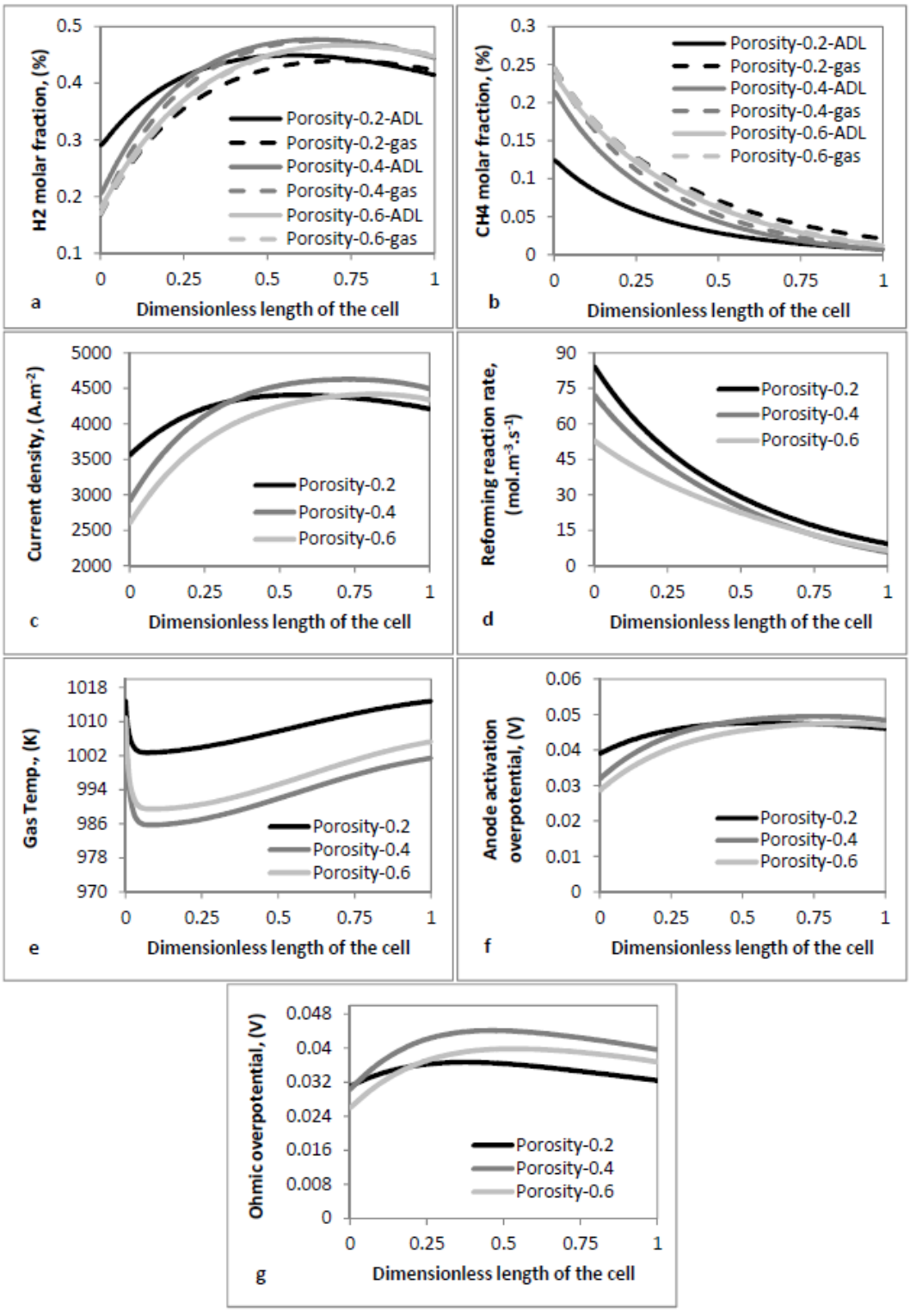

Figure 5.19 - Simulation results for the effect of porosity along the length of the cell (Case 3 – $E_{cell} = 0.819$ V)

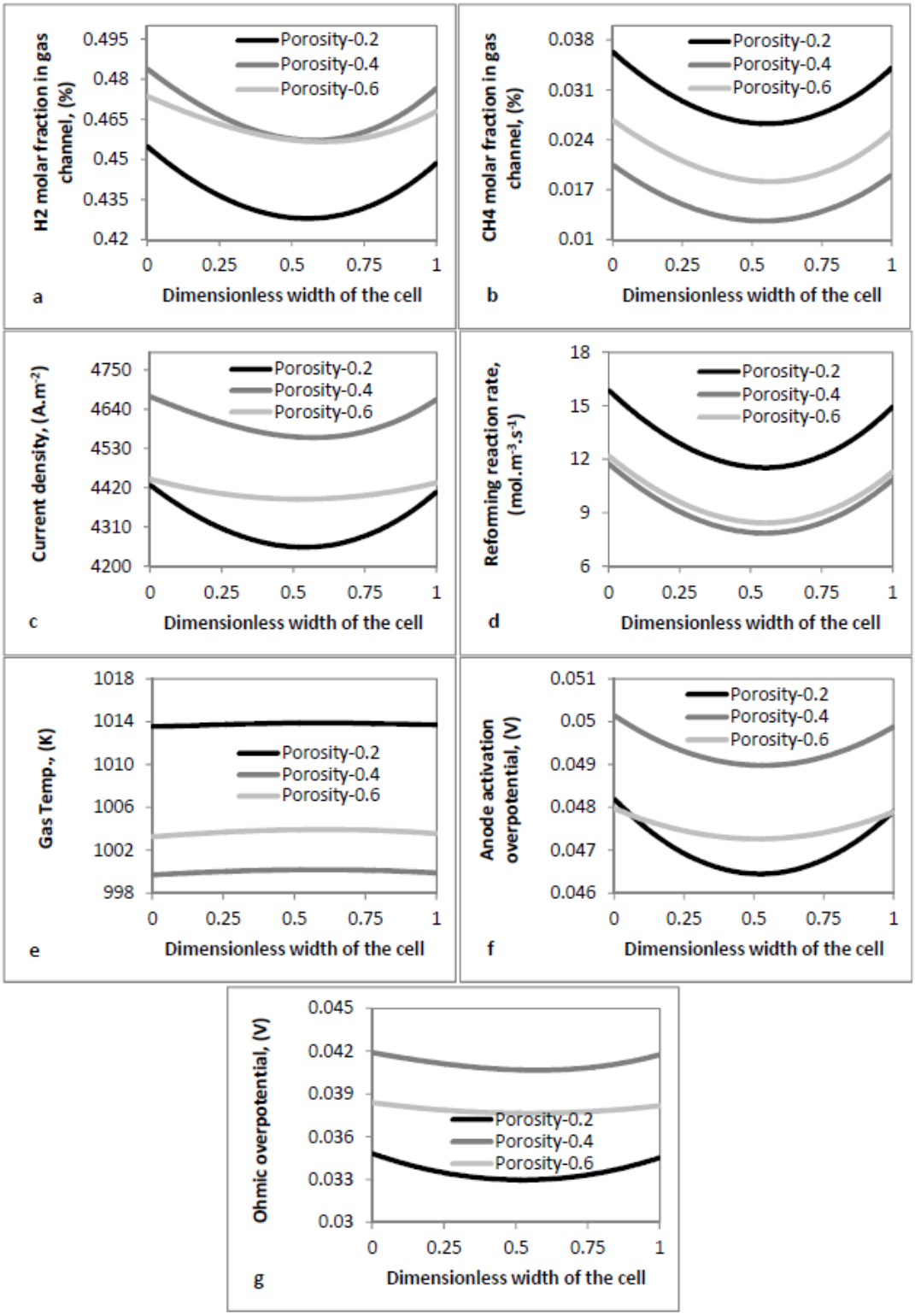

Figure 5.20 - Simulation results for the effect of porosity along the width of the cell (Case 3 – $E_{cell} = 0.819$ V)

Comparing to the simulation results for case 2 (Figure 5.17), distribution of hydrogen comes into different view (Figure 5.20a). This observation can be explained by dominant influence of the electrochemical reaction rate on consumption of hydrogen over the effect of the catalytic reforming on hydrogen yield. However, similar to the simulation results of case 2, under the combined effects of the anode flow field design and micro-structural parameters of the anode diffusion layer, decreasing porosity causes further variation in distribution of different parameters across the width of the cell. In view of this, porosity of 0.2 results in further variation of the current density, activation overpotential and ohmic overpotential across the width of the cell, while their magnitudes are justified with the same reasons explained on Figure 5.19. However, considering the operating conditions and distribution of the same parameters along the length of the cell, it can be concluded that an optimum porosity that results in best performance for the reforming reaction of case two, will not result in best SOFC performance. Decreasing of porosity causes less temperature drop and more uniform distribution of temperature and current density; therefore, lower porosity is beneficial for the overall performance of the cell. Another key conclusion that can be drawn from the above results is that each of the geometrical factors, micro-structural parameters and reaction rates can effectively influence the engineering of the anode diffusion layer, which in turn affects distribution of the process variables across different spatial domains.

5.6.4.2. Effects of Pore Size

In addition to porosity, pore size is another important structural parameter influencing the multi component gas transport and overall performance of the cell. In this regard, Figures 5.21 illustrates the simulation results of case 2 for analysing the effects of the pore radius on distribution of important parameters across the length of the cell. Similar to the results reflecting the effect of the electrode porosity, as the pore size decreases, the reforming reaction rate increases and the smallest pore size is beneficial to that. However, unlike the effects of porosity, variation of the pore size has intensive effects on components' gas transport, reforming reaction rate and temperature drop. This observation may be justified by the strong effects of the pore size on reactive surface area and components

diffusional resistance. Again to further illustrate this effect; Figure 5.23 presents the distribution of the same parameters along the thickness of the cell.

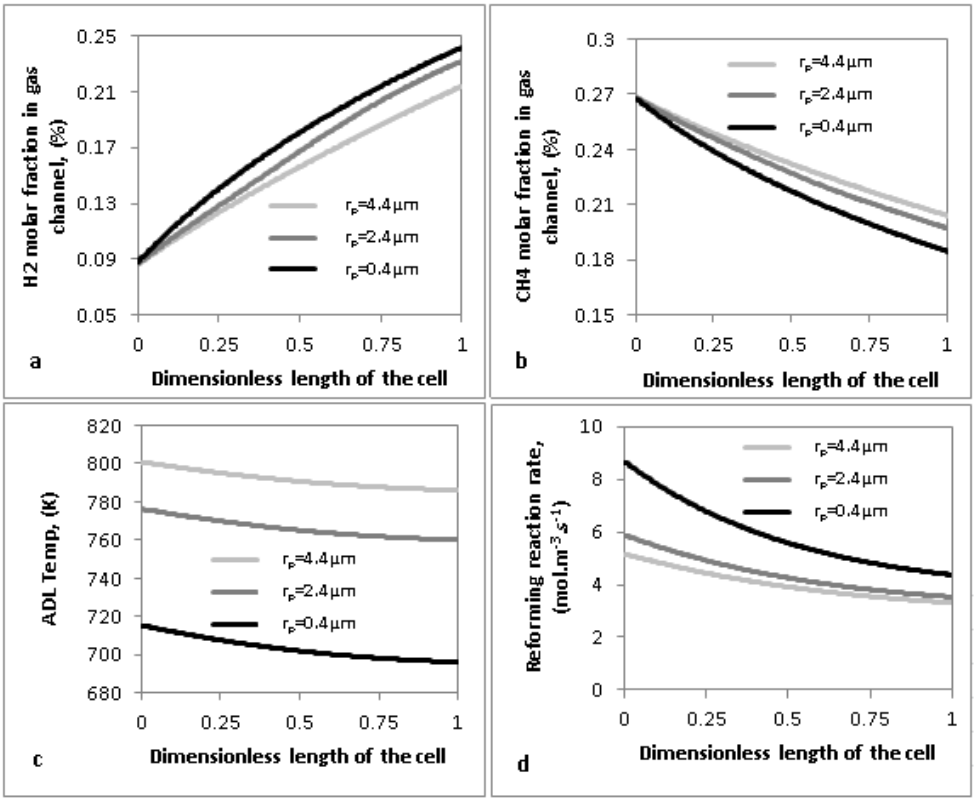

Figure 5.21 - Simulation results for the effect of pore size along the length of the cell (Case 2)

In addition, similar to the effects of the ADL porosity, decreasing the pore size results in further variation of the components' molar fractions and reforming reaction rate along the width of the cell (Figure 5.22). This finding gives another evidence for the predominant effect of the reactive surface area over the components' diffusional resistance for longer residence time and larger reactive area that consequently increases the reforming reaction rate. However, in order to determine the optimum value of the pore size, we need to analyse the overall performance of the cell including all chemical and electrochemical reactions and heat effects of the air flow. In this regard, Figure 5.24 shows the simulation results of case 3 to analyse the effects of the pore radius on overall performance and distribution of different parameters along the length of the cell. It is interesting to mention that the maximum reforming reaction rate and consequently, the maximum methane conversion corresponds to the pore size of 2.4 µm, which is in the middle of the pore size range.

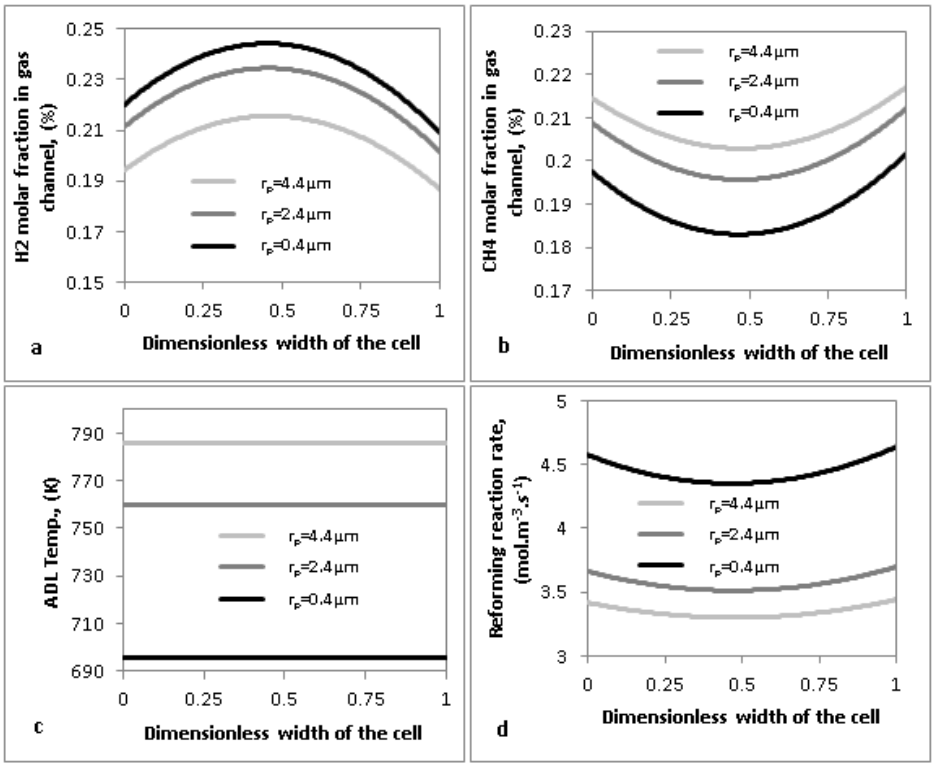

Figure 5.22 - Simulation results for the effect of pore size along the width of the cell (Case 2)

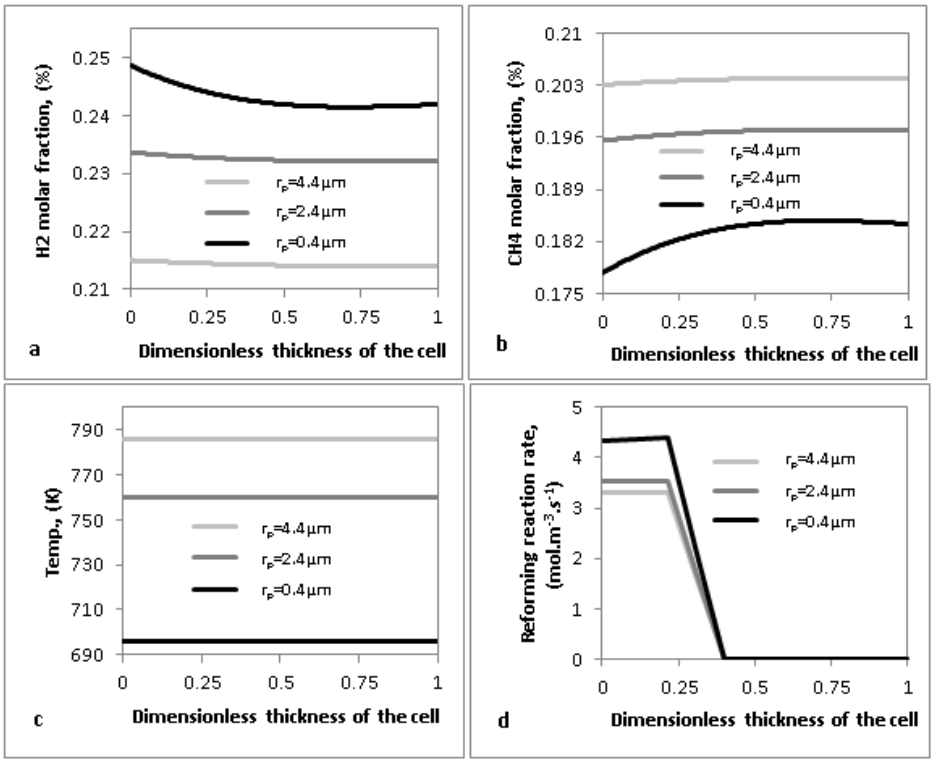

Figure 5.23 - Simulation results for the effect of pore size along the cell thickness (Case 2)

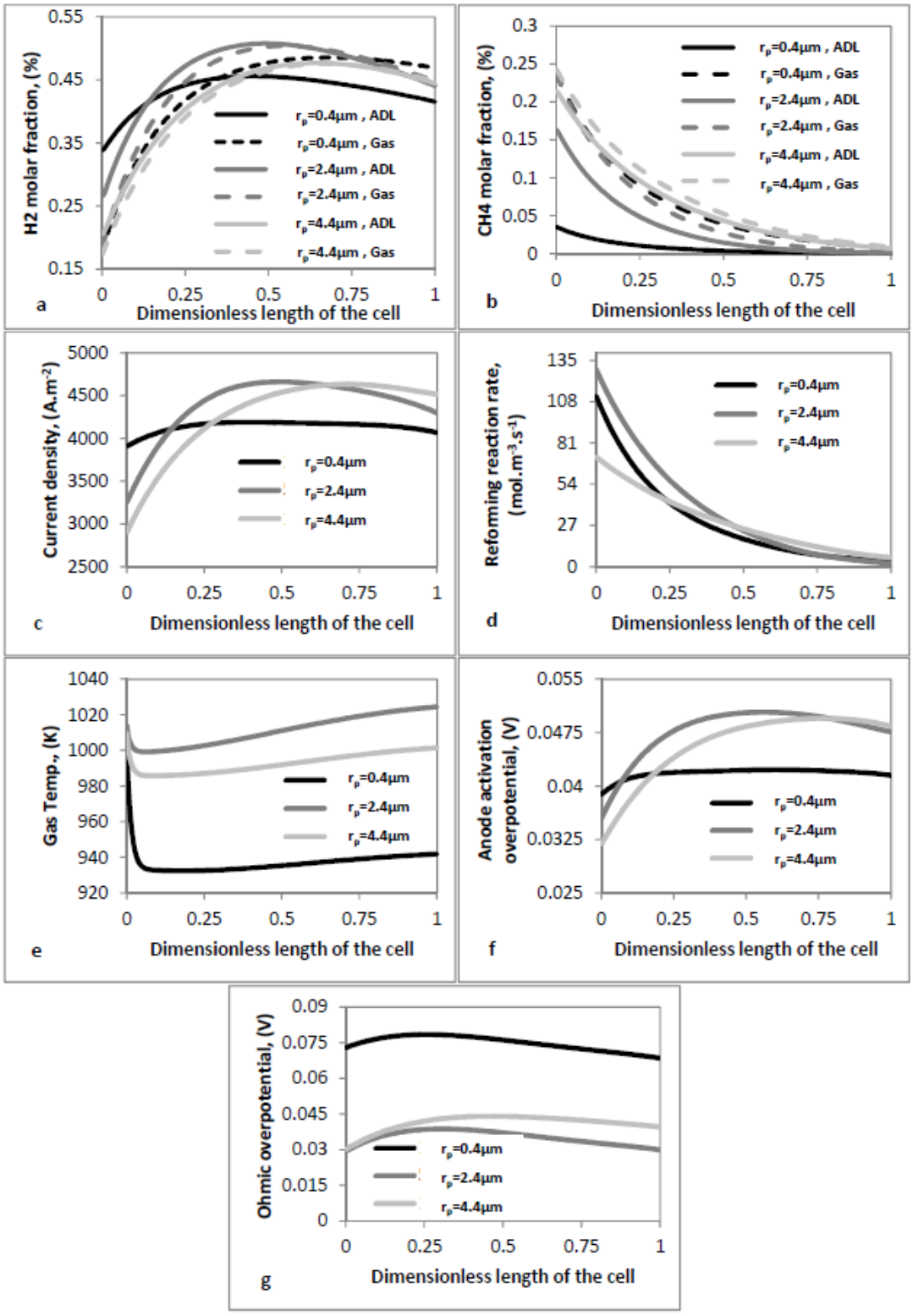

Figure 5.24 - Simulation results for the effect of pore size along the length of the cell (Case 3 – E_{cell} = 0.819 V)

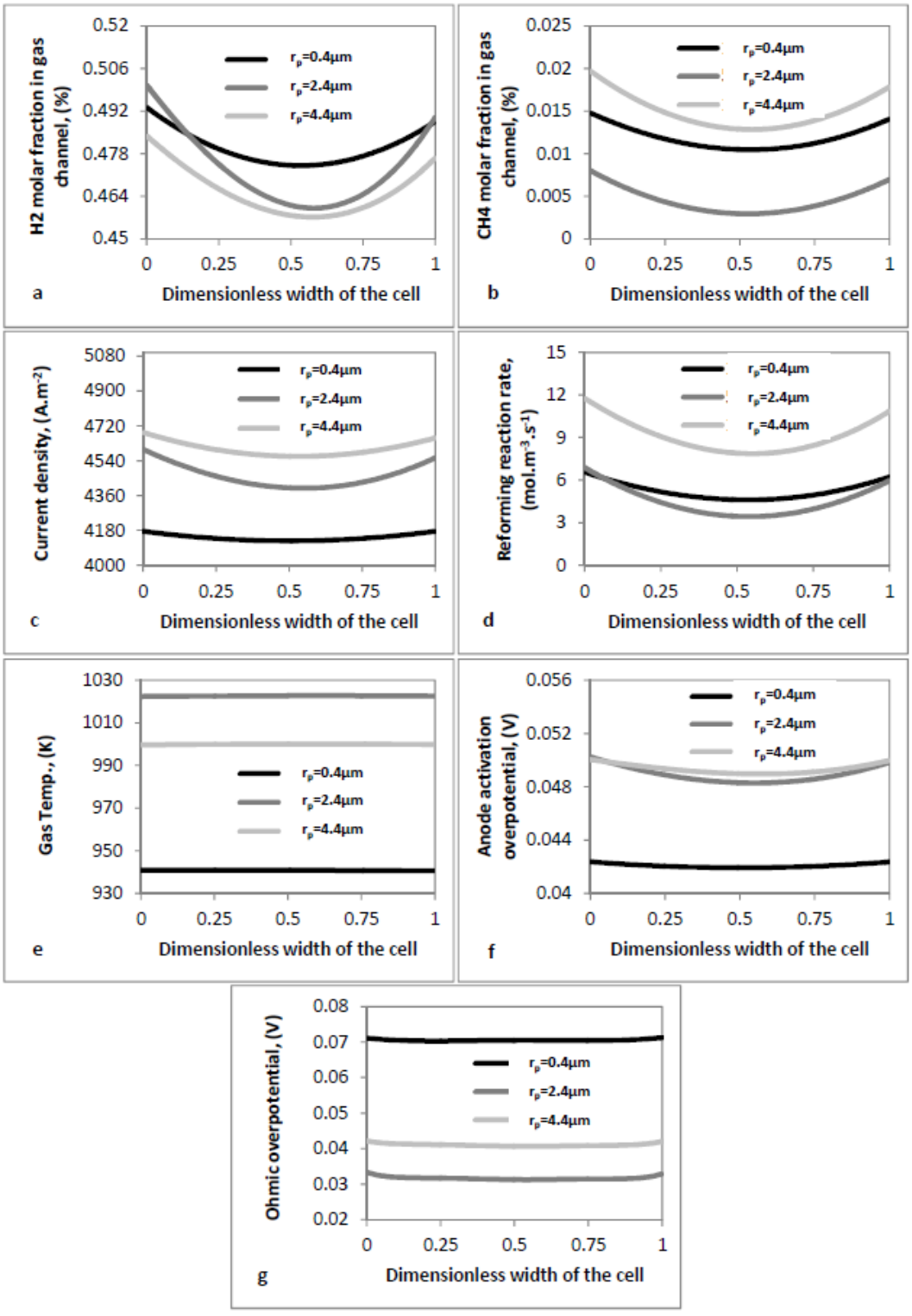

Figure 5.25 - Simulation results for the effect of pore size along the width of the cell (Case 3 – E_{cell} = 0.819 V)

This observed phenomenon is justified as follows. Decreasing the pore size increases the reactive surface area. On the contrary, as shown in Figure 2.24a, b, decreasing the pore size causes the reactants' diffusional resistance and consequently the differences between the reactants' molar fractions between the anode diffusion layer and gas channels to be significantly increased. Therefore, as expected, not only the multi component gas transport but also the current density is significantly influenced. Therefore, the mid-range of the pore size (2.4 μm) is beneficial to the overall performance of the cell. In other words, excepting initial length of the cell, the lowest pore size decreases the cell performance significantly. This is due to the less amount of H2 within the initial length of the gas channels, heat effects of the reforming reaction rate and two different mechanisms governing the molar fraction of hydrogen at a given operating conditions: (1) H2 production due to the reforming and water gas shift reactions and (2) resistance of the porous anode to H2 diffusion [32]. In view of this, for the smallest pore size (0.4 μm), the initial length of the anode diffusion layer is less influenced by the fuel inlet operating condition and the hydrogen produced from the reforming reaction effectively promotes the electrochemical reaction rate (Figure 5.24c). Simultaneously, the hydrogen molar fraction in fuel gas channels increases across the length of the cell (Figure 5.24a). Therefore, except for the initial distance of the cell, hydrogen diffusion from the gas channels to the reactive surface area of the anode catalyst layer become critical. Thus considering substantial components' diffusional resistance of the smallest pore size, the overall performance of the cell decreases significantly. Moreover, under the combined effects of the reforming and electrochemical reaction rates, the mid-range of the pore size results in less temperature drop while the smallest pore size causes the fuel gas temperature to be decreased significantly. It can also be observed from Figures 5.24f and 5.24g that distribution of the activation overpotential is consistent with the current density and temperature. Meanwhile the mid-range of the pore size results in the less amount of the ohmic overpotential.

In addition to the above, Figure 5.25 shows the simulation results of case 3 to analyse the effects of the pore size on overall performance and distribution of different parameters along the width of the cell. Similar to the reasons explained for the effects of porosity, the distribution of hydrogen can be viewed differently.

However, the mid-range pore size that maximise reforming and overall performance of the cell, exhibits obvious variation in distribution of different parameters across the width of the cell. Nevertheless, considering the operational condition and comparing with distribution of the same parameters along the length of the cell, this variation is relinquished. Therefore, in contrast with the conclusion from the simulation results of case two, under the influences of the electrochemical reaction rate and heat effects of the air channels, the mid-range of the pore size is the most appropriate for engineering of the anode diffusion layer.

5.6.4.3. Effects of Thickness

Since an anode supported SOFC is studied in this work, the effects of the ADL thickness on the SOFC performance is another parameter that needs to be investigated. In this regard, simulation results of case two across different spatial domains are given in Figures 5.26 to 5.28.

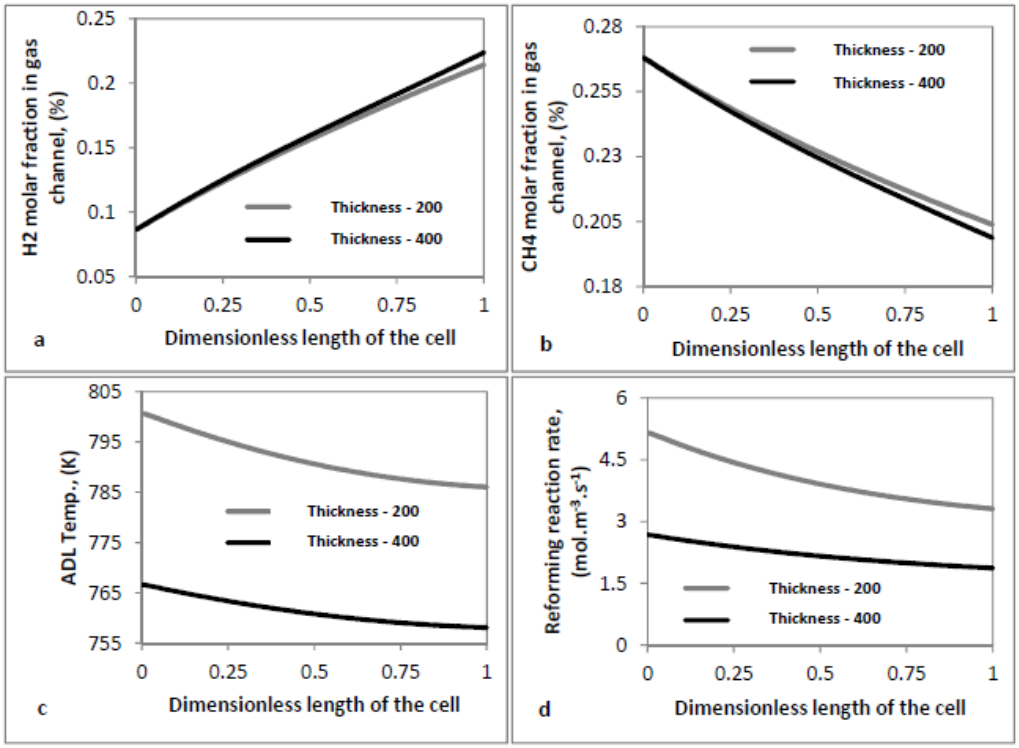

Figure 5.26 - Simulation results for the effect of ADL thickness along the length of the cell (Case 2)

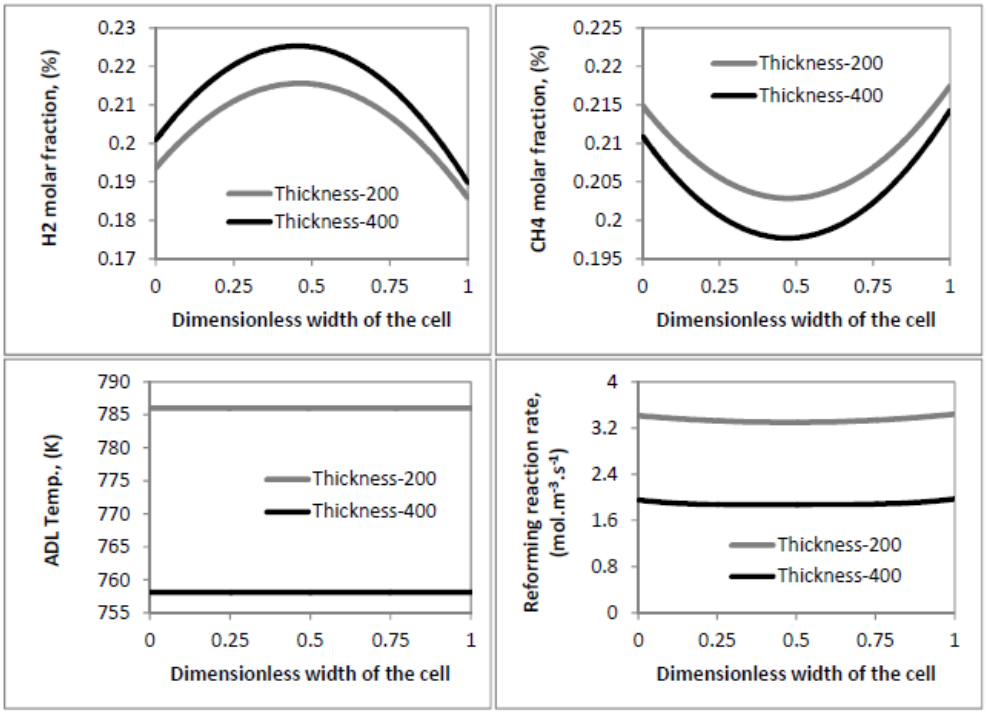

Figure 5.27 - Simulation results for the effect of ADL thickness along the width of the cell (Case 2)

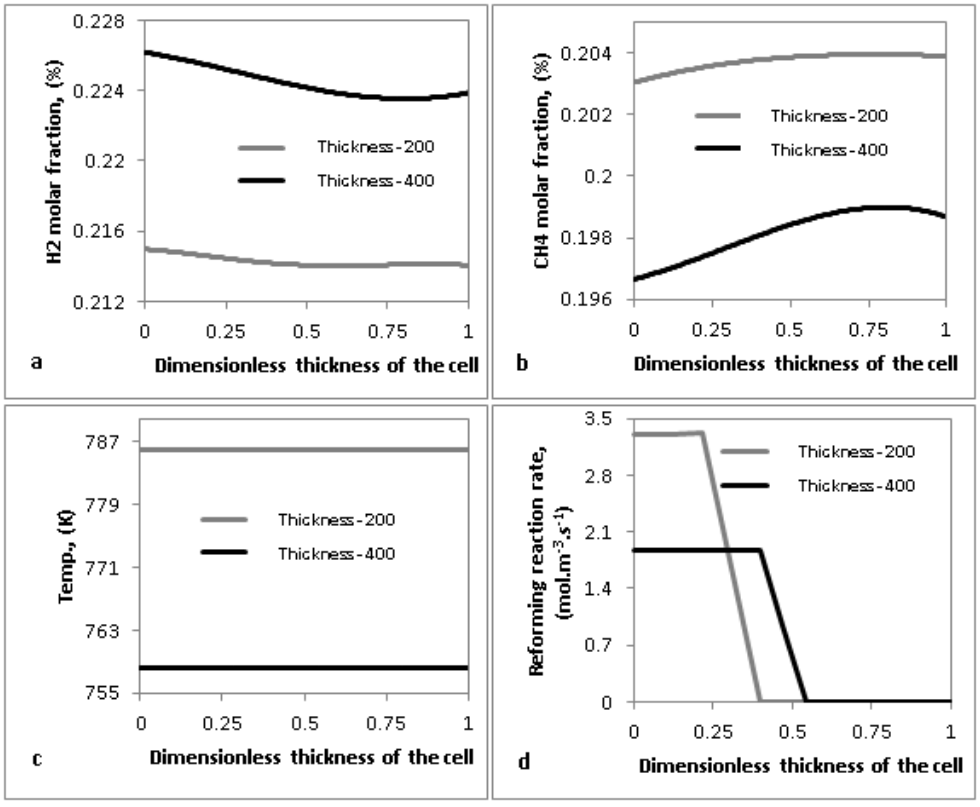

Figure 5.28 - Simulation results for the effect of ADL thickness along the cell thickness (Case 2)

As shown in Figures 5.26 to 5.28, temperature decrease and methane conversion into hydrogen are found to be increased with increasing ADL thickness. It is consistent with the fact that increasing the ADL thickness provides a sufficient number of the catalytic sites that are required for the methane reforming reaction to occur [156]. However, at the same position within the anode diffusion layer closing to the interfaces with the anode catalyst layers (ACL), increasing the ADL thickness causes the reforming reaction rate to be decreased and its distribution along the length of the cell becomes less intensive (Figure 5.26d). This is due to the combined effects of the species transfer limitation and dilution of methane with product (Hydrogen) [156]. It is worth noting that increasing the ADL thickness increases diffusion path for the reactants to reach the reactive sites, which in turn increases the resistance to diffusional mass transfer. Distribution of the same parameters along the cell thickness provides better view for the above explanations (Figure 5.28). In addition, as shown in Figure 5.27, distribution of different parameters along the width of the cell reveals the intensification effect of the resistance to diffusional mass transfer at higher ADL thickness. In view of this, for the mid channels with higher residence time, gas reactants are provided with more time to be involved in the catalytic reforming reaction, which in turn causes further decreasing of the methane molar fraction at this region.

Finally, the simulation results of case 3 including the influences of the ADL thickness, electrochemical reaction and heat effects of the air channels are given in Figures 5.29 and 5.30. In this regard, the hydrogen molar fraction is found to be controlled by both the reforming and electrochemical reaction rates (Figure 5.29a). In view of this, hydrogen molar fraction increases within the initial length of the cell because the methane conversion mainly occurs in this region. After a maximum, the hydrogen concentration decreases until the cell outlet as it is oxidised all along the length of the cell. As shown in Figures 5.29a and 5.29b, again it is worth noting that the increasing of the differences of hydrogen and methane molar fractions between the anode diffusion layer and gas channels is a good evidence for the effects of the ADL thickness on the species diffusional resistance, which in turn intensifies decreasing of the reforming reaction rate for 400 μm thick of the anode diffusion layer (Figure 5.29d).

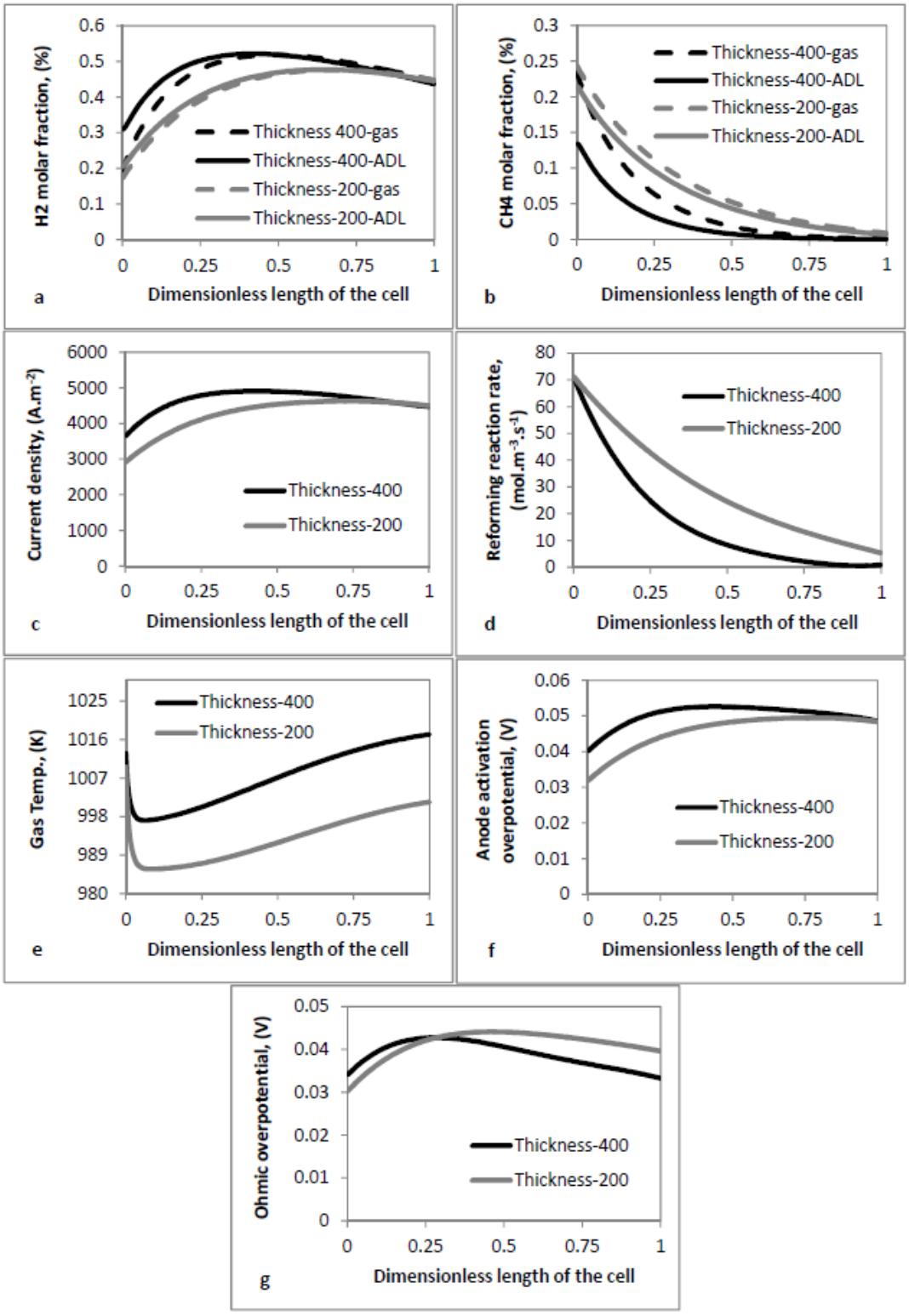

Figure 5.29 - Simulation results for the effect of ADL thickness along the length of the cell (Case 3 – E_{cell} = 0.819 V)

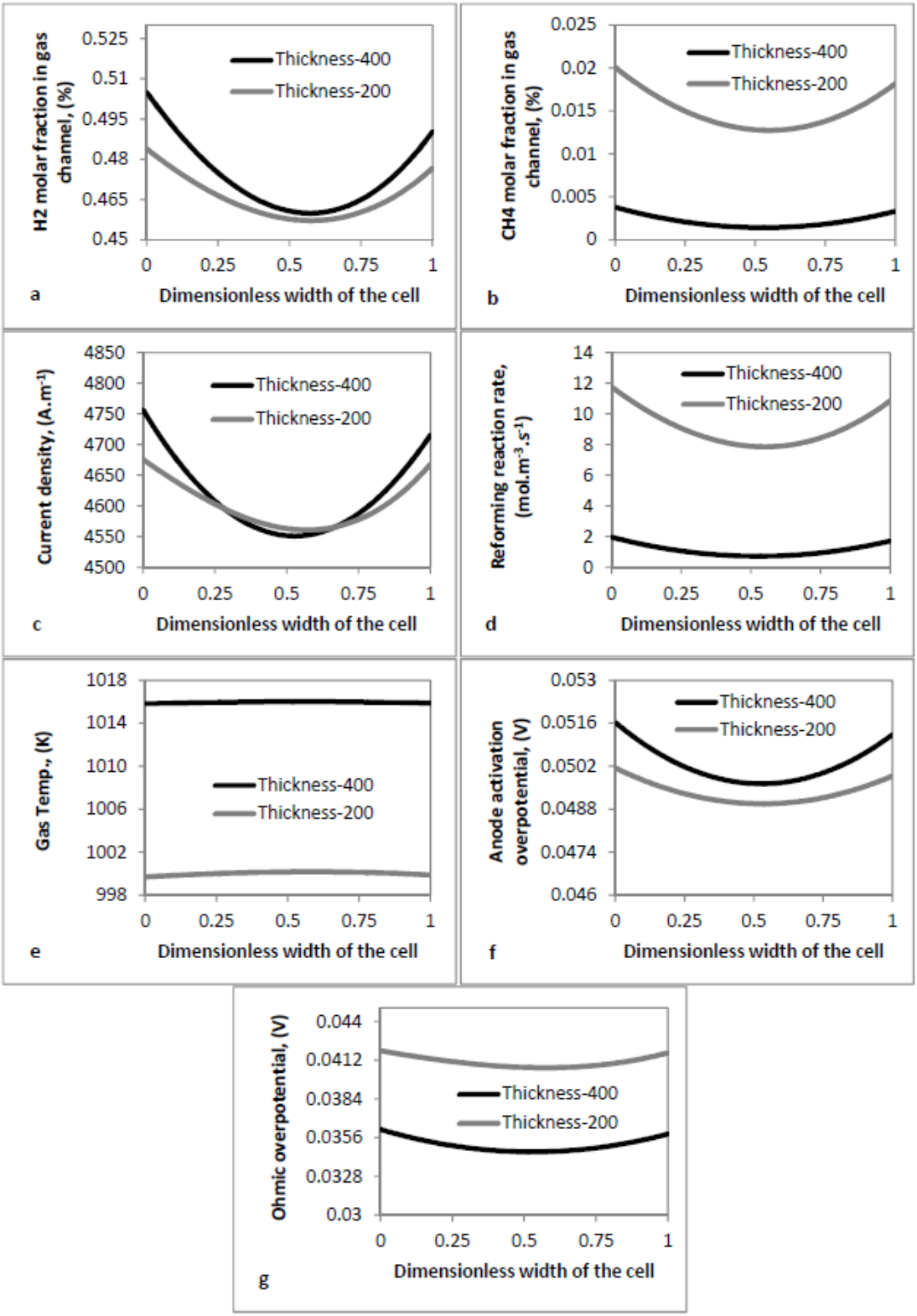

Figure 5.30 - Simulation results for the effect of ADL thickness along the width of the cell (Case 3 – E_{cell} = 0.819 V)

However, improving the electrochemical performance is obtained by increasing the anode thickness that is linked to the amount of hydrogen produced by the reforming reaction. Figures 5.29f and 5.29g present the evaluation of the anode activation and ohmic overpotentials along the length of the cell, which are consistent with distribution of temperature and current density. Again, under the combined effects of the reforming and electrochemical reaction rates, increasing the ADL thickness improves temperature decrease and ohmic overpotential.

Lastly, the simulation results of case 3 for analysing the effect of the ADL thickness on distribution of the same parameters across the width of the cell is shown in Figure 5.30. The point that needs to be explained here is the dissimilar effect of the ADL thickness on variation of the reforming and electrochemical reaction rates at 90% length and along the width of the cell. This is probably due to the reactants' molar fractions. As it is shown in Figure 5.30b, for the ADL with 400 μm thick, methane conversion is almost 100% and then the reforming reaction rate is less influenced by the reactants' diffusional resistance. However, the concentration of hydrogen is quite high; therefore, distribution of the current density is more influenced from both the hydrogen diffusional resistance and residence time distribution. In view of this, overpotentials and temperature profiles are consistent with the reaction rates.

5.2. Summary

A 3D CFD model was developed to study the combined effects of the geometrical factors and micro-structural parameters of the anode diffusion layer on the distribution of the key parameters along different spatial domains of an industrial planar SOFC previously designed by CFCL. In this study, it was shown that increasing the number of the inlet manifolds is beneficial for less pressure drop and uniform velocity profile over the cell active area. Furthermore, geometrical design of the outlet manifold may influence the creation of negative pressure zone. In addition, modifying parallel channels to the spot design, causes decreasing of the mean velocity at areas adjacent to the interlaced ribs. This can result in fuel depletion and consequently contributes to increase the severity of thermal stress. In continuation of the above, distribution of the key parameters along different spatial

domains reveals the complex interaction between the anode flow field design and microstructural parameters of the anode diffusion layer. This can effectively influence the variation of different parameters across different distances of the cell, which in turn affects the engineering of the anode porous media. However, it is worth noting that microstructural parameters were found to have conflicting effects on multi component gas transport and the involved reactions. From the simulation results, it can be concluded that an optimal set of micro structural parameters, which resulted in the best performance for the reforming reaction rate, will not automatically result in best SOFC performance. In view of this, the ADL structure with porosity of 0.4 and smaller pore radius is beneficial for the reforming reaction rate. However, including the electrochemical reaction and heat effects of the air channels denotes different engineering for maximum utilization of the anode diffusion layer. In this regard, it is beneficial to keep the porosity low and do a trade-off between the thickness and pore size of the ADL. Considering the operating conditions and model input parameters, it was concluded that the mid-range of the pore size is beneficial to the overall performance of the cell. Moreover, it was shown that with a larger ADL thickness, the SOFC performance increases. However, it can reduce the reforming reaction rate due to the dilution of the reactants with product.

Chapter 6

Conclusions and Future work

6.1. Conclusions

This thesis focused on improvements for multi scale modelling of the planar SOFC. In view of this, the following key conclusions can be drawn from the results of this research.

A decent agreement was obtained between the steady state predicted results from the developed PFR model and the experimental data published in the literature. Furthermore, it was shown that under the steady state operating condition, no charging or discharging process occurred; therefore, Faradic and electrolyte current densities are identical. On the other hand, in response to a voltage step change, apart from the first initial jump of the electrolyte current density, double layer charging and discharging process has insignificant effect on transient behaviour; while the slow dynamics of the cell to a voltage step change is mainly governed by temperature. On the contrary, when SOFC is subjected to a sinusoidal voltage, temperature and reactants' concentration are not sensitive to the high frequent voltage change, while dynamic response of the cell is mainly controlled by the electrochemical reactions and double layer charging and discharging processes. In view of this, depending on double layer capacities, a continual difference between the Faradic and electrolyte currents was observed. However, there is a direct relation between current and overpotentials. Therefore, at the cathode-electrolyte interface with higher resistance to the half-cell electrochemical reaction, the activation overpotential and consequently the Faradic current density become less sensitive to the sinusoidal variation of voltage.

However, not all reactors are perfectly mixed, nor do all reactors exhibit plug flow behaviour. Additionally, the effects of the flow field design and different fuel and air flow configurations cannot be considered in these simplified models. Therefore, as

the next step, a new dynamic tank in series reactor (TSR) model of a planar SOFC operating with co-, counter and cross flow directions was developed for the first time. The reduction in model complexity has been achieved by replacing a planar SOFC with a network of several continues stirred tank reactors (CSTR). This makes TSR model to be computationally fast compared to CFD models for sketching 2D visualization map of the SOFC performance. The V-I curves predicted from the TSR model at three different flow rates of the hydrogen fuel were justified by comparison with the experimental data from literature. Furthermore, examination of the simulation results indicates the possibility of enhancing the fuel cell performance by decreasing the maldistribution of the fields. In addition, the simulation results demonstrate strong coupling between the temperature, species concentration, activation overpotential and current density, while these results highlighted the influence of different fuel and air flow configurations on the steady state and dynamic behaviours. In view of this, the co-flow case was the most favourable for the planar SOFC with improved performance, while its response to a voltage step increase provided the most uniform transient behaviour at different points of the cell. Moreover, it can be concluded that for the co-flow direction, temperature dominates the slow dynamics of the local current density whereas in the low temperature regions of the counter and cross flow cases; the slow dynamics of the current density tends to be characterized by the initial undershoot followed by a slower transient response. This is due to the combined effects of the diffusion resistance within porous electrode, hydrogen accumulation toward the fuel outlets and influence of the PEN temperature.

To further improve the TSR model, we need to implement the gas flow distribution patterns. In addition, to meet the scope of the future work, it will be good if we can compare 2D distribution of the key parameters predicted from TSR model, with the results from a 3D CFD model of an industrial case. In view of this, a 3D CFD model accounting for the effects of different anode flow fields, previously designed by CFCL, on pressure and velocity profiles was developed. The simulation results of this part indicate that increasing the number of the inlet manifolds is beneficial for the less pressure drop and uniform velocity profile over the cell active area. Furthermore, curvature and geometrical design of the outlet manifold may result in negative pressure zone and back flow separation. In addition, although modifying

parallel channels to the spot design causes decreasing of the mean velocity at areas adjacent to the interlaced ribs; they show almost similar pressure and velocity profiles. However, considering that CFCL is a world leading organisation focussed on the commercialization of the methane fuelled planar SOFCs, this model was further extended to include catalytic chemical and electrochemical reaction rates together with the heat effects from the air flow. To assist this aim, the electrodes were considered as two distinct volumes, referred to as diffusion and catalyst layers. In this way, the catalytic chemical reactions were treated in the anode diffusion layer, while the electrochemical sub-model was solved with the catalyst layers. To evaluate predictions from 3D CFD model, first, the results including the effect of the catalytic chemical (but with no fuel cell reactions) were compared with thermodynamic equilibrium data, simulation results from CFCL 1D model and the results from two other reforming models. It can be concluded that although both 1D and 3D models closely approach thermodynamic equilibrium, the 1D model somewhat over-predicts conversion that would be achieved in a real geometry and a 3D model is more representative of the global reaction rate. Moreover, different reforming kinetic models resulted in different prediction for methane conversion and temperature profiles. This is due to dissimilarities in chemical properties of the anode material, which are reflected entirely through their different intrinsic kinetic rates. In the next step, heat effect of the air flow together with chemical and electrochemical reaction rates was included. The predicted V-I curve from 3D CFD model showed good agreement with the experimental data from the similar geometry reported by CFCL.

In addition, due to the importance of the Ni-based anode support to provide internal reforming environment, a parametric study was carried out to investigate the combined effects of the geometrical factors and micro-structural parameters of the anode diffusion layer on distribution of the key parameters along different spatial domains. From the simulation results, it was shown that the complex interaction between the anode flow field design and micro-structural parameters of the anode diffusion layer can effectively influence the variation of different parameters across different distances of the cell, which in turn affects the engineering of the anode porous media. However, micro-structural parameters have been found to have conflicting effects on multi component gas transport and the reactions involved. It was shown that an optimal set of micro-structural parameters, which resulted in the

best performance for the reforming reaction rate, will not automatically result in the best SOFC performance. In view of this, the ADL structure with porosity of 0.4 and smaller pore radius is beneficial for the reforming reaction rate. However, including the electrochemical reaction and the heat effects of the air channels gave different micro-structural parameters for maximum utilization of the anode diffusion layer. In this regard, it is beneficial to keep the porosity low and have a trade-off between the thickness and pore size of the ADL. Considering the operating conditions and model input parameters, it was concluded that the mid-range of the pore size is beneficial for the overall performance of the cell. Moreover, it was shown that with a larger ADL thickness, the SOFC performance increases. However, it can reduce the reforming reaction rate due to the dilution of the reactants with product.

6.2. Future Work

In addition to the above conclusions, the results obtained from different perspectives for multi scale modelling of the planar SOFC, suggest several areas for future research.

First of all, the charge balance equations at the interface between the electron and ion conducting media can be used for calculating the activation overpotential with no restriction concerning the steps for the charge transfer process. In view of this, the developed dynamic models in the form of PFR or CSTR can be used for numerical impedance analysis, which will provide a better understanding of the main phenomena governing electrochemical reactions in fuel cells. Furthermore, based on the findings from the PFR model, it can be used for numerical impedance analysis. Therefore, it can provide practical applications for analysing the kinetic behaviours and designing of the material properties.

Moreover, to initiate the development of TSR model, we considered a scenario of a single cell fuelled by pure hydrogen without any consideration of the inlet manifolds and the stacking of the cell. Therefore, TSR model can be further advanced for the methane fuelled planar SOFC. In future, we can use the innovative method to integrate the TSR model with 3D CFD model of the methane fuelled SOFC. In view of this, the velocities of the fuel and air streams at the inlet of different CSTR

compartments can be adjusted by the velocity profiles predicted from the CFD model. In this way, the CFD models will be independent of the cell electrochemical parameters such as the voltage, current and the reactions, which will reduce the modelling and simulation effort. Furthermore, it can be expected that extending a TSR model for the stack will capture distribution of the key parameters with minimum computational effort. Therefore, TSR model of the SOFC stack, 3D CFD model of the flow fields and lumped parameter models of the BOP components can form a real multi scale model for tackling SOFC system design and control issues. The use of the distributed parameter control theory for control design of the SOFC is crucial for improving its power output, efficiency and life time. For example, it can eliminate the formation of hot spots in the cell thereby increasing the life time.

Additionally, to meet the scope of the future work, the simulation results from TSR model of the planar methane fuelled SOFC can be checked by comparison with the results from 3D CFD model developed in this research. However, the CFD model could be further advanced by incorporating interconnects' computational domains. In view of this we can set the appropriate boundary conditions between the anode diffusion layers and interconnects. As a consequence, charge balance approach can be used as the more accurate solution for the charge transfer processes. In addition, the exchange current densities can be treated as the function of the local temperature and species concentration profiles.

References

1. Faghri, A.; Guo, Z., Challenges and opportunities of thermal management issues related to fuel cell technology and modeling. *Int. J. Heat Mass Transfer* **2005,** 48, (19-20), 3891-3920.
2. Fontes, E.; Nilsson, E., Modeling the fuel cell. *The Industrial Physicist* **2001,** 7, (4), 14.
3. Bi, W.; Li, J.; Lin, Z., Flow uniformity optimization for large size planar solid oxide fuel cells with U-type parallel channel designs. *J. Power Sources* **2010,** 195, (10), 3207-3214.
4. Pakalapati, S. R. A new reduced order model for solid oxide fuel cells. Ph.D. Thesis, West Virginia University, 2006.
5. *International energy outlook 2010*; DOE/EIA-0484; U.S. Department of Energy: Washington DC.
6. Bove, R.; Ubertini, S., Modeling solid oxide fuel cell operation: Approaches, techniques and results. *J. Power Sources* **2006,** 159, (1), 543-559.
7. Recknagle, K. P.; Williford, R. E.; Chick, L. A.; Rector, D. R.; Khaleel, M. A., Three-dimensional thermo-fluid electrochemical modeling of planar SOFC stacks. *J. Power Sources* **2003,** 113, (1), 109-114.
8. Arpornwichanop, A.; Chalermpanchai, N.; Patcharavorachot, Y.; Assabumrungrat, S.; Tade, M., Performance of an anode-supported solid oxide fuel cell with direct-internal reforming of ethanol. *Int. J. Hydrogen Energy* **2009,** 34, (18), 7780-7788.
9. Wang, K.; Hissel, D.; Péra, M. C.; Steiner, N.; Marra, D.; Sorrentino, M.; Pianese, C.; Monteverde, M.; Cardone, P.; Saarinen, J., A Review on solid oxide fuel cell models. *Int. J. Hydrogen Energy* **2011,** 36, (12), 7212-7228.
10. Appleby, A. J.; Foulkes, F. R., *Fuel cell handbook*. Van Nostrand Reinhold: 1989.
11. Sabaripandiyan, D.; Daniel, A. In *A comparative review on small scale integration of hybrid fuel cell and PV generating system to utility network*, 2010; IEEE: 2010; pp 590-595.
12. Bagot s ki , V. S., *Fuel cells: problems and solutions*. Wiley: 2009.
13. Hoogers, G., *Fuel cell technology handbook*. CRC: 2003.

14. Gou, B.; Na, W. K.; Diong, B., *Fuel cells: modeling, control, and applications*. CRC: 2009.
15. Kaka , S.; Pramuanjaroenkij, A.; Zhou, X. Y., A review of numerical modeling of solid oxide fuel cells. *Int. J. Hydrogen Energy* **2007,** 32, (7), 761-786.
16. Larminie, J.; Dicks, A., *Fuel cell systems explained*. J. Wiley: 2003.
17. Huang, K.; Goodenough, J. B., *Solid Oxide Fuel Cell Technology: Principles, Performance and Operations*. Taylor and Francis: 2009.
18. Maric, R.; Ohara, S.; Fukui, T.; Yoshida, H.; Nishimura, M.; Inagaki, T.; Miura, K., Solid Oxide Fuel Cells with Doped Lanthanum Gallate Electrolyte and LaSrCoO Cathode, and Ni-Samaria-Doped Ceria Cermet Anode. *J. Electrochem. Soc.* **1999,** 146, 2006.
19. Gorte, R. J., Recent developments towards commercialization of solid oxide fuel cells. *AIChE J.* **2005,** 51, (9), 2377-2381.
20. Stambouli, A. B.; Traversa, E., Solid oxide fuel cells (SOFCs): a review of an environmentally clean and efficient source of energy. *Renewable Sustainable Energy Rev.* **2002,** 6, (5), 433-455.
21. Yamamoto, O., Solid oxide fuel cells: fundamental aspects and prospects. *Electrochim. Acta* **2000,** 45, (15-16), 2423-2435.
22. Fergus, J. W., Metallic interconnects for solid oxide fuel cells. *Mater. Sci. Eng.* **2005,** 397, (1-2), 271-283.
23. Fergus, J. W., Lanthanum chromite-based materials for solid oxide fuel cell interconnects. *Solid State Ionics* **2004,** 171, (1-2), 1-15.
24. Zhu, W.; Deevi, S., Development of interconnect materials for solid oxide fuel cells. *Mater. Sci. Eng.* **2003,** 348, (1-2), 227-243.
25. Stiller, C. Design, operation and control modelling of SOFC/GT hybrid systems. Ph.D. Thesis, Norwegian University of Science and Technology, 2006.
26. Larrain, D. Solid oxide fuel cell stack simulation and optimization, including experimental validation and transient behavior. ÉCOLE POLYTECHNIQUE FÉDÉRALE DE LAUSANNE, 2005.
27. Colpan, C. O.; Dincer, I.; Hamdullahpur, F., A review on macro level modeling of planar solid oxide fuel cells. *Int. J. Energy Res.* **2008,** 32, (4), 336-355.
28. Andersson, M.; Yuan, J.; Sundén, B., Review on modeling development for multiscale chemical reactions coupled transport phenomena in solid oxide fuel cells. *Appl. Energy* **2010,** 87, (5), 1461-1476.

29. Fung, A.; Zabihian, F., A Review on Modeling of Hybrid Solid Oxide Fuel Cell Systems. *Int. J. Eng.* **2009,** 3, (2), 85-119.
30. Bhattacharyya, D.; Rengaswamy, R., A review of solid oxide fuel cell (SOFC) dynamic models. *Ind. Eng. Chem. Res.* **2009,** 48, (13), 6068-6086.
31. Yang, Y.; Du, X.; Yang, L.; Huang, Y.; Xian, H., Investigation of methane steam reforming in planar porous support of solid oxide fuel cell. *Appl. Therm. Eng.* **2009,** 29, (5-6), 1106-1113.
32. Ni, M.; Leung, D. Y. C.; Leung, M. K. H., Electrochemical modeling and parametric study of methane fed solid oxide fuel cells. *Energy Convers. Manage.* **2009,** 50, (2), 268-278.
33. Costamagna, P.; Costa, P.; Antonucci, V., Micro-modelling of solid oxide fuel cell electrodes. *Electrochim. Acta* **1998,** 43, (3-4), 375-394.
34. Chan, S.; Khor, K.; Xia, Z., A complete polarization model of a solid oxide fuel cell and its sensitivity to the change of cell component thickness. *J. Power Sources* **2001,** 93, (1-2), 130-140.
35. Chan, S.; Xia, Z., Anode micro model of solid oxide fuel cell. *J. Electrochem. Soc.* **2001,** 148, A388.
36. Lehnert, W.; Meusinger, J.; Thom, F., Modelling of gas transport phenomena in SOFC anodes. *J. Power Sources* **2000,** 87, (1-2), 57-63.
37. Yakabe, H.; Hishinuma, M.; Uratani, M.; Matsuzaki, Y.; Yasuda, I., Evaluation and modeling of performance of anode-supported solid oxide fuel cell. *J. Power Sources* **2000,** 86, (1-2), 423-431.
38. Yuan, J., Simulation and Analysis of Multi-scale Transport Phenomena and Catalytic Reactions in SOFC Anodes. *Chem. Prod. Process Model.* **2010,** 5, (1), 12.
39. Brown, M.; Primdahl, S.; Mogensen, M., Structure/performance relations for Ni/yttria-stabilized zirconia anodes for solid oxide fuel cells. *J. Electrochem. Soc.* **2000,** 147, 475.
40. Bieberle, A.; Meier, L.; Gauckler, L., The electrochemistry of Ni pattern anodes used as solid oxide fuel cell model electrodes. *J. Electrochem. Soc.* **2001,** 148, A646.
41. Hussain, M.; Li, X.; Dincer, I., Multi component mathematical model of solid oxide fuel cell anode. *Int. J. Energy Res.* **2005,** 29, (12), 1083-1101.

42. Divisek, J.; Jung, R.; Vinke, I., Structure investigations of SOFC anode cermets part II: electrochemical and mass transport properties. *J. Appl. Electrochem.* **1999,** 29, (2), 165-170.

43. Suwanwarangkul, R.; Croiset, E.; Fowler, M.; Douglas, P.; Entchev, E.; Douglas, M., Performance comparison of Fick's, dusty-gas and Stefan-Maxwell models to predict the concentration overpotential of a SOFC anode. *J. Power Sources* **2003,** 122, (1), 9-18.

44. Mitterdorfer, A.; Gauckler, L., Identification of the reaction mechanism of the Pt, O2 (g)| yttria-stabilized zirconia system:: Part I: General framework, modelling, and structural investigation. *Solid State Ionics* **1999,** 117, (3-4), 187-202.

45. Huang, Q. A.; Hui, R.; Wang, B.; Zhang, J., A review of AC impedance modeling and validation in SOFC diagnosis. *Electrochim. Acta* **2007,** 52, (28), 8144-8164.

46. Takano, K.; Nagata, S.; Nozaki, K.; Monma, A.; Kato, T.; Kaga, Y.; Negishi, A.; Kato, K.; Inagaki, T.; Yoshida, H., Numerical simulation of a disk-type SOFC for impedance analysis under power generation. *J. Power Sources* **2004,** 132, (1-2), 42-51.

47. Barfod, R.; Mogensen, M.; Klemensø, T.; Hagen, A.; Liu, Y. L.; Hendriksen, P. V., Detailed characterization of anode-supported SOFCs by impedance spectroscopy. *J. Electrochem. Soc.* **2007,** 154, B371.

48. Bessler, W. G.; Gewies, S.; Vogler, M., A new framework for physically based modeling of solid oxide fuel cells. *Electrochim. Acta* **2007,** 53, (4), 1782-1800.

49. Hofmann, P.; Panopoulos, K., Detailed dynamic Solid Oxide Fuel Cell modeling for electrochemical impedance spectra simulation. *J. Power Sources* **2010,** 195, (16), 5320-5339.

50. Zhu, H.; Kee, R. J., Modeling electrochemical impedance spectra in SOFC button cells with internal methane reforming. *J. Electrochem. Soc.* **2006,** 153, A1765.

51. Bessler, W. G., A new computational approach for SOFC impedance from detailed electrochemical reaction-diffusion models. *Solid State Ionics* **2005,** 176, (11-12), 997-1011.

52. Bi, W.; Chen, D.; Lin, Z., A key geometric parameter for the flow uniformity in planar solid oxide fuel cell stacks. *Int. J. Hydrogen Energy* **2009,** 34, (9), 3873-3884.

53. Koh, J. H.; Seo, H. K.; Lee, C. G.; Yoo, Y. S.; Lim, H. C., Pressure and flow distribution in internal gas manifolds of a fuel-cell stack. *J. Power Sources* **2003,** 115, (1), 54-65.
54. Maharudrayya, S.; Jayanti, S.; Deshpande, A., Flow distribution and pressure drop in parallel-channel configurations of planar fuel cells. *J. Power Sources* **2005,** 144, (1), 94-106.
55. Maharudrayya, S.; Jayanti, S.; Deshpande, A., Pressure losses in laminar flow through serpentine channels in fuel cell stacks. *J. Power Sources* **2004,** 138, (1-2), 1-13.
56. Liu, H.; Li, P.; Lew, J. V., CFD study on flow distribution uniformity in fuel distributors having multiple structural bifurcations of flow channels. *Int. J. Hydrogen Energy* **2010,** 35, (17), 9186-9198.
57. Li, P.; Coopamah, D.; Ki, J. P. In *Uniform Distribution of Species in Fuel Cells Using a Multiple Flow Bifurcation Design*, Sixth international conference on fuel cell science, June 16-18, 2008; ASME: 2008.
58. Huang, C.; Shy, S.; Lee, C., On flow uniformity in various interconnects and its influence to cell performance of planar SOFC. *J. Power Sources* **2008,** 183, (1), 205-213.
59. Yakabe, H.; Ogiwara, T.; Hishinuma, M.; Yasuda, I., 3-D model calculation for planar SOFC. *J. Power Sources* **2001,** 102, (1-2), 144-154.
60. Qu, Z.; Aravind, P. V.; Boksteen, S. Z.; Dekker, N. J. J.; Janssen, A. H. H.; Woudstra, N.; Verkooijen, A. H. M., Three-dimensional computational fluid dynamics modeling of anode-supported planar SOFC. *Int. J. Hydrogen Energy* In Press, Corrected Proof.
61. Danilov, V. A.; Tade, M. O., A CFD-based model of a planar SOFC for anode flow field design. *Int. J. Hydrogen Energy* **2009,** 34, (21), 8998-9006.
62. Ferguson, J.; Fiard, J.; Herbin, R., Three-dimensional numerical simulation for various geometries of solid oxide fuel cells. *J. Power Sources* **1996,** 58, (2), 109-122.
63. Xia, W.; Yang, Y.; Wang, Q., Effects of operations and structural parameters on the one-cell stack performance of planar solid oxide fuel cell. *J. Power Sources* **2009,** 194, (2), 886-898.

64. Janardhanan, V. M.; Deutschmann, O., CFD analysis of a solid oxide fuel cell with internal reforming: Coupled interactions of transport, heterogeneous catalysis and electrochemical processes. *J. Power Sources* **2006,** 162, (2), 1192-1202.
65. Achenbach, E., Three-dimensional and time-dependent simulation of a planar solid oxide fuel cell stack. *J. Power Sources* **1994,** 49, (1-3), 333-348.
66. Li, J.; Cao, G. Y.; Zhu, X. J.; Tu, H. Y., Two-dimensional dynamic simulation of a direct internal reforming solid oxide fuel cell. *J. Power Sources* **2007,** 171, (2), 585-600.
67. Serincan, M. F.; Pasaogullari, U.; Sammes, N. M., A transient analysis of a micro-tubular solid oxide fuel cell (SOFC). *J. Power Sources* **2009,** 194, (2), 864-872.
68. Krewer, U.; Pfafferodt, M.; Kamat, A.; Menendez, D. F.; Sundmacher, K., Hydrodynamic characterisation and modelling of anode flow fields of Direct Methanol Fuel Cells. *Chem. Eng. J.* **2007,** 126, (2-3), 87-102.
69. Ho, T. X. Modeling of Transport, Chemical and Electrochemical Processes in Solid Oxide Fuel Cells. Ph.D. Thesis, University of Bergen, 2009.
70. Zhu, H.; Kee, R. J.; Janardhanan, V. M.; Deutschmann, O.; Goodwin, D. G., Modeling elementary heterogeneous chemistry and electrochemistry in solid-oxide fuel cells. *J. Electrochem. Soc.* **2005,** 152, A2427.
71. Lai, K.; Koeppel, B. J.; Choi, K. S.; Recknagle, K. P.; Sun, X.; Chick, L. A.; Korolev, V.; Khaleel, M., A quasi-two-dimensional electrochemistry modeling tool for planar solid oxide fuel cell stacks. *J. Power Sources* **2011,** 196, (6), 3204-3222.
72. Burt, A.; Celik, I.; Gemmen, R.; Smirnov, A., A numerical study of cell-to-cell variations in a SOFC stack. *J. Power Sources* **2004,** 126, (1-2), 76-87.
73. Xue, X.; Tang, J.; Sammes, N.; Du, Y., Dynamic modeling of single tubular SOFC combining heat/mass transfer and electrochemical reaction effects. *J. Power Sources* **2005,** 142, (1-2), 211-222.
74. Cheddie, D. F.; Munroe, N. D. H., A dynamic 1D model of a solid oxide fuel cell for real time simulation. *J. Power Sources* **2007,** 171, (2), 634-643.
75. Aguiar, P.; Adjiman, C.; Brandon, N., Anode-supported intermediate-temperature direct internal reforming solid oxide fuel cell:: II. Model-based dynamic performance and control. *J. Power Sources* **2005,** 147, (1-2), 136-147.
76. Aguiar, P.; Adjiman, C.; Brandon, N. P., Anode-supported intermediate temperature direct internal reforming solid oxide fuel cell. I: model-based steady-state performance. *J. Power Sources* **2004,** 138, (1-2), 120-136.

77. Kang, Y.; Li, J.; Cao, G.; Tu, H.; Yang, J., One-dimensional dynamic modeling and simulation of a planar direct internal reforming solid oxide fuel cell. *Chin. J. Chem. Eng.* **2009,** 17, (2), 304-317.

78. Kang, Y. W.; Li, J.; Cao, G. Y.; Tu, H. Y.; Yang, J., A reduced 1D dynamic model of a planar direct internal reforming solid oxide fuel cell for system research. *J. Power Sources* **2009,** 188, (1), 170-176.

79. Wang, C.; Nehrir, M. H., A physically based dynamic model for solid oxide fuel cells. *Energy Convers.* **2007,** 22, (4), 887-897.

80. Campanari, S., Thermodynamic model and parametric analysis of a tubular SOFC module. *J. Power Sources* **2001,** 92, (1-2), 26-34.

81. Lin, Z.; Stevenson, J.; Khaleel, M., The effect of interconnect rib size on the fuel cell concentration polarization in planar SOFCs. *J. Power Sources* **2003,** 117, (1-2), 92-97.

82. Winkler, W.; Nehter, P.; Williams, M. C.; Tucker, D.; Gemmen, R., General fuel cell hybrid synergies and hybrid system testing status. *J. Power Sources* **2006,** 159, (1), 656-666.

83. Suther, T.; Fung, A. S.; Koksal, M.; Zabihian, F., Effects of operating and design parameters on the performance of a solid oxide fuel cell–gas turbine system. *Int. J. Energy Res.* **2011,** 35, (7), 616-632.

84. Chan, S.; Ho, H.; Tian, Y., Modelling of simple hybrid solid oxide fuel cell and gas turbine power plant. *J. Power Sources* **2002,** 109, (1), 111-120.

85. Chan, S.; Ho, H.; Tian, Y., Multi-level modeling of SOFC-gas turbine hybrid system. *Int. J. Hydrogen Energy* **2003,** 28, (8), 889-900.

86. Calise, F.; Dentice, A., Simulation and exergy analysis of a hybrid solid oxide fuel cell (SOFC)-gas turbine system. *Energy* **2006,** 31, (15), 3278-3299.

87. Freeh, J. E.; Pratt, J. W.; Brouwer, J., Development of a solid-oxide fuel cell/gas turbine hybrid system model for aerospace applications. *ASME Paper Number GT2004-53616* **2004**.

88. Roberts, R.; Brouwer, J.; Jabbari, F.; Junker, T.; Ghezel-Ayagh, H., Control design of an atmospheric solid oxide fuel cell/gas turbine hybrid system: Variable versus fixed speed gas turbine operation. *J. Power Sources* **2006,** 161, (1), 484-491.

89. Zhu, Y.; Tomsovic, K., Development of models for analyzing the load-following performance of microturbines and fuel cells. *Electr. Power Syst. Res.* **2002,** 62, (1), 1-11.

90. Kimijima, S.; Kasagi, N. In *Performance evaluation of gas turbine-fuel cell hybrid micro generation system*, 2002; ASME: 2002.
91. Magistri, L.; Traverso, A.; Cerutti, F.; Bozzolo, M.; Costamagna, P.; Massardo, A., Modelling of Pressurised Hybrid Systems Based on Integrated Planar Solid Oxide Fuel Cell (IP SOFC) Technology. *Fuel Cells* **2005,** 5, (1), 80-96.
92. Selimovic, A.; Palsson, J., Networked solid oxide fuel cell stacks combined with a gas turbine cycle. *J. Power Sources* **2002,** 106, (1-2), 76-82.
93. Song, T. W.; Sohn, J. L.; Kim, J. H.; Kim, T. S.; Ro, S. T.; Suzuki, K., Performance analysis of a tubular solid oxide fuel cell/micro gas turbine hybrid power system based on a quasi-two dimensional model. *J. Power Sources* **2005,** 142, (1-2), 30-42.
94. Stiller, C.; Thorud, B.; Bolland, O., Safe dynamic operation of a simple SOFC/GT hybrid system. *J. Eng. Gas Turbines Power* **2006,** 128, 551.
95. Hecht, E. S.; Gupta, G. K.; Zhu, H.; Dean, A. M.; Kee, R. J.; Maier, L.; Deutschmann, O., Methane reforming kinetics within a Ni-YSZ SOFC anode support. *Appl. Catal., A* **2005,** 295, (1), 40-51.
96. Mangold, M.; Krasnyk, M.; Sundmacher, K., Theoretical investigation of steady state multiplicities in solid oxide fuel cells*. *J. Appl. Electrochem.* **2006,** 36, (3), 265-275.
97. Aguiar, P.; Chadwick, D.; Kershenbaum, L., Modelling of an indirect internal reforming solid oxide fuel cell. *Chem. Eng. Sci.* **2002,** 57, (10), 1665-1677.
98. Bansal, R., *Handbook of engineering electromagnetics*. Marcel Dekker: New York, 2004.
99. Zhu, H.; Kee, R. J., Modeling distributed charge-transfer processes in SOFC membrane electrode assemblies. *J. Electrochem. Soc.* **2008,** 155, B715-B729.
100. Hendriks, M.; Ten Elshof, J.; Bouwmeester, H.; Verweij, H., The electrochemical double-layer capacitance of yttria-stabilised zirconia. *Solid State Ionics* **2002,** 146, (3-4), 211-217.
101. Kwon, K. H.; Shin, C. B.; Kang, T. H.; Kim, C. S., A two-dimensional modeling of a lithium-polymer battery. *J. Power Sources* **2006,** 163, (1), 151-157.
102. Munder, B.; Ye, Y.; Rihko-Struckmann, L.; Sundmacher, K., Solid electrolyte membrane reactor for controlled partial oxidation of hydrocarbons: Model and experimental validation. *Catal. Today* **2005,** 104, (2-4), 138-148.
103. Bagotsky, V. S.; Müller, K., *Fundamentals of electrochemistry*. Wiley-Interscience NJ: 2006.

104. Chaisantikulwat, A.; Diaz-Goano, C.; Meadows, E., Dynamic modelling and control of planar anode-supported solid oxide fuel cell. *Computers & Chemical Engineering* **2008,** 32, (10), 2365-2381.

105. Ho, T. X.; Kosinski, P.; Hoffmann, A. C.; Vik, A., Modeling of transport, chemical and electrochemical phenomena in a cathode-supported SOFC. *Chem. Eng. Sci.* **2009,** 64, (12), 3000-3009.

106. Skeel, R. D.; Berzins, M., A method for the spatial discretization of parabolic equations in one space variable. *SIAM journal on scientific and statistical computing* **1990,** 11, (1), 1-32.

107. Keegan, K. R.; Khaleel, M. A.; Chick, L. A.; Recknagle, K. P.; Simner, S. P.; Deibler, J. E. *Analysis of a planar solid oxide fuel cell based automotive auxiliary power unit*; Pacific Northwest National Laboratory (PNNL), Richland, WA (US): 2003.

108. Hosseini, S.; Danilov, V. A.; Vijay, P.; Tadé, M. O., Improved Tank in Series Model for the Planar Solid Oxide Fuel Cell. *Ind. Eng. Chem. Res.* **2010,** 50, (2), 1056-1069.

109. Damm, D. L.; Fedorov, A. G., Spectral radiative heat transfer analysis of the planar SOFC. *J. Fuel Cell Sci. Technol.* **2005,** 2, 258.

110. Daun, K.; Beale, S.; Liu, F.; Smallwood, G., Radiation heat transfer in planar SOFC electrolytes. *J. Power Sources* **2006,** 157, (1), 302-310.

111. Todd, B.; Young, J. B., Thermodynamic and transport properties of gases for use in solid oxide fuel cell modelling. *J. Power Sources* **2002,** 110, (1), 186-200.

112. Ravussin, F., Local current measurement in a solid oxide fuel cell repeat element. *J. Eur. Ceram. Soc.* **2007,** 27, (2-3), 1035-1040.

113. Iserles, A., *A first course in the numerical analysis of differential equations*. Cambridge Univ Pr: 2009; Vol. 44.

114. Society, A. M., *Reviews in numerical analysis, 1980-86: as printed in Mathematical reviews*. American Mathematical Society: 1987.

115. Patcharavorachot, Y.; Arpornwichanop, A.; Chuachuensuk, A., Electrochemical study of a planar solid oxide fuel cell: Role of support structures. *J. Power Sources* **2008,** 177, (2), 254-261.

116. Iwata, M.; Hikosaka, T.; Morita, M.; Iwanari, T.; Ito, K.; Onda, K.; Esaki, Y.; Sakaki, Y.; Nagata, S., Performance analysis of planar-type unit SOFC considering current and temperature distributions. *Solid State Ionics* **2000,** 132, (3-4), 297-308.

117. Bhattacharyya, D.; Rengasamy, R.; Caine, F., Dynamic simulation and analysis of a solid oxide fuel cell (SOFC). *Comput.-Aided Chem. Eng.* **2007,** 24, 907-912.
118. Bhattacharyya, D.; Rengaswamy, R.; Finnerty, C., Dynamic modeling and validation studies of a tubular solid oxide fuel cell. *Chem. Eng. Sci.* **2009,** 64, (9), 2158-2172.
119. Xie, Y.; Xue, X., Transient modeling of anode-supported solid oxide fuel cells. *Int. J. Hydrogen Energy* **2009,** 34, (16), 6882-6891.
120. Krewer, U.; Kamat, A.; Sundmacher, K., Understanding the dynamic behaviour of direct methanol fuel cells: Response to step changes in cell current. *J. Electroanal. Chem.* **2007,** 609, (2), 105-119.
121. Kenney, B.; Karan, K., Engineering of microstructure and design of a planar porous composite SOFC cathode: A numerical analysis. *Solid state ionics* **2007,** 178, (3-4), 297-306.
122. Hajimolana, S. A.; Hussain, M. A.; Daud, W.; Soroush, M.; Shamiri, A., Mathematical modeling of solid oxide fuel cells: A review. *Renewable Sustainable Energy Rev.* **2011,** 15, (4), 1893-1917.
123. Versteeg, H. K.; Malalasekera, W., *An introduction to computational fluid dynamics: the finite volume method*. Prentice Hall: 2007.
124. Qu, Z.; Aravind, P. V.; Boksteen, S. Z.; Dekker, N. J. J.; Janssen, A. H. H.; Woudstra, N.; Verkooijen, A. H. M., Three-dimensional computational fluid dynamics modeling of anode-supported planar SOFC. *Int. J. Hydrogen Energy* **2011,** 36, (16), 10209-10220.
125. Pasaogullari, U.; Wang, C. Y., Computational fluid dynamics modeling of solid oxide fuel cells. *Proceedings of the Electrochemical Society (Solid Oxide Fuels Cells VIII, Paris)* **2003,** 7, 1403.
126. Smith, J. M.; Ness, H. C. V.; Abbott, M. M., *Introduction to chemical engineering thermodynamics*. McGraw-Hill: 2005.
127. *ANSYS FLUENT 13.0 User Guide*. ANSYS Inc.: Pennsylvania, USA, 2010.
128. Todd, B.; Young, J., Thermodynamic and transport properties of gases for use in solid oxide fuel cell modelling. *J. Power Sources* **2002,** 110, (1), 186-200.
129. Jeon, D. H., A comprehensive CFD model of anode-supported solid oxide fuel cells. *Electrochim. Acta* **2009,** 54, (10), 2727-2736.
130. Autissier, N.; Larrain, D., CFD simulation tool for solid oxide fuel cells. *J. Power Sources* **2004,** 131, (1-2), 313-319.

131. Bird, R. B.; Stewart, W. E.; Lightfoot, E. N., *Transport phenomena*. J. Wiley: 2007.
132. Autissier, N.; Larrain, D., CFD simulation tool for solid oxide fuel cells. *Journal of Power Sources* **2004,** 131, (1-2), 313-319.
133. Shi, L. Computational fluid dynamics simulation of steam reforming and autothermal reforming for fuel cell applications. Ohio University, 2009.
134. Li, P. W.; Schaefer, L.; Chyu, M. K., A numerical model coupling the heat and gas species' transport processes in a tubular SOFC. *J. Heat Transfer* **2004,** 126, 219.
135. Lubelli, F., Internal reforming solid oxide fuel cell-gas turbine combined cycles (IRSOFC-GT): part A—cell model and cycle thermodynamic analysis. *J. Eng. Gas Turbines Power* **2000,** 122, 27.
136. Campanari, S.; Iora, P., Comparison of finite volume SOFC models for the simulation of a planar cell geometry. *Fuel Cells* **2005,** 5, (1), 34-51.
137. Achenbach, E.; Riensche, E., Methane/steam reforming kinetics for solid oxide fuel cells. *J. Power Sources* **1994,** 52, (2), 283-288.
138. Ahmed, K.; Foger, K., Kinetics of internal steam reforming of methane on Ni/YSZ-based anodes for solid oxide fuel cells. *Catal. Today* **2000,** 63, (2-4), 479-487.
139. Sanchez, D.; Chacartegui, R.; Munoz, A.; Sanchez, T., On the effect of methane internal reforming modelling in solid oxide fuel cells. *Int. J. Hydrogen Energy* **2008,** 33, (7), 1834-1844.
140. Haberman, B.; Young, J., Three-dimensional simulation of chemically reacting gas flows in the porous support structure of an integrated-planar solid oxide fuel cell. *Int. J. Heat Mass Transfer* **2004,** 47, (17-18), 3617-3629.
141. Yuan, J.; Huang, Y.; Sundén, B.; Wang, W. G., Analysis of parameter effects on chemical reaction coupled transport phenomena in SOFC anodes. *Heat Mass Transfer* **2009,** 45, (4), 471-484.
142. Ni, M.; Leung, D. Y. C.; Leung, M. K. H., Modeling of methane fed solid oxide fuel cells: Comparison between proton conducting electrolyte and oxygen ion conducting electrolyte. *J. Power Sources* **2008,** 183, (1), 133-142.
143. Klein, J. M.; Bultel, Y.; Georges, S.; Pons, M., Modeling of a SOFC fuelled by methane: From direct internal reforming to gradual internal reforming. *Chem. Eng. Sci.* **2007,** 62, (6), 1636-1649.
144. Hofmann, P.; Panopoulos, K.; Fryda, L.; Kakaras, E., Comparison between two methane reforming models applied to a quasi-two-dimensional planar solid oxide fuel cell model. *Energy* **2009,** 34, (12), 2151-2157.

145. Drescher, I.; Lehnert, W.; Meusinger, J., Structural properties of SOFC anodes and reactivity. *Electrochim. Acta* **1998,** 43, (19-20), 3059-3068.
146. Hou, K.; Hughes, R., The kinetics of methane steam reforming over a Ni/[alpha]-Al2O catalyst. *Chem. Eng. J.* **2001,** 82, (1-3), 311-328.
147. Qi, Y.; Huang, B.; Luo, J., Dynamic modeling of a finite volume of solid oxide fuel cell: The effect of transport dynamics. *Chem. Eng. Sci.* **2006,** 61, (18), 6057-6076.
148. Hussain, M. M.; Li, X.; Dincer, I., Mathematical modeling of transport phenomena in porous SOFC anodes. *Int. J. Therm. Sci.* **2007,** 46, (1), 48-56.
149. Tanner, C. W.; Fung, K. Z.; Virkar, A. V., The effect of porous composite electrode structure on solid oxide fuel cell performance. *J. Electrochem. Soc.* **1997,** 144, 21.
150. Hussain, M. M.; Li, X.; Dincer, I., Mathematical modeling of planar solid oxide fuel cells. *J. Power Sources* **2006,** 161, (2), 1012-1022.
151. Fleig, J., Solid oxide fuel cell cathodes: polarization mechanisms and modeling of the electrochemical performance. *Annu. Rev. Mater. Res.* **2003,** 33, (1), 361-382.
152. Qu, Z.; Aravind, P. V.; Dekker, N. J. J.; Janssen, A. H. H.; Woudstra, N.; Verkooijen, A. H. M., Three-dimensional thermo-fluid and electrochemical modeling of anode-supported planar solid oxide fuel cell. *J. Power Sources* **2010,** 195, (23), 7787-7795.
153. Cooke, A. J.; Rowe, R. K., Extension of porosity and surface area models for uniform porous media. *J. Environ. Eng.* **1999,** 125, (2), 126-136.
154. Bertei, A.; Nicolella, C., Percolation theory in SOFC composite electrodes: Effects of porosity and particle size distribution on effective properties. *J. Power Sources* **2011,** 196, (22), 9429-9436.
155. Maharudrayya, S.; Jayanti, S.; Deshpande, A. P., Pressure losses in laminar flow through serpentine channels in fuel cell stacks. *J. Power Sources* **2004,** 138, (1-2), 1-13.
156. Laurencin, J.; Lefebvre-Joud, F.; Delette, G., Impact of cell design and operating conditions on the performances of SOFC fuelled with methane. *J. Power Sources* **2008,** 177, (2), 355-368.
157. Welty, J. R.; Wicks, C. E.; Wilson, R. E., *Fundamentals of momentum, heat, and mass transfer*. Wiley: 1984.
158. Qi, Y.; Huang, B.; Chuang, K. T., Dynamic modeling of solid oxide fuel cell: The effect of diffusion and inherent impedance. *J. Power Sources* **2005,** 150, 32-47.

Every reasonable effort has been made to acknowledge the owners of copyright material. I would be pleased to hear from any copyright owner who has been omitted or incorrectly acknowledged.

Appendix A – Estimation of the Gas Diffusivity

The binary diffusivity of a pair of gaseous species i and j is modelled by the Fuller's correlation [157, 158].

$$D_{ij} = \frac{1.013^{-2} T^{1.75} \left(\frac{1}{M_{w,i}} + \frac{1}{M_{w,j}}\right)^{0.5}}{P\left[\left(\sum v_i\right)^{1/3} + \left(\sum v_j\right)^{1/3}\right]^2} \quad \text{(A-1)}$$

However, diffusion coefficient of species i in the multi-component gas mixture is calculated by the expression that is based on the binary coefficients [37].

$$D_{i,GM} = \frac{1 - y_i}{\sum_{j \neq i}^{m} \frac{y_j}{D_{ij}}} \quad \text{(A-2)}$$

For the porous layer with large pores, diffusion flux is predominant and the effective diffusion coefficient components can be calculated from equation (A-2). However, Knudsen diffusion occurs in the porous layer with small pores when the mean free-path of molecules is smaller than the pore size, and the molecules collide with the walls more often between themselves. Knudsen diffusion coefficient D_{ik} is calculated based on the free molecule flow theory [38].

$$D_{i,k} = \frac{2}{3} r_p \sqrt{\frac{8RT}{\pi M_{w,i}}} \quad \text{(A-3)}$$

To account for the effects of Knudsen diffusion, porosity and the increased diffusion length due to the tortuous paths of real pores of the porous electrodes, the effective diffusion coefficient can be evaluated as follows [38] .

$$D_i^{eff} = \frac{\varepsilon}{\iota} \left(\frac{D_{i,GM} \times D_{i,k}}{D_{i,GM} + D_{i,k}}\right) \quad \text{(A-4)}$$